AD-A257 989

||||||||||||||||||||||||

RL-TR-91-382
Final Technical Report
December 1991

PHOTOREFRACTIVE PROPERTIES OF DOPED BaTiO3 AND SBN

Massachusetts Institute of Technology

DTIC
S **ELECTE**
DEC 0 8 1992
E **D**

APPROVED FOR PUBLIC RELEASE; DISTRIBUTION UNLIMITED.

92-30964

||||||||||||||||||||||
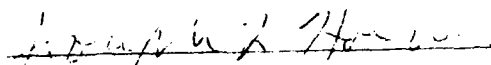
Rome Laboratory
Air Force Systems Command
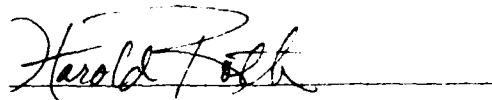Griffiss Air Force Base, NY 13441-5700

This report has been reviewed by the Rome Laboratory Public Affairs Office (PA) and is releasable to the National Technical Information Service (NTIS). At NTIS it will be releasable to the general public, including foreign nations.

RL-TR-91-382 has been reviewed and is approved for publication.

APPROVED:

JOSEPH L. HORNER
Project Engineer

FOR THE COMMANDER:

HAROLD ROTH, Director
Solid State Sciences
Electromagnetics & Reliability Directorate

If your address has changed or if you wish to be removed from the Rome Laboratory mailing list, or if the addressee is no longer employed by your organization, please notify RL(ERO) Hanscom AFB MA 01731-5000. This will assist us in maintaining a current mailing list.

Do not return copies of this report unless contractual obligations or notices on a specific document require that it be returned.

Accesion For		
NTIS CRA&I		☒
DTIC TAB		☐
Unannounced		☐
Justification		

PHOTOREFRACTIVE PROPERTIES OF DOPED BaTiO3 AND SBN

Dr Cardinal Warde

By		
Distribution /		
Availability Codes		
Dist	Avail and / or Special	
A-1		

Contractor: Massachusetts Institute of Technology
Contract Number: F19628-85-K-0050
Effective Date of Contract: 21 Feb 86
Contract Expiration Date: 31 May 92
Short Title of Work: Photorefractive Properties of Doped
$BaTiO_3$ and SBN

Period of Work Covered: Feb 86 - May 92

Principal Investigator: Dr Cardinal Warde
　　　　　　　　Phone: (617) 275-3100

Project Engineer:　　　Joseph Horner
　　　　　　　　Phone: (617) 377-3841

REPORT DOCUMENTATION PAGE

Form Approved
OMB No. 0704-0188

1. AGENCY USE ONLY (Leave Blank)	2. REPORT DATE December 1991	3. REPORT TYPE AND DATES COVERED Final Feb 86 - May 92

4. TITLE AND SUBTITLE

PHOTOREFRACTIVE PROPERTIES OF DOPED BaTiO3 AND SBN

6. AUTHOR(S)

Cardinal Warde

5. FUNDING NUMBERS

C - F19628-85-K-0050
PE - 61101E
PR - E397
TA - AR
WU - 20

7. PERFORMING ORGANIZATION NAME(S) AND ADDRESS(ES)

Massachusetts Institute of Technology
Cambridge MA 02139

8. PERFORMING ORGANIZATION REPORT NUMBER

N/A

9. SPONSORING/MONITORING AGENCY NAME(S) AND ADDRESS(ES)

Defense Advanced Research
     Projects Agency
1400 Wilson Blvd
Arlington VA 22209

Rome Laboratory (ERO)
Hanscom AFB MA 01731-5000

10. SPONSORING/MONITORING AGENCY REPORT NUMBER

RL-TR-91-382

11. SUPPLEMENTARY NOTES

Rome Laboratory Project Engineer: Joseph L. Horner/ERO/(617) 377-3841

12a. DISTRIBUTION/AVAILABILITY STATEMENT

Approved for public release; distribution unlimited.

12b. DISTRIBUTION CODE

13. ABSTRACT (Maximum 200 words)

Several novel photorefractive scattering processes were studied. Isotropic scattering of a single intense pump beam was observed and modeled. Numerical calculations, performed using material parameters consistent with the previous experiments, yielded scattering cross sections in excellent agreement with the observations. Anisotropic scattering of a single extraordinary polarized beam into conical rings of light was also observed. Using a phase matching condition and the electrooptic tensor symmetry properties of $BaTiO_3$, the scattering process of the inner ring was uniquely determined. A model which describes the formation of the outer ring was also proposed.

14. SUBJECT TERMS

Photorefractive Effect, Barium Titanate, Stronium Barium Niobate, Iron Doping, Anisotropic Diffraction

15. NUMBER OF PAGES 92

16. PRICE CODE

17. SECURITY CLASSIFICATION OF REPORT UNCLASSIFIED	18. SECURITY CLASSIFICATION OF THIS PAGE UNCLASSIFIED	19. SECURITY CLASSIFICATION OF ABSTRACT UNCLASSIFIED	20. LIMITATION OF ABSTRACT UL

Abstract

Photorefractive materials are an important class of electrooptic materials used in a wide variety of nonlinear optical devices. Although recent theories explaining the photorefractive charge transport properties of these materials have been relatively successful, the origin of the charge centers is unknown. Also, there are several anomalous effects observed in $BaTiO_3$ which indicate that the charge transport models are incomplete.

In this investigation, photo-induced absorption, and isotropic and anisotropic photorefractive gratings were used to study the photo-induced charge transport properties of $BaTiO_3$ in an attempt to identify the photorefractive species. Previous models and experiments on $BaTiO_3$ have not taken into account the effects of photo-induced absorption in studying photorefractive gratings. Also, most of this early work concentrated on the isotropic nature of these gratings to determine the material properties. The experiments and analyses presented here extend these techniques, both theoretically and experimentally, to include photo-induced absorption and anisotropic photorefractive gratings.

The photo-induced absorption experiments presented here represent evidence for the existence of a distribution of localized trapping states in the band gap of $BaTiO_3$. The intensity dependence of the photo-induced absorption correlates well with the intensity dependences of the trap density and recombination time, quantities which until now were assumed to be constants.

Several novel photorefractive scattering processes were also studied. Isotropic scattering of a single intense pump beam was observed and modeled. Numerical calculations, performed using material parameters consistent with the previous experiments, yielded scattering cross sections in excellent agreement with the observations. Anisotropic scattering of a single extraordinary polarized beam into conical rings of light was also observed. Using a phase matching condition and the electrooptic tensor symmetry properties of $BaTiO_3$, the scattering process of the inner ring was uniquely determined. A model which describes the formation of the outer ring was also proposed.

Anisotropic scattering into higher orders were observed. To derive approximate solutions for the higher order gratings a perturbation technique was used to modify the transport equations. The measurements were found to be well described by the model. Finally, a new anisotropic four-wave mixing configuration was demonstrated. It was shown that amplified reflection could be performed without phase conjugation.

Contents

1 Introduction

1.1 The Photorefractive Effect

The wide spread proliferation of laser technology and the growing interest in non-linear optics during the early sixties, led to an intensive search for new optical materials. This early research was primarily concerned with parametric wave-mixing, such as frequency doubling.[1,2] and parametric amplification.[3,4] Since these processes required a variety of phase matching conditions, many birefringent crystals, such as ammonium dihydrogen phosphate (ADP),[5] potassium dihydrogen phosphate (KDP),[6] and barium sodium niobate $Ba_2NaNb_5O_{15}$,[7] were examined. Unfortunately, the high optical intensities required for optical parametric processes were also a source of optical damage.[8]

In $LiNbO_3$ and $LiTaO_3$, this damage was manifest as distortions in the refractive index along the path of the beam.[8] which could be reversed by heating the crystal, or by flooding it uniformly with light. This damage was also found to be a function of total energy incident on the crystal. That is, short exposure times and high intensities gave the same effect as long exposure times and low intensities. The ability of the crystal to integrate the optical power indicated that some type of microscopic transport process could be involved. Since the refractive index damage was photo-induced, the term photorefractive was coined.

In a similar phenomenon, known as the photochromic effect, the optical absorption could be changed by the application of light. This change in the absorption was shown to be the result of photo-induced charge transfer between impurity ions in the crystal.[9,10] Since different valence states of the ions had different absorption spectra, spatially varying intensity patterns generated spatially varying absorption centers in the crystal. An extension of this model was used by Chen[11] to explain the optical damage seen in $LiNbO_3$.

In Chen's model, Fig. 1, charge trapped in defects or impurities in the band gap, is photoexcited in the high intensity regions of the crystal. The liberated carriers then migrate to the dark regions of the crystal, resulting in a redistribution of charge with the same spatial variation as the incident light. This redistributed charge has an associated space charge field which, in noncentrosymmetric crystals, induces a change in the refractive index through the linear electrooptic effect. Since the symmetry requirement for phase matching is the same as that for the electrooptic effect, no inversion symmetry, many materials of possible use in parametric wave mixing were found to be subject to photorefractive damage. Some of the materials found to be photorefractive include ferroelectric $BaTiO_3$,[12] $Sr_xBa_{1-x}Nb_2O_6$ (SBN),[13] $Ba_2NaNb_5O_{15}$,[14] and $KNbO_3$,[15] non-ferroelectric $Bi_{12}SiO_{20}$ (BSO),[16] and GaAs,[17] and organic polymers.[18] Also certain PLZT ceramics,[19,20] which possess only a second order (Kerr) electrooptic effect, have been found to be photorefractive.

Illumination

Dark

Conduction Band

Recombination

Photo-Ionisation

Valence Band
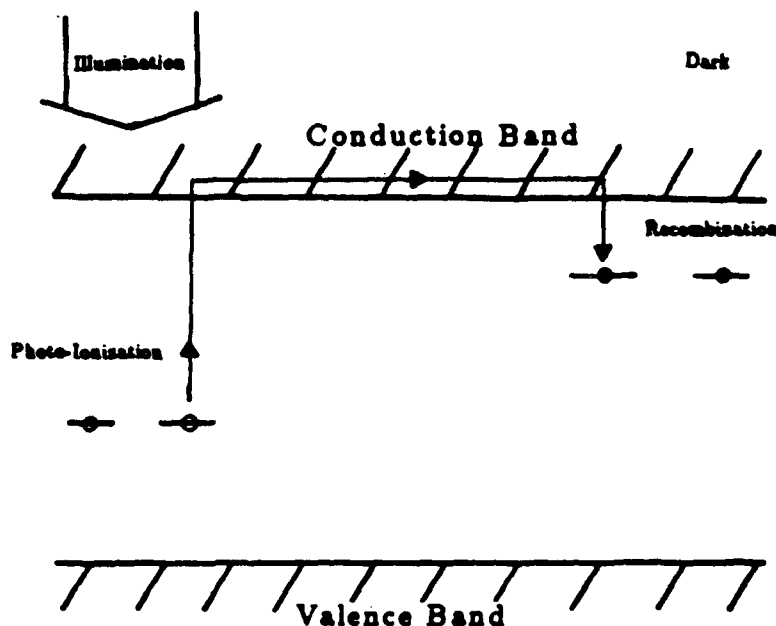
Figure 1: Basic mechanism of the photorefractive effect. Photoexcited electrons are redistributed, resulting in a space-charge field which modulates the refractive index through the electrooptic effect.

Chen was the first to devise the standard experiment for studying the photorefractive effect. He realized that the refractive index variations could be used to store phase holograms in the crystal.[21] In his experiment, the interference fringes of two coherent plane waves intersecting in the crystal, produced a pure phase grating through the photorefractive effect. This enables characterization of the effect in a crystal by measuring the diffraction efficiency of a light induced grating. In one experiment, more than 100 gratings were recorded in a $LiNbO_3$ crystal.[22]

Since this early work, the photorefractive effect has been used in a large number of nonlinear optical applications. The most widely known of these is optical phase conjugation.[23,24,25] This will be discussed in Chapter 6. Other applications include; image subtraction,[26] associative holographic memories,[27] phase-locking of lasers,[28] and optical bistability.[29] While many of these applications have shown great promise in the optical signal processing field, it is a promise which has so far been fruitless, since these applications are confined to relatively few research laboratories. Some of the reasons photorefractive materials have not been successfully integrated into useful devices are (1) a lack of a clear understanding of the photorefractive centers and their role in the photorefractive process, and (2) several anomalous photorefractive scattering processes that tend to degrade device performance. Other considerations are more in the nature of engineering problems such as the requirements of stability

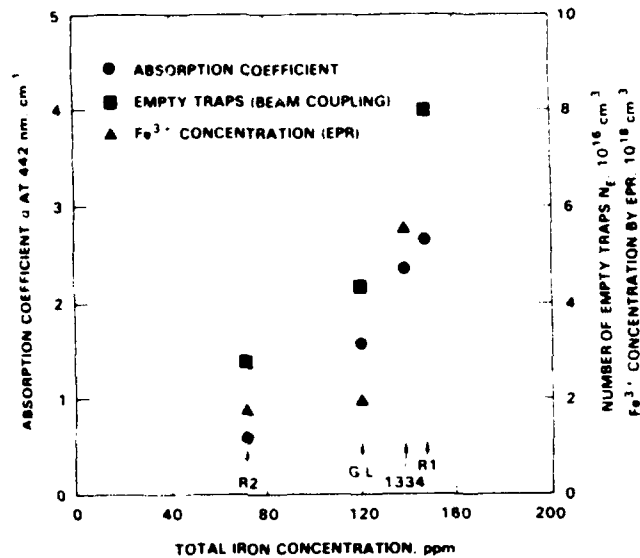Figure 2: Correlation between iron concentration and the photorefractive trap density in $BaTiO_3$. (After Ref. 34)

and coherence needed for holography.

Identification of the photorefractive species in $LiNbO_3$ was attempted in the early seventies by Peterson et al. [30] Their method was to combine a number of techniques such as electron spin resonance, oxidation and reduction, and optical absorption to correlate the affects of selected doping on the photorefractive properties. They measured the diffraction efficiency of undoped crystals and crystals doped with 450 ppm Fe. The diffraction efficiency of the doped crystals was found to be two orders of magnitude larger than the undoped crystals. After annealing in a reduced oxygen partial pressure the diffraction efficiency of all the crystals was smaller than that of the as-grown or air-annealed crystals.

Their ESR measurements indicated that the dominant valence state of the iron in the as grown crystal was Fe^{+3}. Since the reduced crystals showed both a decrease in the diffraction efficiency and a decrease in the Fe^{+3} ESR signal, they concluded that the predominant photorefractive species in $LiNbO_3$ was Fe^{+3}. Unfortunately, most of the early photorefractive work did not include light-induced grating erasure and although there has been some work on the erasure rate kinetics, [31, 32, 33] the intensity dependence of the erasure rate has not been reported. Therefore, it is not known if the decay rate of $LiNbO_3$ exhibits a sublinear intensity response. Also, photo-induced absorption effects were not reported.

The first attempts to determine the photorefractive species in $BaTiO_3$ were only recently attempted by Klein and Schwartz. [34] Their research was patterned after that of Peterson et al, [30] with the exception that they used beam coupling to characterize the photorefractive effect. Chemical analyses of the crystals showed

that iron was the predominant impurity in their commercial samples, although other transition metal impurities were also present. These iron concentrations also seemed to correlate to the Fe^{+3} ESR signals from the samples. Since the beam coupling results showed a linear correlation to the iron concentration, they concluded that iron was also the dominant photorefractive species in $BaTiO_3$. Their data showed a four-fold increase in the trap density for only a two-fold increase in the iron concentration Fig. 2.

This result however, is in direct conflict with the results of Schunemann et al. [35] and the work presented in this thesis. The origin of this conflict is not completely understood, however the crystals used in this work were grown from purified materials and systematically doped with varying amounts of iron, constituting a better control group.

Ducharme and Feinberg [36] conducted oxidation reduction experiments on similar commercially available samples of $BaTiO_3$. They found that the dominant carrier, which was holes in as grown and oxidized crystals, could be converted to electrons after reduction at 650°c at a partial pressure of 10^{-6} atm. The sublinear intensity dependence of the decay rate usually observed for $BaTiO_3$, [37] was observed for their as grown and oxidized crystals. However, the crystals which had been converted to n type exhibited a linear intensity dependence for the decay rate.

1.2 References : Section 1

1. P. A. Franken, A. E. Hill, and G. Weinreich, "Generation of optical harmonics,"Phys. Rev. Lett. $\underline{7}$, 118 (1961)

2. R. C. Miller, "Optical second harmonic generation in piezoelectric crystals," Appl. Phys. Lett. $\underline{5}$, 17 (1967)

3. J. A. Giordmaine, and R. C. Miller, "Tunable coherent parametric oscillation in $LiNbO_3$ at optical frequencies," Phys. Rev. Lett. $\underline{14}$ 973 (1965)

4. C. C. Wang and G. W. Racette, "Measurement of parametric gain accompanying optical difference frequency generation," Applied Physics Lett. $\underline{6}$, 169 (1965)

5. G. E. Francois, "CW Measurements of the optical nonlinearity of Ammonium Dihydrogen Phosphate," Phys. Rev. $\underline{143}$, 597 (1966)

6. S. A. Akhmanov, A I. Korrigin, V. A. Kolosov, A. S. Piskarskas, V. V. Fadeev, and R. V. Khokhlov, "Tunable parametric light generator with KDP crystal," Sov. Phys. J. Expt. Theor. Phys. Lett. (Engl. transl.), 3, 241 (1966)

7. J. E. Geusic, H. J. Levinstein, J. J. Rubin, S. Singh, and L. G. van Uitert, "Continuous 0.532-μ solid state source using $Ba_2NaNb_5O_{15}$," Appl. Phys. Lett. $\underline{12}$, 306 (1968)

8. A. Ashkin, G. Boyd, J.M. Dziedzic, R.G. Smith, A.A. Kallman, J.J. levinstein, and K.Nassau , "Optically-Induced Refractive Index Inhomogeneties in $LiNbO_3$ and $LiTaO_3$, Appl. Phys. Lett. $\underline{9}$, 72 (1966)

9. B. W. Faughnan and Z. J. Kiss, "Photoinduced reversible charge-transfer processes in transition-metal-doped single-crystal SrTiO3 and TiO_2," Phys. Rev. Lett. $\underline{21}$ (1968)

10. B. W. Faughnan and Z. Kiss, "Optical and EPR studies of photochromic $SrTiO_3$ doped with Fe/Mo and Ni/Mo," IEEE J. Quantum Electron. $\underline{5}$, 17 (1969)

11. F.S. Chen, "Optically Induced Change of Refractive Index in $LiNbO_3$ and $LiTaO_3$ ", J. Appl. Phys. $\underline{40}$, 3389 (1969)

12. R. L. Townsend and J. T. LaMacchia, "Optically Induced Refractive Index Changes in $BaTiO_3$" , J. Appl. Phys. $\underline{41}$, 5188 (1970)

13. J. B. Thaxter, "Electrical Control of Holographic Storage in Strontium-Barium Niobate", Appl. Phys. Lett., $\underline{15}$, 210 (1969)

14. J. J. Amodei, D. L. Staebler, and A. W. Stephens, "Holographic Storage in Doped Barium Sodium Niobate", Appl. Phys. Lett. $\underline{18}$, 507 (1971)

15. P. Gunter, U. Fluckiger, J. P. Huingnard, and F. Micheron, "Optically Induced Refractive Index Changes in $KNbO_3$:Fe ", Ferroelectrics 13, 297 (1976)

16. M. Peltier and F. Micheron, "Voiume Hologram Recording and Charge Transfer Process in $Bi_{12}SiO_{20}$ and $Bi_{12}GeO_{20}$ ", J. ppl. Phys. 48, 3683 (1977)

17. M. B. Klein, "Beam Coupling in Undoped GaAs at 1.06 mm Using the Photorefractive Effect ", Opt. Lett. 9, 35 (1984)

18. R. A. Bartolini, A. Bloom, and H. A. Weakliem, "Volume Holographic Recording Characteristics of an Organic Medium ", Appl. Opt. 15 (1975)

19. F. Micheron, C. Mayeux, A. Hermosin, and J. Nicholas, "Holographic Storage in PLZT Ceramics" ,J. Amer. Ceram. Soc. 57, 306 (1974)

20. J. W. Burgess, K. J. Hurditch, C. J. Kirkby, and G. E. Scrivener, " Holographic Storage and Photoconductivity in PLZT Ceramic Materials ", Appl. Opt. 15, 1550 (1976)

21. F. S. Chen, J.T. LaMacchia,and D.B. Fraser. "Holographic Storage in Lithium Niobate", Appl. Phys. Lett. 13, 72 (1969)

22. D.L. Staebler, W.J. Burke, W.Phillips, and J.J. Amodei. "Multiple Storage and Erasure of Fixed Holograms in Fe-Doped $LiNbO_3$" ,Appl. Phys. Lett. (1975)

23. J. Feinberg and R. W. Hellwarth. "Phase-conjugating mirror with continuous wave gain." Opt. Lett. 5, 519 (1980)

24. R. Hellwarth. "Generation of time-reversed wave fronts by nonlinear refraction." J. Opt. Soc. Am. 67, 1 (1977)

25. A. Yariv and D. Pepper, "Amplified reflection, phase conjugation, and oscillation in degenerate four-wave mixing." Opt. Lett. 1, 16 (1977)

26. S. Kwong, G. Rakuljic. and A. Yariv, "Real time image subtraction and "exclusive or" operat n using a self-pumped phase conjugate mirror." Appl. Phys. Lett. 48, 20 (1986)

27. B. H. Stoffer, G. J. Dunning, Y. Owechko, and E. Marom, "Associative holographic memory with feedback using phase-conjugate mirrors," Opt. Lett. 11, 118 (1986)

28. J. Feinberg and G. D. Bacher. "Phase-locking lasers with phase conjugation," Appl. Phys. Lett. 48, 3 (1986)

29. R. W. Eason and A. M. Smout, "Bistability and noncommutative behavior of multiple beam self-pulsing and self-pumping in $BaTiO_3$," Opt. Lett. 12, 51 (1986)

30. G. E. Peterson, A. M. Glass, and T. J. Negran, "Control of the susceptibility of lithium niobate to laser-induced refractive index changes," Appl. Phys. Lett. 19, 130 (1971)

31. J. K. Tyminski and R. C. Powell, "Analysis of the decay dynamics of laser induced gratings in $LiNbO_3$," J. Opt. Soc. Am. B2, 440 (1985)

32. J. Baquedano, M. Carrascosa, L. Arizmendi, and J. Cabrera, "Erasure kinetics and spectral dependence of the photorefractive effect in $Fe:LiNbO_3$," J. Opt. Soc. Am. B 4, 309 (1987)

33. M. Carrascosa, and F. Agullo-Lopez, "Kinetics of optical erasure of sinusoidal holographic gratings in photorefractive materials," IEEE J. Quan. Electron. 22, 1369 1986

34. M. B. Klein and R. N. Schwartz, "Photorefractive effect in $BaTiO_3$: microscopic origins," J. Opt. Soc. Am. B 3, 293 (1986)

35. P. G. Schunemann, D. A. Temple, R. S. Hathcock, H. L. Tuller, H. P. Jenssen, D. R. Gabbe,and C. Warde, "Photorefractive effect in high purity $BaTiO_3$," Conference on Lasers and Electro-Opt., Technical Digest Series 14, 178 1987.

36. S. Ducharme and J. Feinberg , " Altering the Photorefractive Properties of $BaTiO_3$ by Reduction and Oxidation at 650 °C " , J. Opt. Soc. Am. B 3, 283 (1986)

37. S. Ducharme and J. Feinberg , " Speed of the photorefractive effect in a $BaTiO_3$ single crystal," J. Appl. Phys. 56, 839 (1984)

2 Barium Titanate:Physical Properties and Crystal Growth

The electrical and optical properties of Barium titanate have been studied intensively over the past forty years with much of this work performed at the MIT Laboratory for Insulation Research. This section primarily serves to give background on the material properties of $BaTiO_3$ relevant to the photorefractive effect.

2.1 Physical Properties

Above 130 °C, barium titanate exists in the cubic perovskite structure, ABO_3, shown in Fig. 2.1. [1] In this structure, the Ti^{4+} ions (B), are at the center of six O^{2-} ions forming regular octahedrons. The octahedrons are connected at the corners with Ba^{2+} ions, (A), occupying holes in this framework. Each Ba^{2+} ion is surrounded by twelve equidistant O^{2-} ions.

As the temperature is lowered below 130 °C, $BaTiO_3$ experiences three first order ferroelectric phase transitions. At 130 °C the unit cell becomes distorted along a [100] direction and the crystal symmetry reduces to tetragonal 4mm. It is believed that the Ti and O ions move to new equilibrium positions in opposite directions [see Fig. 4] resulting in a net polarization. This model was shown to fit neutron and x-ray diffraction data with the barium ions not contributing to the polarization. [1] Since this shift can occur in any one of six directions, cooling through the Curie temperature causes simultaneous nucleation of multiple domain structures in the crystal.

The first order electrooptic effect has it's origin in the quadratic electrooptic effect. To understand this consider the cubic structure of $BaTiO_3$ above 130 °C. In this phase the refractive index is isotropic. However, if we apply an electric field to the crystal we can induce birefringence through the quadratic electrooptic effect [2]

$$\Delta \left(\frac{1}{n^2} \right) \propto P^2 . \tag{1}$$

In this case the polarization P is the result of the applied field E.

Now consider the same $BaTiO_3$ crystal below 130 °C. In this tetragional phase there is a spontaneous polarization P_s and from Eq. 1 we expect that the crystal should be naturally birefringent. When an electric field E is applied to the crystal the net polarization P is composed of both the spontaneous polarization P_s and the polarization due to applied fields P_E. From Eq. 1 we see that the change in the refractive index now has several terms with

$$\Delta \left(\frac{1}{n^2} \right) \propto P_s^2 + P_E^2 + P_s P_E . \tag{2}$$
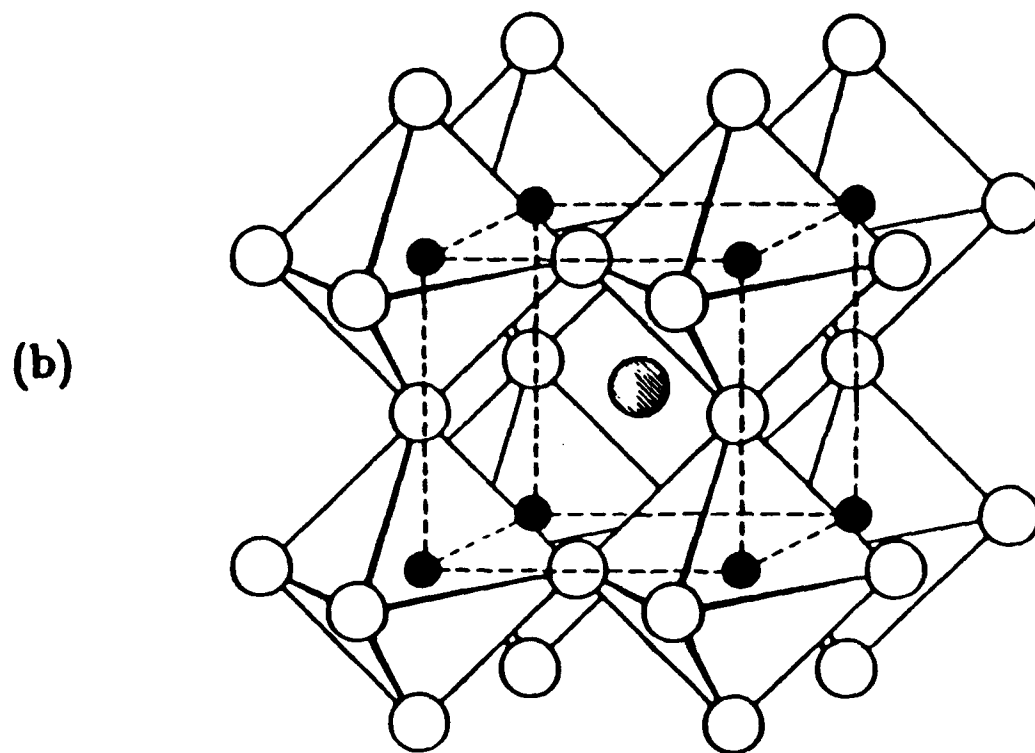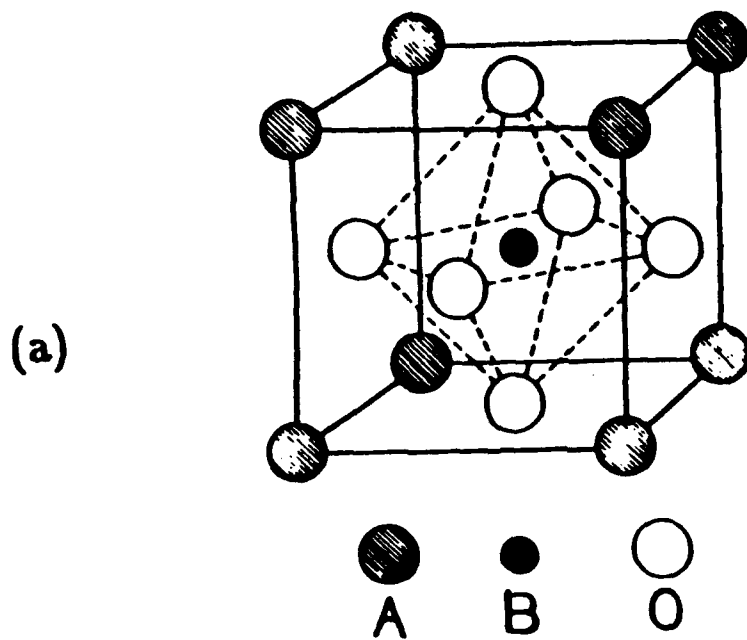
(a)

A   B   O

(b)

Figure 3: Perfect perovskite structure showing (a) the unit cell centered around the Ti^{+4} ion, and (b) the TiO_6 octahedra surrounding the Ba^{+2} ion. (After Ref. 1).
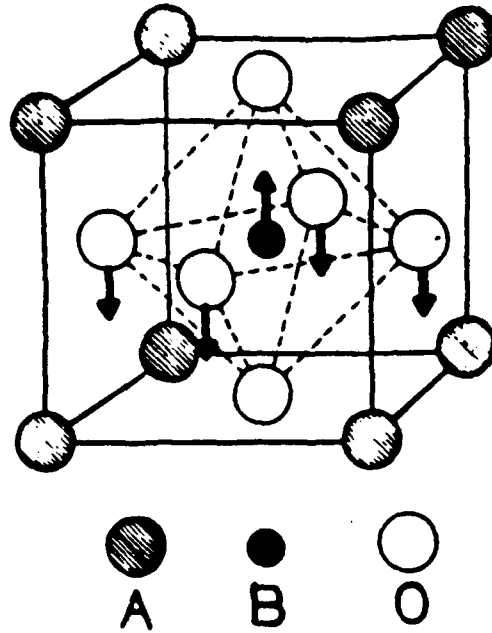
Figure 4: Ionic displacement in tetragonal $BaTiO_3$.

As stated, the natural birefringence is due to the spontaneous polarization P_s, with n_o-$n_e \propto P_s^2$. For small applied fields we can neglect the P_E^2 term. This leaves the cross term which is known as the first order electrooptic effect. Taking into account the tensoral properties of the crystal, the electrooptic effect can be written as [3]

$$\Delta n_{ij} = -\frac{n_i^3}{2} r_{ijk} E_k \tag{3}$$

where r_{ijk} is known as the electrooptic tensor. Using the symmetry properties of the tetragonal phase 4mm, the allowed tensor elements are $r_{131}=r_{311}=r_{232}=r_{322}$, $r_{113}=r_{223}$, and r_{333}. [3]

The two remaining phase transitions are found to be very destructive. Below 5 $°C$, the unit cell distorts to mm orthorombic symmetry with the spontaneous polarization along the [110] directions. Finally, below -90 $°C$, the spontaneous polarization is along the [111] direction with 3m trigonal symmetry.

The room temperature tetragonal phase is the one of interest to most optics researchers since its both ferroelectric and electrooptic with only a only a slight elongation of the unit cell in the polar direction.

2.2   Crystal Growth and Preparation

At present, the best technique of growing single crystalline $BaTiO_3$ is the top-seeded solution growth technique developed at the MIT Crystal Physics and Optical Electronics Laboratory. In this method, a solution of BaO and TiO_2 is prepared using

the phase diagram shown in Fig. 6(a). A composition of 66%TiO_2 and 34%BaO is found to give the widest growth range. The furnace, Fig. 2.2, is heated by silicon carbide heating elements and the thermal gradients are kept low by insulating fire bricks. The temperature is raised to approximately 1400 $^\circ$C and a [100] seed of $BaTiO_3$ is introduced into the furnace above the melt. After equilibrium is reached, the seed is introduced into the melt. To initiate growth, the temperature is slowly lowered at approximately 0.4 $^\circ$C/hr. After 5 to 10 hours, the seed is pulled from the melt at a rate of 0.2 to 1.0 mm/hr. After about 60 hours of pulling, the crystal is removed from the melt and the furnace slowly cooled to room temperature.

Because of the large differences in the size of Ba and Ti ions, doping is expected to be highly site selective. For instance, the transition metals are all similar in radius to the Ti ion, while the rare earth ions are closer in radius to the Ba ion. Therefore Fe^{+3} would be expected to be incorporated in the lattice at the Ti^{+4} site, while Ce would probably reside in the Ba site.

The first attempt at doping was made on crystals grown from a melt containing reagent grade TiO_2 and $BaCO_3$. These crystals were light green in color before doping. The addition of 20 ppm Cr to the melt, {$0.66[(1-x) TiO_2 + x Cr_2O_3] + 0.34 BaO$}, resulted in crystals which were very dark red in color. Although these were not useful for the normal photorefractive studies, the strong beam fanning discussed in Chapter 6 was first seen in these crystals.

The second doping attempt was made on crystals known as nominally pure, that is, they were grown from a melt containing relatively pure TiO_2 and reagent grade $BaCO_3$. Crystals of this type are the same as those reported in the literature. These crystals were found to have a light yellow-orange color. The addition of 20 ppm Ce to the melt, [$0.66TiO_2 + 0.34(1-x)BaO + 0.34(x)CeO_2$], resulted in moderately dark red samples. Strong beam fanning was observed in the Ce doped samples and photorefractive characterization was again hindered.

The third attempt at doping was performed by Peter Schunemann on a melt containing TiO_2 which he purified through a distillation process and $BaCO_3$ purified by David Gabbe through a solvent extraction processes. The undoped crystals showed very little absorption in the visible. The doped crystals were prepared by substituting Fe for Ti in the melt [$0.66(1-x)TiO_2 + 0.66(x/2)Fe_2O_3 + 0.34BaO$] where x is the doping level. The melt doping levels were 50 ppm, 500 ppm, and 1000 ppm. The color of the as-grown doped samples varied from light yellow for the 50 ppm to brown for the 1000 ppm. The visible absorption in 50 ppm and 500 ppm crystals was small enough to allow photorefractive characterization.

Crystal growth from a $BaTiO_3$ Ba_2O_4 melt [see Fig. 6(b)] was also attempted. This has the potential of increasing the growth range and lowering the growth temperature. In this case only one growth run was attempted. The composition used was [$0.4B_2O_3 + 0.6TiO_2 + BaO$] and the resulting seeding temperature was 1287°. This melt seemed to be extremely viscous and the resulting crystal was simply a mass of dendritic growth. However, recently crystals have been successfully grown
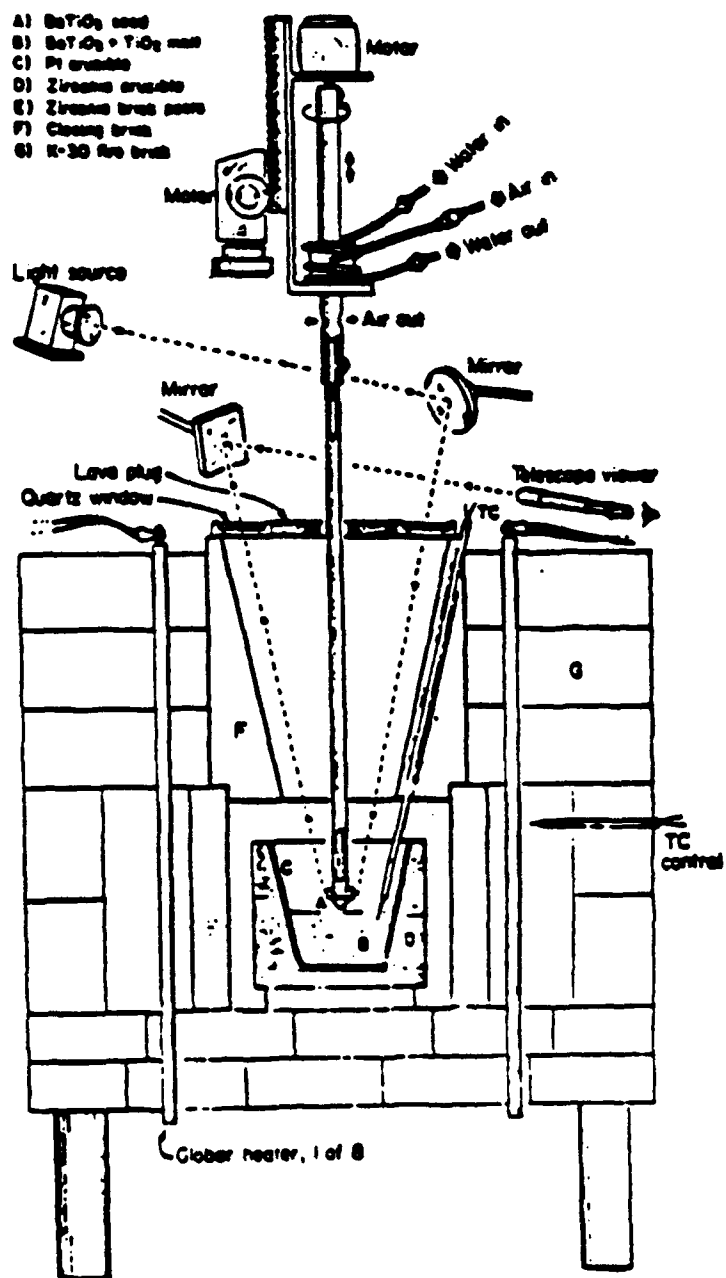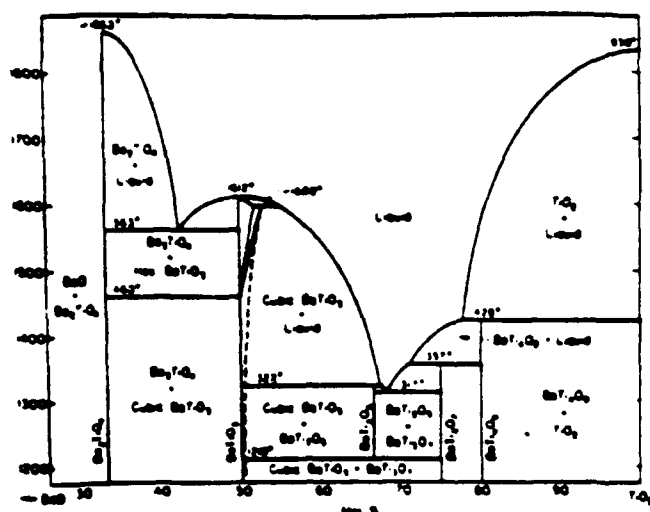
Figure 5: Schematic diagram of a typical furnace used for top-seeded solution growth of oxide crystals. (After Ref. 4).

(a)
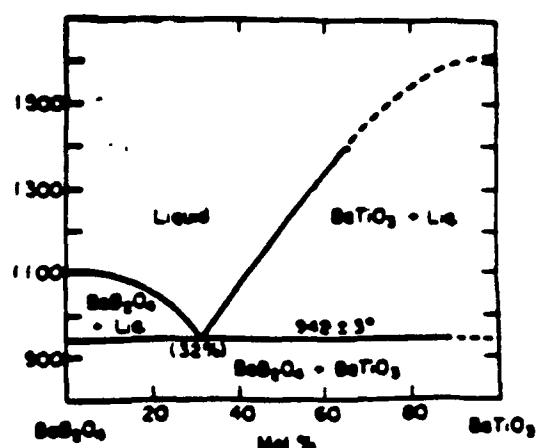
(b)

Figure 6: (a) The BaO-TiO_2 phase diagram and (b) the BaB_2O_4-$BaTiO_3$ phase diagram. (After Refs. 6 and 7)

from a similar melt by David Gabbe. [5]

As a final note, a weighing error by the author lead to a melt with approximately a 50/50 BaO/TiO_2 ratio. This resulted in a crystal which was extremely cracked and very unsymmetric. X-ray diffraction data taken by David Gabbe showed this crystal to have a hexagonal structure as expected by the phase diagram Fig. 6(a).

Since the Curie point is around 130 $^{\circ}$C, crystals cut from the boules are found to have twinning of 90° domains as shown in Fig. 7. These crystals are cut along [100] directions and polished first with 20 micron grit and then 3 micron diamond paste. The domains are eliminated by two methods. First the samples are subjected to hydrostatic pressure alternately along two perpendicular axes to eliminate the twinning. After each cycle the crystal must be repolished due to surface changes which can result in cracking if the poling were continued. This mechanical poling removes the 90° domains leaving only the domains which are 180° apart. These are aligned by heating the crystal near or above the Curie temperature, applying an electric field of approximately 1000 V/cm, and then slowly cooling the sample back to room temperature. Figure 8(a) shows the typical domain structure of an unpoled crystal placed between cross polarizers. Figure 8(b) shows the same crystal after mechanical and electrical poling with the c-axis parallel to the page and the long axis of the crystal. The size difference is due to the successive repolishing of the crystal during the poling cycles.
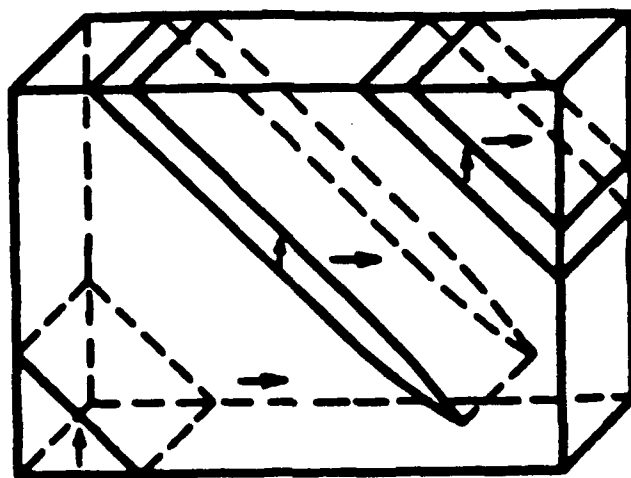
Figure 7: Domain twinning in BaTiO$_3$. The arrows denote the polar axis (After Ref. 1).
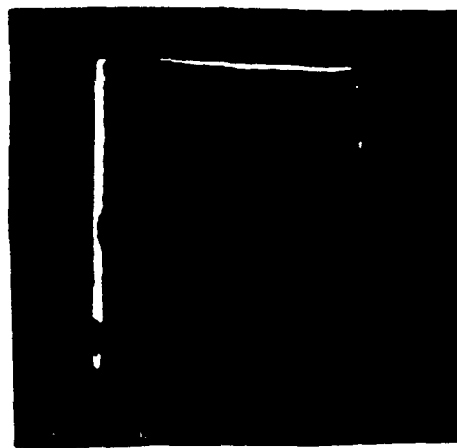
(a)   **(b)**

Figure 8: Photographs of a BaTiO$_3$ crystal (a) unpoled and (b) poled. The crystal was placed between crossed polarizers and in (b) the c-axis is parallel to the page.

Three samples doped with 50 ppm, 500 ppm, and 1000 ppm Fe were electroded on the c faces, placed in a quartz tube and annealed at 800 °C in an argon atmosphere with 100 ppm oxygen (10^{-4} atm) for 36 hours. The samples were then quenched to 175 °C by moving the quartz tube to another furnace at 175 °C. A poling field was then applied and the temperature slowly lowered to room temperature at a rate of approximately 5 °C/hour. [9, 8]

2.3 References : Section 2

1. A. von Hippel, *Dielectrics and waves* , (The MIT Press, Cambridge Massachusetts 1954)

2. G. Burns, Solid State Physics, (Academic Press, Inc. New York, 1985)

3. J. F. Nye, Physical properties of crystals, (Oxford University Press, London 1957)

4. V. Belruss, J. Kalnajs, A. Linz and R. Folweiler, "Top-Seeded solution growth of oxide crystals from non-stoichiometric melts," ater. Res. Bull. 6, 899 (1971)

5. David Gabbe, (private communication)

6. D. E. Rase and R. Roy, J. Am. Ceram. Soc. 38, 111 (1955)

7. Y. Goto and L. Cross, Yogyo Kyokai Shi 77, 355 (1969)

8. P. G. Schunemann, D. A. Temple, R. S. Hathcock, C. Warde, H. L. Tuller, and H. P. Jenssen, "Effects of iron concentration on the photorefractive properties of $BaTiO_3$," Accepted for publication in the J. Opt. Soc. Am. B Feature Issue on Photorefractive Materials, Effects and Devices, August 1988.

9. Peter Schunemann, Masters Thesis, MIT (1987)

3 Role of Iron Centers in the Photorefractive Effect in Barium Titanate

Role of iron centers in the photorefractive effect in barium titanate

P. G. Schunemann,* D. A. Temple, R. S. Hathcock, H. L. Tuller, H. P. Jenssen, D. R. Gabbe, and C. Warde

Crystal Physics and Optical Electronics Laboratory, Massachusetts Institute of Technology, Cambridge,
Massachusetts 02139

Variably valent iron impurities have been suggested as the source of photorefractive charge carriers in BaTiO. High-purity BaTiO crystals were grown with transition-metal impurity levels below the 10^{15} cm baseline estimated for photorefractivity. Iron-doped crystals were grown with concentrations of 5, 50, 250, 500, 750, and 1000 parts in 10^6 of iron. Changes in iron valence monitored by optical absorption in the P_0 range $1-10^{-4}$ atm were found to be consistent with a defect-chemical model indicating Fe^{4+} and Fe^{4+} to be the stable valence states in this range. Photorefractive characterization of high-purity BaTiO suggests that variably valent iron ions are not the dominant photorefractive species in these crystals, whereas the role of iron centers in doped crystals is complicated by large absorption losses.

INTRODUCTION

BaTiO$_3$ is of particular interest among photorefractive materials because it has demonstrated the highest four-wave mixing reflectivities (greater than a factor of 20) by virtue of its large electro-optic coefficients.[1,2] Despite the promise of barium titanate for applications involving phase conjugation and optical information processing, the centers responsible for the photorefractive effect in this material have not been conclusively identified, and this lack of understanding hinders the control and optimization of its nonlinear-optical and photorefractive properties.

The basic physics of the photorefractive effect is currently well understood[3]: (1) When the material is nonuniformly illuminated, carriers (electrons or holes) are optically excited from energy levels (donors or acceptors) in the band gap; (2) the excited carriers migrate by diffusion and drift and are retrapped and reexcited until they reach the less bright regions of the material; (3) this redistribution of charge creates internal electric fields that modulate the refractive index of the material through the electro-optic effect. The exact identity of the photorefractive sources and traps, however, remains unclear for BaTiO$_3$.

Previous efforts to isolate the photorefractive centers in BaTiO$_3$ have focused mainly on nominally undoped crystals from a single commercial source.[4] Klein and Schwartz[5] determined the impurity concentrations in a series of such crystals by chemical analysis and noted a general increase in the photorefractive trap density, Fe^{3+} electron paramagnetic resonance (EPR) signal, and absorption coefficient with increasing iron content over a narrow concentration range [~50–150 parts in 10^6 (ppm)]. On the basis of their observations and similar results reported for LiNbO$_3$,[6,9] Klein and Schwartz concluded that Fe^{3+} and Fe^{2+} are the sources and traps, respectively, of photorefractive carriers when the carriers are holes (and vice versa for electrons). Reduction of the same crystals ($P_{O_2} = 10^{-8.1}–10^{-12}$ atm) yielded increases in photorefractive speed and a change in carrier sign from positive to negative. These were explained by a model

based on variations in the Fe^{2+}/Fe^{3+} ratio.[10] Ducharme and Feinberg[11] reported the effects of oxidation and reduction at 650°C on a nominally undoped crystal and also noted a change in photorefractive carrier sign, which, in their crystal, corresponded to a minimum in trap density near 0.5 atm. These results led them to conclude that oxygen vacancies (or impurity–oxygen vacancy complexes) were the photorefractive donors of negative charge.

The only reported study of the photorefractive properties of intentionally doped BaTiO$_3$ is the recent work of Godefroy et al.[12] They measured the maximum diffraction efficiency, writing speed, and electro-optic coefficients in a series of crystals doped with a wide range of Fe concentrations (undoped to 2500 ppm). They reported that all measured parameters were highest in the 750-ppm Fe-doped crystal, with the diffraction efficiency increasing by a factor of 1000 over that of the undoped crystal. A major shortcoming of this work, however, is that the measured crystals were neither electrically nor mechanically poled, and the measurements that were performed are particularly sensitive to the presence of 90° and 180° domains. In fact, their reported investigations of the crystal-domain structure (performed using a unique optical topography approach) indicated a low degree of poling and notable variation among crystals.

The goal of this research was to gain more insight into the role of Fe centers, if any, in the photorefractive process in BaTiO$_3$ by controlling the concentration and valence states of the Fe in a series of crystals and by correlating the results with measured optical and photorefractive properties. Our approach is based on the popular theory[5] that variably valent transition-metal ions, in particular divalent and trivalent Fe impurities, are the species responsible for photorefractive charge carriers in BaTiO.

Our strategy for evaluating the effects of such centers on the photorefractive behavior of BaTiO was fourfold. Because it has been estimated that the density of charge carriers involved in the photorefractive effect is of the order of 10^{15}/cm[13] the first goal of this research was to prepare high-purity single crystals with transition-metal and aliovalent

impurity levels below this level. The second goal of this
work was to grow a series of Fe-doped BaTiO₃ single crystals
with low background impurity levels by systematically dop-
ing the melt from which the above-mentioned high-purity
crystals were grown. Third, we employed a defect-chemical
approach to control the Fe valence through thermal oxida-
tion and reduction treatments. Finally, these variations in
Fe concentration and valence were correlated with general
trends in the photorefractive behavior of the crystals as
characterized by saturation diffraction efficiency, light-in-
duced grating erasure rate, and two-beam coupling mea-
surements. Preliminary results of this study were recently
presented.[14][16]

HIGH-PURITY BARIUM TITANATE SYNTHESIS

Purification of Starting Materials

A major effort in this research was devoted to the synthesis
of high-purity starting materials because titanium dioxide
and barium carbonate feed materials are not commercially
available with impurity levels below the nominal concentra-
tion of 10^{16}/cm³, as is apparently required for photorefrac-
tivity.

The TiO_2 feed material was prepared by the hydrolysis of
titanium isopropoxide, $Ti(OC_3H_7)_4$, according to the reac-
tion

$$Ti(OC_3H_7)_4 + 3H_2O \xrightarrow{C_3H_7OH} TiO_2 \cdot H_2O + 4C_3H_7OH.$$

(1)
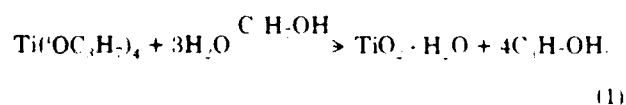
The titanium alkoxide precursor (Stauffer Chemical Com-
pany) was first purified by a reduced-pressure fractional
distillation. This purification technique was based on the
observation that titanium isopropoxide has a much lower
boiling point than the isopropoxides of other transition-
metal impurities.[17] A 600 mm × 12.5 mm vacuum-jacketed
distilling column packed with 1/8-in. (0.32-cm) glass helices
provided ~15–20 theoretical plates.[18] Purification was
qualitatively evidenced by the transformation of the alkox-
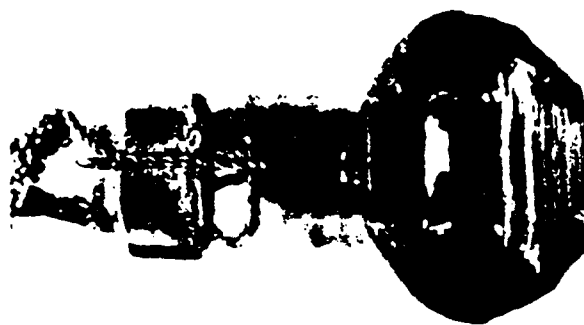ide from deep yellow to water clear in color, leaving a dark-

Fig. 2. Typical single-crystal boule grown by TSSG.

Fig. 3. Photograph of 90° domain walls (diagonal lines) in unpoled
BaTiO₃ single crystal.

brown liquid and metal particulates in the still pot. The
collected distillate was removed under a dry-nitrogen atmo-
sphere and was reacted with a dilute solution of deionized
water and semiconductor-grade isopropyl alcohol (Mal-
linckrodt) to form hydrated TiO_2 powder, which was then
vacuum dried in the same vessel. A flow chart for the pro-
cess is shown in Fig. 1(a).

Barium carbonate was formed by reaction of a purified
aqueous solution of $BaCl_2$ and urea, $(NH_2)_2CO$, with CO_2 in a
pressurized vessel. Reagent-grade $BaCl_2$ and urea were dis-
solved in water, filtered, and purified by solvent extraction.
In the solvent-extraction process the aqueous solution was
intimately mixed with a dense immiscible liquid phase
(chloroform) that contained an extracting or chelating agent
(diethylammonium diethyldithiocarbonate), which readily
forms complexes with a large number of metal ions. These
metal complexes segregated to the dense chloroform phase,
where their presence was indicated by a bright-yellow or
green color, and were subsequently removed by using a se-
paratory funnel. The extraction process was repeated for
several solution pH values until the extracting phase was
colorless. After extraction, the purified solution was refil-
tered and reacted under CO_2 pressure (1.03 × 10⁵ Pa,
~80°C) to form crystalline $BaCO_3$, which was centrifuged,
washed, and dried. A flow chart for the entire process,
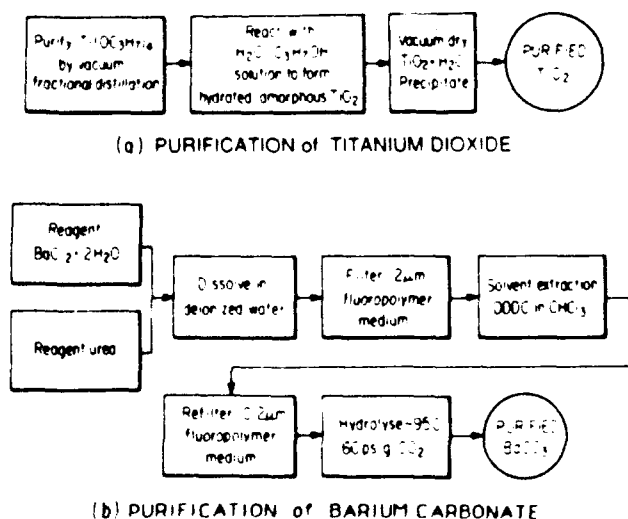carried out in a class 100 clean room, is shown in Fig. 1(b).

(a) PURIFICATION of TITANIUM DIOXIDE

(b) PURIFICATION of BARIUM CARBONATE

Fig. 1. Flow charts for (a) preparation of high-purity TiO₂ and (b)
purification and synthesis of BaCO₃

Single-Crystal Growth

High-purity $BaTiO_3$ single crystals were grown by the top-seeded solution growth (TSSG) technique.[19,20] Extreme care was exercised to minimize furnace contamination of the purified feed materials. The growth furnace was rebricked with new lining materials, new SiC heating elements were used, and the platinum crucible was kept covered while the closing bricks were lowered in place. Crystal growth was first initiated on a platinum wire to avoid contamination from an impure single-crystal seed. Later, high-purity single-crystal seeds cut in the {100} direction were used with dimensions of approximately 10 mm × 2.5 mm × 2.5 mm.

Single crystals were grown from a titanium-rich melt containing 66 mol % TiO_2, corresponding to a liquidus temperature of approximately 1380°C. (Experience has indicated that growth from melts at temperatures >1400°C yields poor results.) The melt was heated slowly at first to drive out moisture and was then raised from 200 to 1450°C in 20 h and soaked for 24–40 h to ensure complete dissolution of the ceramic powders. Seeding temperatures, indicated by equilibrium between the melt and the air-cooled seed, varied between 1382 and 1392°C for successful growth runs because of variations in the moisture content of the hydrated TiO_2. After seeding, the melt was cooled at 0.2°C/h for 25–35 h until pulling began at 0.15–0.2 mm/h. During pulling, the melt was cooled at 0.5°C/h to temperatures slightly above the eutectic (1320°C), after which the crystal was removed from the melt and slowly cooled to room temperature. Most growth runs yielded single-crystal boules of good optical quality, as shown in Fig. 2.

Optical Sample Preparation

Crystals were cut along {100} planes, as determined by the backreflection Laue method, and faces were ground to near parallel with 20-μm SiC. Cut and ground cubes were then polished by hand with 3-μm diamond paste on a lightly oiled paper lap. The presence of 90° domains in the polished samples was clearly indicated by sharp planar boundaries within the polished samples. These boundaries ran diagonally across the predominantly a faces, as shown in Fig. 3. These domain walls, in fact, served to identify the a faces, whereas the c direction was indicated by a characteristic color pattern when viewed between crossed polarizers.

Single-domain samples were achieved by a combination of mechanical and electrical poling. Uniaxial stresses of 10.3×10^6 to 20.7×10^6 Pa applied along an a axis were generally sufficient to remove all visible 90° domain walls. During application of the stress, performed by using a pressurized piston, the 90° domain walls visible in the unstressed a direction would migrate toward the corners of the crystal. This migration would create surface steps on faces along which the ends of the domain-wall boundaries moved. The moving domain walls would eventually get hung up on these surface steps so that the crystal needed to be repolished before poling could continue. After sufficient iterations, all directly visible 90° domain walls could be removed, although a cloudiness visible in crossed polarizers often revealed the presence of residual 90° domains. These were removed by applying an electric field of 1000 V/cm in an oil bath near or above the Curie temperature (133°C). Nickel electrodes were polished to optical flatness to ensure good electrical

Table 1. Spark-Source Mass Spectrographic Analysis of Reagent Precursors, Purified Feed Materials, and Resulting $BaTiO_3$ Single Crystals[a]

Element[b]	TiO (Unpurified)	TiO (Purified)	BaCl2 (Unpurified)	Urea (Unpurified)	BaCO3 (Purified)	BaTiO3
Li+	0.5		2		1	
B3+	2	3	2	0.2	1	5
Na+	≤2	≤2	2	0.5	2	≤2
Mg2+	2	2	1	≤1	5	2
Al3+	1	2	2	2	3	0.5
Si4+	5	5	4	10	4	4
P5+	0.1	0.03	0.2	0.1	0.1	0.05
S2-	<2	<2	<2	0.5	<2	<2
Cl-	10	3	Major	2	150	10
K+	2	2	≤0.2	0.1	2	≤0.1
Ca2+	3	5	200	3	250	2
Cr3+	0.06		≤0.02	≤0.02	0.05	≤0.02
Mn3+					≤0.02	≤0.02
Fe3+	2	0.5	0.3	0.2	1	0.3
Ni3+	0.3		0.1	≤0.04	≤0.04	0.04
Cu2+	0.1		≤0.02	≤0.02	0.06	
Zn2+			≤0.1		0.1	
As5+			0.5		0.05	0.1
Sr2+			30		20	50
Zr4+	0.1		<0.04		0.1	
Nb5+	0.03					
La3+			0.06		0.06	
Ce4+			≤0.02		≤0.02	
Pr3+					≤0.02	
Nd3+					≤0.08	
Pb2+			≤0.04		≤0.04	

[a] Quantities are given in parts per million atomic.
[b] Si^{4+}, Ca^{2+}, Sr^{2+}, Zr^{4+}, and Pb^{2+} are isovalent impurities.
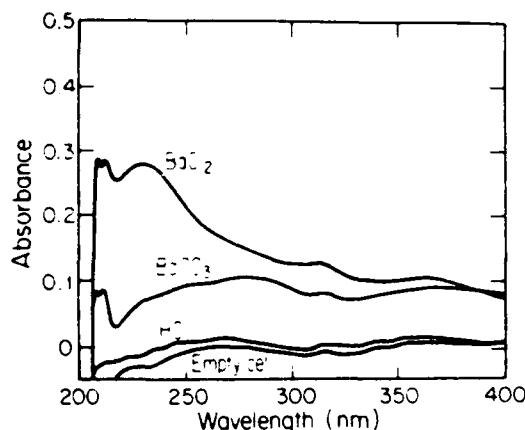
Fig. 4. Measured UV spectra of reagent BaCl, and purified BaCO dissolved in HCl. Peak at 230 nm corresponds to Fe impurities removed by solvent extraction.
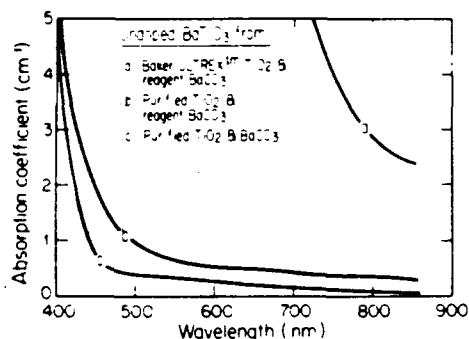

Fig. 5. Measured optical-absorption spectra comparing relative purity of BaTiO single crystals grown from commercial and purified feed materials.

1. The spark-source data indicated that the TiO fractional distillation procedure reduced the Fe content by a factor of 4 and removed all other transition metals to below detection limits.

2. UV spectrophotometric data of purified $BaCO$ and the reagent $BaCl_2$ precursor dissolved in HCl (Fig. 4) indicated that the absorbance due to transition-metal chloro-complexes in the $BaCO_3$ is significantly lower than in the $BaCl_2$. The peak at 230 nm in the $BaCl_2$ spectra corresponds well to the Fe peak reported in the literature.[21] In contrast, then, to the mass spectrometric data, which gave Fe concentrations of 0.3 and 1 ppm in $BaCl_2$ and $BaCO_3$, respectively, these results show that the $BaCO$ purification process significantly reduced the Fe levels of the $BaCl$ precursor.

3. Optical-absorption spectra of crystals grown from (a) reagent $BaCO$, and Baker Ultrex TiO_2, (b) reagent grade $BaCO_3$ and purified TiO_2, and (c) purified $BaCO_3$ and purified TiO synthesized in this laboratory (Fig. 5) reveal that the band edge of the high-purity crystal is shifted to a slightly shorter wavelength and drops off more steeply, both of which are indications of decreased impurity levels.

4. As indicated by mass spectrometry, transition-metal impurity levels in the high-purity $BaTiO_3$ single crystal are near or below the nominal concentration of $10^{16}/cm^3$ (1 ppm atomic $= 1.56 \times 10^{16}/cm^3$) predicted for observing the photorefractive effect. Fe and Ni were measured at concentrations of 0.3 and 0.04 ppm (atomic), respectively, whereas all other transition metals were below detection limits (0.01 ppm). The only aliovalent impurities reported at levels greater than this were B (5 ppm), Al (0.5 ppm), and Cl (10 ppm), which is a remnant of the $BaCl_2$ precursor. These results reveal that these high-purity $BaTiO_3$ crystals are, to our knowledge, the purest yet achieved in this laboratory or ever used for photorefractive studies.

SYSTEMATIC IRON DOPING

To investigate systematically the effects of Fe concentration on the photorefractive properties of $BaTiO_3$, crystals were grown from melt compositions containing 5, 50, 250, 500, 750, and 1000 ppm of Fe. Doping was accomplished by substituting FeO for TiO in the above-mentioned high-purity melt according to the proportion 34% $BaCO_3$ + 66% $[(1 - x)TiO_2 + (x/2)Fe_2O_3]$, where x is the doping level in parts in 10^6 (atomic). The Fe concentration, therefore, refers to the ratio Fe/Ti in the melt. The actual Fe concentrations in the resulting crystals were confirmed by chemical analysis. Atomic absorption analysis (Northern Analytical Laboratories) was conducted on the doped $BaTiO_3$ samples, which were dissolved by fusing with lithium tetraborate. The results are listed in Table 2 and indicate a segregation coefficient near unity. This value for the segregation coefficient is somewhat higher than that reported by Godefroy *et al.*[22] for TSSG $BaTiO_3$. Their Fe concentrations, however, were substantially higher than those used in this study, and the few data points at lower concentrations do suggest values approaching unity.

Single-domain optical samples of the Fe-doped crystals were prepared using the procedures described above for the case of high-purity crystals. Two notable differences in behavior, however, were observed during the electrical-poling procedure. First, crystals containing 500, 750, and 1000

contact, and voltage was applied slowly (10 V/min) to reduce the tendency toward surface cracking at the positive electrode, which sometimes occurs during rapid domain reorientation.

Critical factors in achieving poled $BaTiO$ samples proved to be (1) having a good polish so that moving domain walls would not hang up on surface flaws, (2) using multiple iterations during mechanical poling to avoid stressing and cracking, and (3) having stress-free single crystals. Residual stresses from cooling through the phase transition during crystal growth or stresses induced during mechanical polishing and poling could sometimes prevent complete mechanical poling and would often cause severe cracking during electrical poling.

Evaluation of Sample Purity

A combination of spark-source mass spectrometry (Northern Analytical Laboratory, Amherst, New Hampshire), UV spectrophotometry, and optical-absorption spectroscopy were used to confirm the impurity concentration levels in the starting materials, the purified feed, and the resulting high-purity $BaTiO$ single crystals. The results of spark-source mass spectrometry are listed in Table 1, and the UV spectrophotometric data and visible absorption spectra are given in Figs. 4 and 5, respectively. The results of these analyses can be summarized as follows:

Table 2. Chemical Analysis of Fe-Doped BaTiO₃ Single Crystals[a]

Sample Number	Iron Doping Level in Melt (ppm)	Iron Level in Crystal, Analyzed (ppm)[b]
1434	0	0.3[c]
1442	5	<10
1446	50	49
1453	500	530
1457	750	731
1462	1000	980

[a] Results indicate a segregation coefficient near unity.
[b] Atomic absorption (Northern Analytical).
[c] Spark-source mass spectrometry (Northern Analytical).

ppm of Fe were found to develop an unusual bright-yellow color band during application of the applied field (1000 V/ cm) at temperatures near the Curie temperature. T_c. This color band was defined by a sharp boundary parallel to the positive electrode, and with time this boundary propagated toward the negative electrode. A similar coloration phenomenon was apparently observed by Godefroy *et al.*[12] and prevented them from electrically poling their samples. Fortunately, in these experiments the color front advanced only 1 or 2 mm into the crystal in the times required for electrical poling (1.5–2.5 h), thereby leaving a region large enough for optical evaluation.

Electrocoloration phenomena were previously reported in both BaTiO₃ (Refs. 23 and 24) and SrTiO₃.[25] Blanc and Staebler[25] noted that the application of dc electric fields to transition-metal-doped SrTiO₃ in the temperature range of ~100–325°C resulted in the appearance of colored regions characteristic of oxidized material at the positive electrode and reduced material at the negative electrode. Their results were consistent with a simple model based on the drift of doubly ionized oxygen vacancies under the influence of the applied field, which caused oxidation and reduction of stationary transition-metal ions near the positive and negative electrodes, respectively. This effect was observed for all transition metals studied: Fe, Ni, Co, and Mo. Assuming that the same phenomenon occurs in our heavily doped BaTiO₃:Fe samples, we applied their analysis to our results to obtain an approximate value for the mobility of oxygen vacancies, μ_V, in BaTiO₃ given by

$$dx/dt = \mu_V V/x, \tag{2}$$

where dx/dt is the rate of the color boundary movement, x is the width of the untransformed region, and V is the applied voltage. This yielded a μ_V value of ~3 × 10⁻⁸ cm²/V sec at ~128°C, which compares favorably with the 1.5 × 10⁻⁸ cm²/ V sec obtained by Blanc and Staebler[25] for SrTiO₃ at 200°C.

The second effect of added Fe, which was noted during electrical poling, was a slight decrease in the Curie temperature evidenced by visual observation of the tetragonal-to-cubic phase transition. More-accurate Curie temperature measurements were performed using capacitance techniques on thin (100) slabs cut from high-purity, 50-, 500-, and 1000-ppm Fe-doped samples. These samples were equilibrated at 800°C in oxygen partial pressures of 1, 10⁻², and 10⁻⁴ atm, and in each case they were subsequently quenched to ~175°C and slowly cooled to ~125°C while the ac capacitance (100 kHz) was monitored. In each case the phase change was marked by a sudden plunge in the relative

dielectric constant from ~12,000 in the cubic phase to ~2,000 after the transition. The results indicated that the Curie temperature dropped approximately 2°C per 1000 ppm of Fe, in close agreement with the value of −21°C/ mol % reported by Hagemann and Ihrig.[26] Annealing in the oxygen partial pressure range indicated above had no significant effect on T_c, however, which is in agreement with the results of previous workers[26] as well as those of Weschler *et al.*[10] but is in sharp contrast with the results of Ducharme and Feinberg,[11] who noted a 6°C drop in T_c for annealing in argon as compared with oxygen.

CONTROL OF IRON VALENCE

Defect Chemistry of BaTiO₃:Fe

The understanding and control of the various valence states of Fe and their relative concentrations is clearly critical to evaluating the possible role of these centers in the photorefractive process in BaTiO₃. The defect chemistry of BaTiO₃[27-32] and in particular transition-metal-doped BaTiO₃[26,33-35] has been extensively studied by high-temperature electrical conductivity, thermogravimetry, Mössbauer spectroscopy, and EPR. The work of Hagemann and co-workers[26,33-35] on Fe-doped BaTiO₃ yielded the thermodynamic defect model presented below, which permits the concentrations of Fe²⁺, Fe³⁺, and Fe⁴⁺ to be determined as a function of oxygen partial pressure, temperature, and total Fe doping level.

When BaTiO₃ is treated at low oxygen partial pressures and elevated temperatures, oxygen vacancies are created and balanced by the generation of mobile electrons according to the reaction

$$O_O{}^x = \tfrac{1}{2}O_2 + V_O{}^{\bullet\bullet} + 2e', \tag{3}$$
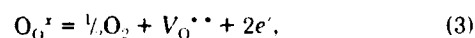
with an equilibrium constant for reduction given by

$$K_n = [V_O{}^{\bullet\bullet}]n^2 P_O{}^{1/2} = K_n{}'' \exp(-\Delta H_n{}''/kT), \tag{4}$$

where n is the electron concentration and $\Delta H_n{}''$ is the standard enthalpy of reduction associated with the formation of doubly ionized oxygen vacancies. The notation is that of Kroger and Vink,[16] where the cross, dot, and slash superscripts correspond to neutral, positive, and negative effective charges, respectively. The electroneutrality condition in this regime is simply

$$2[V_O{}^{\bullet\bullet}] = n, \tag{5}$$

where the atmosphere-controlled oxygen-vacancy concentration is much greater than the total Fe concentration.

At higher oxygen partial pressures, however, the oxygen-vacancy concentration becomes fixed by the total Fe concentration, depending on the stable valence state(s) present. For every two Fe⁴⁺ ions reduced to Fe³⁺, one oxygen vacancy is formed, whereas for every Fe²⁺ ion formed, one oxygen vacancy is generated. Consequently the condition of charge balance requires that

$$[Fe_{Ti}'] = 2[V_O{}^{\bullet\bullet}] \tag{6}$$

when trivalent and tetravalent iron are present or

$$[Fe_{Ti}'] + 2[Fe_{Ti}''] = 2[V_O{}^{\bullet\bullet}] \tag{7}$$

at lower P_O, where both Fe³⁺ and Fe²⁺ are present and are

represented by Fe_{T_i}' and Fe_{T_i}'', respectively. The relevant ionization reactions are given by

$$Fe_{T_i}'' = Fe_{T_i}' + e' \qquad (8)$$

and

$$Fe_{T_i}' = Fe_{T_i}^x + e'. \qquad (9)$$

These reactions have the corresponding mass-action relations[34,35]

$$[Fe_{T_i}']n/[Fe_{T_i}''] = K_D'' = 1/2N_c \exp[-(E_z - E_{Fe}^{2-})/kT], \qquad (10)$$

$$[Fe_{T_i}^x]n/[Fe_{T_i}'] = K_D' = 2N_c \exp[-(E_z - E_{Fe}^-)/kT]. \qquad (11)$$

where N_c is the density of states in the conduction band $(1.55 \times 10^{22} \text{ cm}^{-3})$, E_g is the band gap of $BaTiO_3$ (3.1 eV), and E_{Fe}^{2-} and E_{Fe}^- are the energy levels of Fe^{3+} and Fe^{4+}, respectively, as measured from the top of the valence band.

The concentration of Fe ions in a given valence state is related to the total Fe concentration through the mass-balance equation

$$[Fe_{T_i}]_{tot} = [Fe_{T_i}'] + [Fe_{T_i}^x] \qquad (12)$$

and

$$[Fe_{T_i}]_{tot} = [Fe_{T_i}''] + [Fe_{T_i}'] \qquad (13)$$

for oxidizing and reducing conditions, respectively.

The equilibrium defect model represented by Eqs. (3)–(13) can be used to predict the relative concentration levels of Fe^{2+}, Fe^{3+}, and Fe^{4+} quantitatively for a given set of annealing conditions and doping levels if values for the equilibrium constants K_n'', K_D', and K_D'' are known. The equilibrium constants were determined by thermogravimetric measurements,[34,35] and high-temperature-electrical conductivity measurements,[29–32] which give $K_n'' \sim 3 \times 10^{75} \text{ cm}^{-9} Pa^{1/2}$ and $\Delta H_n'' \sim 9.6 \times 10^{-19}$ J. The ionization energies were determined using thermogravimetry and Mössbauer spectroscopy by Hagemann.[35] These results yielded values for E_{Fe}^- and E_{Fe}^{2-} of 0.8 and 2.4 eV, respectively. These values inserted into Eqs. (4), (10), and (11) and combined with Eqs. (6) and (7) yield values for $[Fe^{2+}]$, $[Fe^{3+}]$, and $[Fe^{4+}]$ as a function of oxygen partial pressure and temperature. Results of such calculations for an equilibrium temperature of 800°C and the total Fe concentrations relevant to this study (0.3, 50, 500, and 1000 ppm) are plotted in Fig. 6.

A number of important trends are illustrated in Fig. 6. For each Fe concentration labeled at the left of the figure, the three plateaus going from left to right correspond to saturation of the Fe ions in the divalent, trivalent, and tetravalent states, respectively, with increasing P_{O_2}. Note that Fe^{4+} and Fe^{3+} are the predominant species under the relatively oxidizing atmospheres encountered during crystal growth, whereas the Fe^{2+} concentration is extremely low $(<10^{15} \text{ cm}^{-3})$ even for the highest Fe concentration and lowest P_{O_2} encountered in this study (1000 ppm of Fe, 10^{-4} atm). The specific P_{O_2}-dependent trends illustrated in Fig. 6 can be derived by combining Eqs. (4), (7), and (10) or Eqs. (4), (6), and (11) and differentiating with respect to log P_{O_2}. Performing this analysis yields

$$d \log[Fe^{4+}]/d \log P_O = -d \log[Fe^{2+}]/d \log P_O = 1/4 \qquad (14)$$
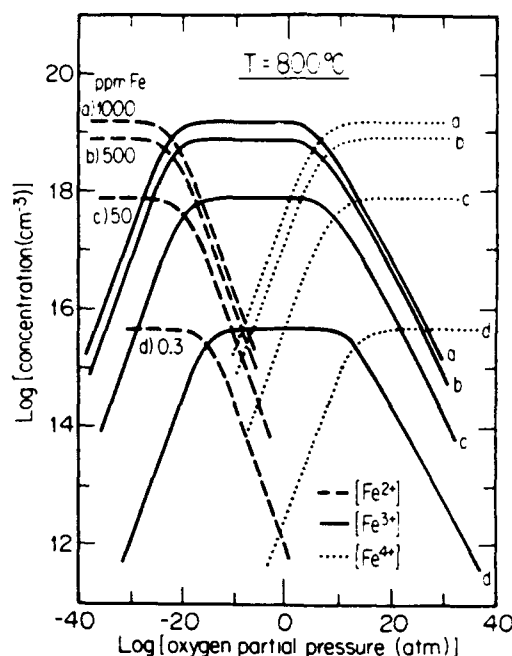

Fig. 6. Calculated variations in the concentrations of Fe^{2+}, Fe^{3+}, and Fe^{4+} as a function of oxygen partial pressure at various Fe concentrations for an equilibration temperature of 800°C.

for low values of P_{O_2}, whereas at higher values of P_{O_2}

$$d \log[Fe^{4+}]/d \log P_O = 1/4 \qquad (15)$$

and

$$d \log[Fe^{3+}]/d \log P_O = -1/6. \qquad (16)$$

Similar manipulation of these equations with respect to the total Fe concentration, $[Fe]_{tot}$, at a fixed P_{O_2} yields

$$d \log[Fe^{2+}]/d \log[Fe]_{tot} = 1/2 \qquad (17)$$

and

$$d \log[Fe^{4+}]/d \log[Fe]_{tot} = 3/2. \qquad (18)$$

[Equations (14)–(16) apply to the regions in Fig. 6 where the concentration of a given valence state is changing and break down as saturation is approached.] Note from Eqs. (17) and (18) that the concentration of a given valence state does not increase linearly with Fe content as one might intuitively expect. It is also notable that the Fe^{4+} concentration increases rather rapidly with Fe content, as compared with Fe^{2+}.

The above defect model governs the changes in oxygen-vacancy concentration in addition to Fe valence. These are plotted in Fig. 7 as a function of oxygen partial pressure for the same conditions as those in Fig. 6. Note that the oxygen-vacancy concentration is fixed over a wide P_{O_2} range by the Fe^{3+} concentration according to Eq. (6). At lower P_{O_2} values, however, Eq. (5) dominates Eq. (7), and additional oxygen vacancies are charge compensated by conduction electrons, resulting in high electrical conductivity. Comparison with Fig. 6 reveals that this intrinsic compensation mechanism takes over before substantial Fe^{2+} can be formed. At high oxygen partial pressures, the oxygen-vacancy concentration reaches a plateau determined by the

level of background impurities, which in Fig. 7 is determined from the chemical analysis results in Table 1. An important consequence of the trends illustrated in Fig. 7 is that oxygen vacancies can be ruled out as the donors responsible for P_{O_2}-dependent changes in photorefractive properties because their concentration is fixed over a wide P_{O_2} range by the presence of acceptor impurities or dopants.

Finally, although the above trends apply at room temperature, some care should be taken in applying the actual defect concentrations shown in Fig. 6 to crystals at 25°C. In the case of oxygen vacancies, rapidly quenching the samples from 800°C effectively freezes in the high-temperature ionic defect structure so that the concentrations in Fig. 7 should still hold. The relative concentrations of Fe^{2+}, Fe^{3+}, and Fe^{4+}, however, depend on the degree of ionization of defects in the system, which is highly temperature dependent. On cooling, some deionization will occur, which, in the case of holes, will shift the curves in Fig. 6 to lower oxygen partial pressures, thus favoring the formation of higher oxidation states.

Optical Absorption Spectroscopy

The variations in Fe valence governed by the above model were monitored by optical-absorption measurements based on the characteristic spectra of Fe^{2+}, Fe^{3+}, and Fe^{4+} in BaTiO$_3$. Because no published absorption spectra were available for melt-grown BaTiO$_3$:Fe, results for Fe-doped SrTiO$_3$ (Ref. 35) served as a guide to the interpretation of our measured spectra. In SrTiO$_3$:2300 ppm Fe, Fe^{4+} charge-transfer bands have been associated with an absorption peak and shoulder at 440 and 590 nm, respectively, in oxidized samples ($P_{O_2} = 1$–10^{-4} atm), giving them a reddish-brownish color.[35] Under more reducing conditions ($P_{O_2} = 10^{-4}$–10^{-17} atm), Fe exists almost entirely in the trivalent state, leaving the same crystals nearly colorless. Significant amounts of Fe^{2+} are formed only in heavily reduced crystals ($P_{O_2} < 10^{-17}$) and have been associated with a double band with peaks at 1030 and 825 nm, which cause the crystals to appear greenish in color.[35]

Optical-absorbance measurements of our BaTiO$_3$:Fe samples yielded similar results. These were performed using a

Fig. 7. Calculated variations in oxygen-vacancy concentration versus P_O for different Fe doping levels and background acceptor levels in Table 1.
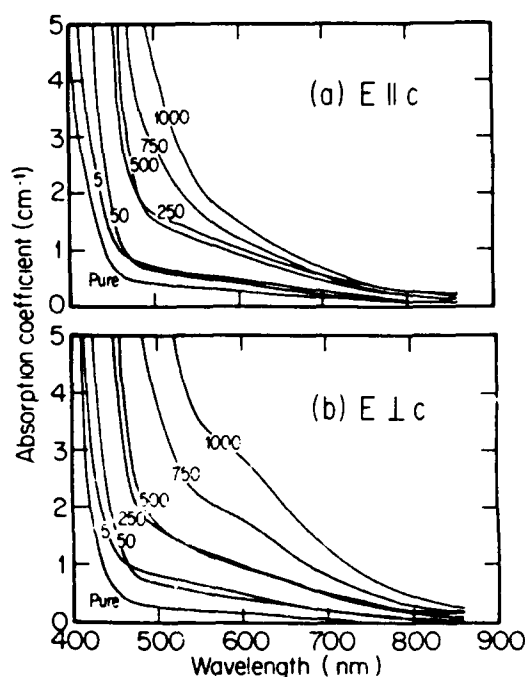

Fig. 8. Measured optical-absorption spectra as a function of Fe doping for as-grown crystals after mechanical poling: (a) E parallel to c, (b) E perpendicular to c.

Perkin-Elmer Lambda 9 double-beam spectrophotometer. Visible absorption spectra were measured between 380 and 860 nm on as-grown and annealed samples for light polarized parallel and perpendicular to the c axis. Automatic background correction compensated for the effects of matched polarizers and a 4-mm circular beam mask. The absorption spectra of the high-purity sample and of those doped with 5, 50, 250, 500, 750, and 1000 ppm of Fe were measured in the as-grown condition after mechanical poling, and the results are shown in Fig. 8. In each case the absorption coefficient α was calculated from the measured transmission T according to

$$\alpha = [2 \ln(1 - R) - \ln T]/d, \tag{19}$$

where d is the sample thickness and R is the reflectance, which is related to the refractive index by

$$R = (n - 1)^2/(n + 1)^2 \tag{20}$$

for the case of normal incidence.[37] Corrections for reflectance were made using Eq. (20) and the refractive-index data of Wemple et al.[38] for BaTiO$_3$ as a function of wavelength and polarization.

In Fig. 8 the effect of Fe doping on the absorption coefficient of as-grown crystals is clear. The data for $E \| c$ and $E \perp c$ are given in Figs. 8(a) and 8(b), respectively. These spectra are characterized by a broad absorption band, extending throughout the visible to the band edge, which increases with increasing Fe content. In addition, the extended band edge appears to shift to higher wavelengths with increasing Fe concentration. The $E \perp c$ polarization shows the emergence of a well-defined shoulder at 620 nm for Fe levels greater than 500 ppm. The slight inconsistencies in the observed trends (i.e., the intersection of the 5- and 250-ppm data with the 50- and 500-ppm curves) were due to scattering from residual 90° domain walls in the 5- and 250-
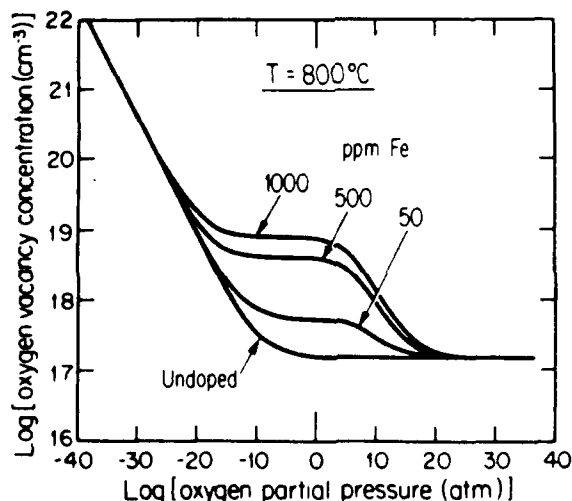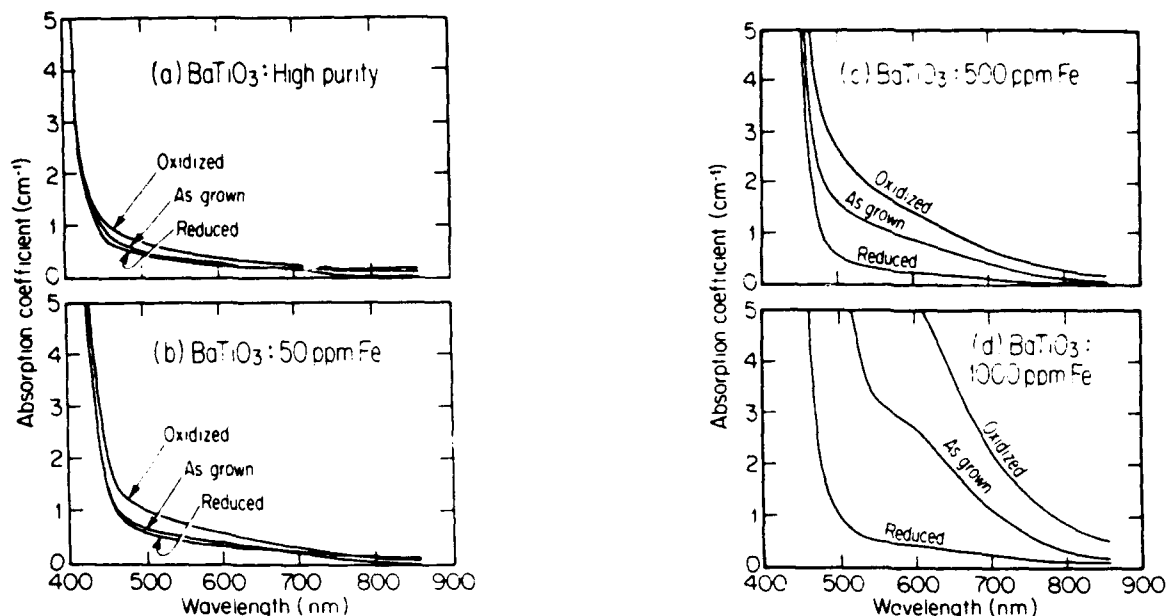
Fig. 9.   Effects of oxidation $(P_o = 1$ atm, 800°C) and reduction $(P = 10^{-4}$ atm, 800°C) on the absorption spectra of BaTiO₃ (a) high purity, (b) 50-ppm Fe, (c) 500-ppm Fe, (d) 1000-ppm Fe $(E$ perpendicular to $c)$.

ppm samples, which increased the measured absorbance. These inconsistencies were removed when electrical poling was performed; however, not all the samples shown survived this procedure.

A second set of samples from boules of high-purity, 50-, 500-, and 1000-ppm Fe were measured after annealing at 800°C in oxygen (1 atm) and in 100 ppm of O_2/Ar $(10^{-4}$ atm), respectively. Oxygen partial pressures were controlled by using premixed Ar/O_2 gases and were monitored by using a calcia-stabilized zirconia electrochemical oxygen sensor in series with the sample furnace.

Before annealing, the c faces of the samples were painted with platinum paste, and the crystals were mounted between platinum sheet electrodes in adjacent spring-loaded sample holders. The crystals were heated slowly through the Curie temperature (4–6°C/h) and then were heated to 800°C in 1 h. Samples were annealed for equilibration times based on the bulk diffusion data of Wernicke[19] (~36 h) and subsequently quenched to just above T, (where the oxygen diffusivity is negligible) in order to freeze in the high-temperature defect structure. Quenching was performed by transferring the gas-sealed quartz-glass tube from the split-tube furnace used for annealing to an adjacent furnace maintained at 175°C. A field of 1000 V/cm was gradually applied, and the crystals were slowly cooled through the Curie temperature (4–6°C/h) and then to room temperature before removing the field. This procedure eliminated the need for repoling after the high-temperature anneal.

The effects of oxidation (1 atm) and reduction $(10^{-4}$ atm) on pure, 50-, 500-, and 1000-ppm Fe-doped samples are shown in Fig. 9. Oxidation increased the height of the broad visible absorption band, turning the more heavily doped crystals a darker brown and the lightly doped crystals a slightly deeper yellow or amber. The effect of reduction was to reduce the height of the 620-nm band drastically, changing the heavily doped crystals from brown to yellow while leaving the high-purity crystal almost colorless.

An interpretation of Figs. 8 and 9 can be based on the
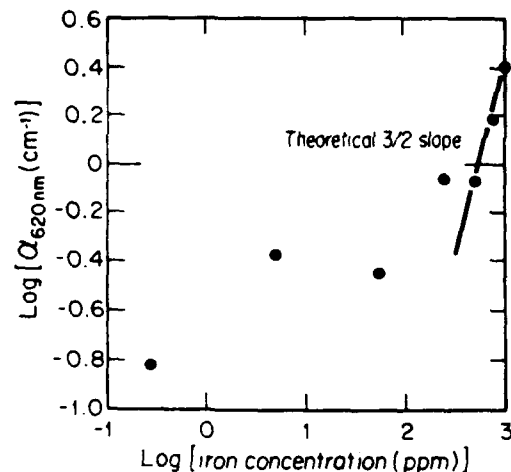
Fig. 10.   Log α_{620} versus log[Fe]..., illustrating the trend toward the theoretical 3/2 dependence at higher Fe concentrations where the 620-nm shoulder can be resolved.

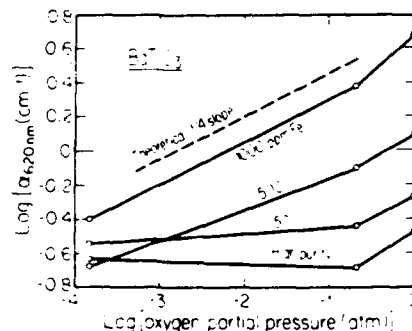Fig. 11. P_o dependence of the 620-nm absorption coefficient (Fe³⁺) approaching the predicted 1/4 slope with increasing Fe content.

previous identification of charge-transfer bands in $SrTiO_3$ and on the observed Fe concentration and P_{O_2}-dependent trends. The broad absorption band in the visible would then correspond to an Fe^{4+} charge-transfer band, with the 620-nm (2.0-eV) shoulder corresponding to the 590-nm feature in $SrTiO_3$:Fe. The shoulder in $BaTiO_3$ is shifted to slightly longer wavelength because of the differences in the crystal field. The analog to the 440-nm peak in the $SrTiO_3$ spectrum occurs at absorbances out of the range of the spectrometer for the sample thicknesses used (3–4.5 mm) and probably explains the apparent shifts in the band edge with increasing Fe content.

Qualitatively, the interpretation above conforms well with the proposed defect model. In the as-grown condition the Fe ions are present in both trivalent and tetravalent states, and the relative concentration of Fe^{4+} increases with increasing Fe content. This manifests itself as a nonlinear increase in the 620-nm absorption peak with increasing Fe content, as observed in Fig. 8(b). When the crystals are oxidized, more of the Fe^{3+} is converted to Fe^{4+}, and vice versa on reduction, resulting in the trends seen in Fig. 9. It is also significant to note that no absorptions corresponding to Fe^{2+} (825 nm in $SrTiO_3$) were observed even for the most reducing conditions investigated herein. This is consistent with the defect model's prediction concerning the low concentration of Fe^{2+} in these samples.

Quantitatively, the Fe concentration dependence and oxygen partial pressure dependence of the 620-nm absorption deviate somewhat from the Fe^{4+} concentration behavior predicted by the defect model, but the fit improves with increasing Fe content. Figure 10 shows that although the 620-nm absorption increases more gradually than predicted for Fe^{4+} at low Fe concentrations, the 3/2 slope predicted by Eq. (18) is closely followed in samples in which the 620-nm shoulder can be resolved (>500 ppm Fe). Similarly, the P_{O_2} dependence of the 620-nm absorption coefficient plotted in Fig. 11 is low in lightly doped samples but approaches the 1/4 slope predicted for Fe^{4+} [Eq. (15)] in the 500- and 1000-ppm Fe-doped samples.

PHOTOREFRACTIVE MEASUREMENTS

High-purity and Fe-doped $BaTiO_3$ crystals in the as-grown, oxidized, and reduced condition were characterized, using a variety of photorefractive techniques, and the observed trends were correlated with the variations in Fe concentration and valence described above. In all the experiments described below, an argon-ion laser operating in the TEM_{00} mode was used to write diffraction gratings in the samples, and a He–Ne laser ($\lambda = 633$ nm) was used to generate the readout beam when required. All measurements were taken at room temperature ($T = 295$ K).

Saturation diffraction efficiency measurements provided a preliminary estimate of the relative magnitude of the photorefractive activity in the various samples. These measurements were applied to high-purity 50-, 500-, and 1000-ppm Fe-doped crystals in the as-grown condition and to samples from the same boules that were oxidized ($P_{O_2} = 1$ atm) and subsequently reduced ($P_{O_2} = 10^{-4}$ atm). In these experiments gratings with a spacing of 2 μm ($\lambda = 514.4$ nm, $2\theta = 14°$; grating vector lying in the plane containing the c axis) were written in the samples, and the intensity of the diffracted readout beam was recorded as a function of time

until saturation was reached. The results for the 500-ppm Fe-doped crystal are shown in Fig. 12 and indicate that the saturation diffracted-beam intensity dropped by almost a factor of 10 when the crystal was oxidized while increasing by a lesser degree when it was reduced. Similar results were obtained for the 50- and 1000-ppm samples.

Additional saturation diffraction efficiency measurements were performed on the as-grown and reduced samples in which the data were normalized with respect to the incident intensity (1 μW/cm^2) of the 633-nm readout laser beam. The writing beams in this case were of wavelength 488 nm, with intensities $I_1 = 17$ μW/cm^2 and $I_2 = 870$ μW/cm^2, and were combined at an external angle, $2\theta = 27°$, by using the anisotropic configuration (grating vector $K \perp c$). The diffracted-beam intensities were measured by an EG&G photodiode. All samples were copolished to identical thicknesses of 4.5 mm $\pm$ 3% to permit direct comparison of the results, which are shown in Fig. 13 as a function of Fe concentration.

Two-beam-coupling measurements were used to determine the sign of the dominant carrier and the effective trap density for the pure as-grown and reduced crystals. In these experiments, the pump and signal beam ($\lambda = 488$ nm) were ordinary polarized with intensities of $I_P = 150$ mW/cm^2 and $I_S = 180$ μW/cm^2, respectively, thus keeping the modulation index $m = 2 (I_P I_S)^{1/2}/(I_P + I_S)$ small ($m \ll 1$) for compatibility with the standard photorefractive models.[13,40,41] Under these conditions the coupling gain Γ of the two beams is defined by the equation[13]

$$\Gamma = \frac{\cos \theta_i}{l} \ln\left(\frac{I_S^p}{I_S^{np}}\right),$$ (21)

where I_S^p and I_S^{np} are the intensities of the signal beam with and without the pump beam, respectively; l is the crystal
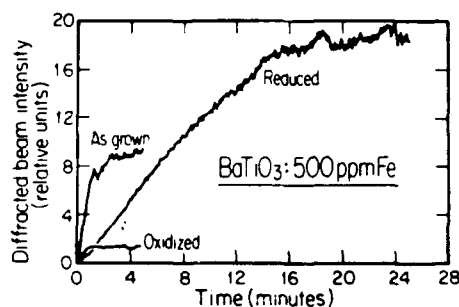

Fig. 12. Effects of oxidation and reduction on the diffracted-beam intensity versus time for $BaTiO_3$:500-ppm Fe. Similar results were achieved for 50- and 1000-ppm Fe-doped $BaTiO_3$.
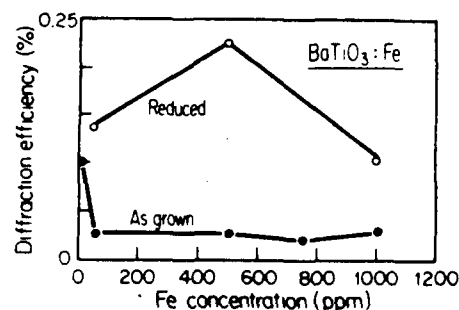

Fig. 13. Saturation diffraction efficiency of as-grown (filled circles) and reduced (open circles) $BaTiO_3$ as a function of Fe concentration.
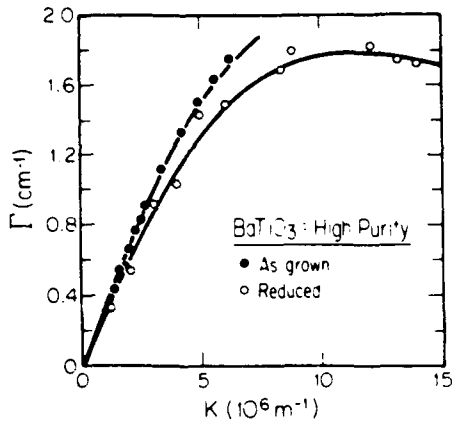
Fig. 14. Beam-coupling gain as a function of grating vector K of high-purity BaTiO. The filled circles represent the as-grown crystal, the open circles represent the reduced crystal, and the solid line is the theoretical fit.

thickness; and θ_i is the angle of the beams inside the crystal. The gain of Eq. (21) can be expressed by[13,40]

$$\Gamma = \frac{4\pi\delta n}{m\lambda \cos(\theta_i)} ,$$ (22)

where

$$\delta n = -\frac{n_o^3 E_{sc}}{2} r_{13}$$ (23)

and where n_o is the ordinary refractive index, r_{13} is the appropriate electro-optic coefficient, and E_{sc} is the steady-state space-charge field, which has the form[41]

$$E_{sc} = \frac{\zeta(K) \dfrac{mkT}{e}}{1 + (K/K_o)^2} ,$$ (24)

in which k is Boltzmann's constant, e is the electronic charge, and $\zeta(K)$ represents the amount of electron–hole competition. The term K_o^2 is related to the effective trap density N_T by the equation[13,40]

$$K_o^2 = \frac{e^2 N_T}{\epsilon\epsilon_o kT} ,$$ (25)

where ϵ is the relative dielectric constant and ϵ_o is the permittivity of free space.

The beam-coupling data are plotted as a function of grating vector K in Fig. 14. From the direction of beam coupling it was determined that the charge carriers were positive for both the as-grown and reduced crystals. Fitting these data to the above equations, we find that $\zeta(K)$ is fairly constant over the range of K values used ($\theta = 2$–$40°$). Using a value of 150 for ϵ_i, the dielectric constant associated with this crystal orientation,[39] we find that the effective trap density is $(2.9 \pm 0.4) \times 10^{-16}$ cm^{-3} and $(2.7 \pm 0.5) \times 10^{16}$ cm^{-1} for the as-grown and reduced crystal, respectively. Note that within the limits of error, reduction had no effect on the measured trap density of the high-purity crystals.

Light-induced grating erasure rate measurements were also used to confirm the effective trap densities in the pure samples. This technique was used previously to determine

materials properties of Bi$_{12}$SiO$_{20}$ (Ref. 42) and BaTiO$_3$ (Ref. 13) and involves writing a grating in the crystal by using two coherent plane waves, removing the writing beams, and flooding the crystal with a uniform erase beam. The decay of the grating diffraction efficiency is simultaneously monitored with a low-power readout beam. When the modulation index of the fringe pattern and the absorption coefficient are small, the decay rate $1/\tau$ is generally in the form of a single exponential and is related to the grating vector K through the equation[13,40]

$$\frac{1}{\tau} = 2\frac{(\sigma_{ph} + \sigma_D)}{\epsilon}\left[\frac{1 + (\epsilon kT/N_T e^2)K^2}{1 + (L_D K)^2}\right] .$$ (26)

where σ_{ph} is the photoconductivity; σ_D is the dark conductivity; N_T is the trap density as before; and the diffusion length L_D is given by $L_D^2 = \mu\tau_R kT/e$, where μ is the carrier mobility and τ_R is the recombination time.

The above experiments were performed for the case of anisotropic diffraction.[43] The writing beams were of wavelength 488 nm, with intensities $I_1 = 200$ mW/cm^2 and $I_2 = 0.1$ mW/cm^2. The erase-beam intensity, $I_E = 14$ mW/cm^2, was held constant throughout the experiment because decay rates in BaTiO$_3$ usually exhibit a nonlinear intensity dependence. The readout-beam intensity was kept less than 1 μW/cm^2. This readout beam ($\lambda = 633$ nm) was chopped at a frequency of 1000 Hz, and the diffracted beam was synchronously detected by using a photomultiplier tube and a lock-in amplifier. The output of the lock-in amplifier was fed to an AT&T 6300 computer equipped with a Data Translation acquisition board with the sampling rate set at 80 Hz. The grating decay data were least-squares fitted to a single exponential, and the decay rate, $1/\tau$, was calculated from the fit. The measurements were repeated as a function of grating vector by varying the writing-beam angles.

The decay rate as a function of the square of the grating vector for the range of K values used is shown in Fig. 15. When a value of 3600 is used for ϵ_a—the dielectric constant appropriate for this orientation[39]—the theoretical fit gives trap density values of $(3.1 \pm 0.3) \times 10^{16}$ cm^{-1} and $(3.3 \pm 0.4) \times 10^{16}$ cm^{-1} for the high-purity as-grown and reduced crystals, respectively. These values are in good agreement with those obtained from the beam-coupling results.
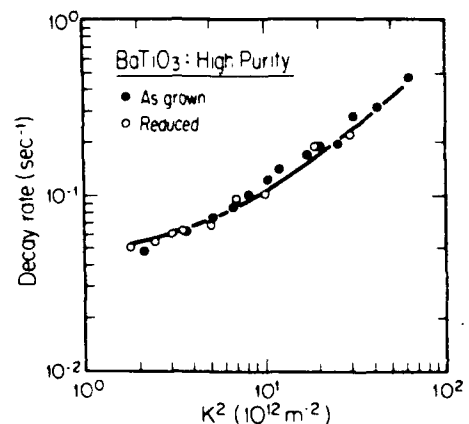

Fig. 15. Light-induced grating decay rate as a function of the grating vector squared for high-purity BaTiO in the as-grown (filled circles) and reduced (open circles) condition. Because the theoretical fits overlapped, only one curve is shown (solid curve).
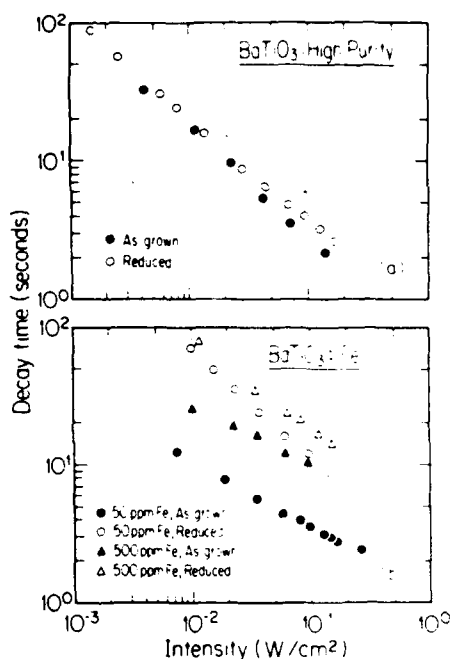
Fig 16. The grating diffraction efficiency decay time as a function of the erase-beam intensity for as-grown and reduced BaTiO₃ (a) high purity, (b) doped with 50 and 500 ppm of Fe.

The intensity dependence of the light-induced decay time was also measured for the above high-purity crystals as well as for the 50- and 500-ppm Fe-doped crystals in the as-grown and reduced condition. These measurements were conducted at a grating spacing of $\Lambda = 2.8\ \mu m$, and the results are shown in Figs. 16(a) and 16(b) for the high-purity and doped crystals, respectively. These data show that, like the measured trap density, both the intensity dependence and the absolute decay time remained the same in the as-grown and reduced high-purity crystals. Note also that the addition of large amounts of Fe decreases the speed of the crystals and that this speed is further reduced and the intensity dependence altered by reduction.

DISCUSSION AND CONCLUSIONS

On the basis of the theoretical defect model for BaTiO₃:Fe and the observed optical-absorption spectra, it is apparent that Fe^{3+} and Fe^{4+} are the dominant valence states of Fe present in our samples in the P_{O_2} range investigated. Thus it is clear that the popular model[5] in which Fe^{3+} and Fe^{2+} are the sources and traps of photorefractive charge carriers does not apply in this case and that trivalent and tetravalent Fe would be expected as the active photorefractive centers if Fe plays any role.

Despite the low levels of transition-metal impurities in our high-purity BaTiO₃ crystals, a relatively strong photorefractive effect was exhibited by these samples. In fact, the effective trap densities determined in the as-grown high-purity samples were of the order of $3 \times 10^{16}\ cm^{-3}$, which is comparable with those values reported for nominally undoped BaTiO₃ with 2 to 3 orders of magnitude higher impurity levels.[5] Furthermore, when high-purity BaTiO₃ samples were reduced, the effective trap density, carrier sign, and speed were virtually unchanged. Because the defect model predicts that this degree of reduction should yield a

nearly sevenfold increase in the concentration of Fe^{3+}, the observed photorefractive behavior of the high-purity crystals is inconsistent with a model in which Fe^{3+} acts as the trap site for photorefractive carriers. It appears, therefore, that Fe is not the dominant photorefractive species in these high-purity BaTiO₃ crystals. Instead, these results suggest that the photorefractive traps are associated with a defect whose concentration is independent of oxygen partial pressure in the P_{O_2} range $0.21-10^{-4}$ atm. Possibilities for such P_{O_2}-independent centers would include barium vacancies or oxygen vacancies (see Fig. 7), but these conjectures require further investigation.

Preliminary photorefractive characterization of Fe-doped BaTiO₃ indicated little change in the saturation diffraction efficiency of the as-grown crystals as a function of Fe content. Even the results for the reduced crystals, which displayed lower overall absorption and slightly higher efficiency, showed no systematic dependence on Fe concentration. The large range of Fe concentrations spanned by the data in Fig. 14, along with the associated variations in the Fe^{4+}/Fe^{3+} ratio given by Eq. (18), offered no visible improvement in properties.

Although the above results seem to suggest that Fe centers are not responsible for the photorefractive effect in the doped crystals, it is important to note that the behavior of these samples was different from that of the high-purity crystals. Figure 16 indicates that reduction affected both the speed and the intensity dependence of the grating erasure process and that these varied as a function of Fe content as well. In addition, the observed decreases and increases in saturation diffraction efficiency, which occurred on oxidation and reduction, respectively, are not inconsistent with a model involving Fe^{4+} and Fe^{3+} as the sources and traps of photorefractive charge carriers. The interpretation of these data is complicated, however, by a large P_{O_2}-dependent absorption coefficient in the Fe-doped crystals. For example, the observed decrease in saturation diffraction efficiency on reduction may simply be due to increased absorption of the writing beams by nonphotorefractive processes.

To complicate the issue further, we have recently observed evidence of strong intensity-dependent absorption in the Fe-doped crystals as opposed to the high-purity sample, which showed none. These observations have inhibited the interpretation of beam-coupling and grating decay measurements on the Fe-doped crystals, which will be presented elsewhere in the near future. In addition, work is continuing to expand the characterization of the crystals used in this study to cover a wider oxygen partial pressure range in order to clarify the role of iron centers in the photorefractive process in BaTiO₃ further.

ACKNOWLEDGMENTS

* Present address, Sanders Associates, 130 Daniel Webster Highway, Merrimack, New Hampshire 03054.

REFERENCES

1. G. C. Valley and M. B. Klein, Opt. Eng. **22**, 704 (1983).
2. P. Gunter, Phys. Rep. **93**, 199 (1982).
3. F. S. Chen, J. Appl. Phys. **40**, 3389 (1969).
4. Sanders Associates, Nashua, New Hampshire.
5. M. B. Klein and R. N. Schwartz, J. Opt. Soc. Am. B **3**, 293 (1986).
6. G. E. Peterson, A. M. Glass, and T. J. Negran, Appl. Phys. Lett. **19**, 130 (1971).
7. G. E. Peterson, A. M. Glass, A. Carnevale, and P. M. Bridgenbaugh, J Am. Ceram. Soc. **56**, 278 (1973).
8. M. G. Clark, F. J. DiSalvo, A. M. Glass, and G. E. Peterson, J. Chem. Phys. **54**, 6209 (1973).
9. H. Kurz, E. Kratzig, W. Keune, H. Engelmann, U. Gonser, B. Dischler, and A. Rauber, Appl. Phys. **12**, 355 (1977).
10. B. A. Wechsler, M. B. Klein, and D. A. Rytz, Proc. Soc. Photo-Opt. Instrum. Eng. **681**, 91 (1986).
11. S. Ducharme and J. Feinberg, J. Opt. Soc. Am. B **3**, 283 (1986).
12. S. Godefroy, G. Ormancey, P. Jullien, Y. Semanou, and W. Ousi-Benomar, in *Digest of IEEE International Symposium on Applications of Ferroelectrics (ISAF)* (Institute of Electrical and Electronics Engineers, New York, 1986), paper PA-1.
13. J. Feinberg, D. Heiman, A. R. Tanguay, Jr., and R. W. Hellwarth, J. Appl. Phys. **51**, 1297 (1980).
14. P. G. Schunemann, D. A. Temple, R. S. Hathcock, H. L. Tuller, H. P. Jenssen, D. R. Gabbe, and C. Warde, in *Digest of Conference on Lasers and Electro-Optics* (Optical Society of America, Washington, D.C., 1987), p. 178.
15. P. G. Schunemann, D. A. Temple, R. S. Hathcock, C. Warde, H. L. Tuller, and H. P. Jenssen, in *Digest of Topical Meeting on Photorefractive Materials, Effects, and Devices* (Optical Society of America, Washington, D.C., 1987), p. 23.
16. C. Warde, D. Temple, P. Schunemann, R. S. Hathcock, H. L. Tuller, and H. P. Jenssen, Proc. Soc. Photo-Opt. Instrum. Eng. **825**, 101 (1987).
17. D. C. Bradley, R. C. Mehotra, and D. P. Gaur, *Metal Alkoxides* (Academic, London, 1978), Chap. 3.
18. K. B. Wiberg, *Laboratory Techniques in Organic Chemistry* (McGraw-Hill, New York, 1960), pp. 1–74.
19. A. Linz, V. Belruss, and C. S. Naiman, J. Electrochem. Soc. **112**, 60C (1965).
20. V. Belruss, J. Kalnajs, and A. Linz, Mater. Res. Bull **6**, 899 (1971).
21. A Glasner and P. Avinur, Talanta **11**, 679, 761, 775 (1964)
22. G. Godefroy, C. Dumas, P. Lompre, and A. Perrot, Ferroelectrics **37**, 725 (1981).
23. M. S. Kosman and E. V. Bursian, Sov. Phys. Dokl. **2**, 354 (1957).
24. G. Ormancey and P. Jullien, Ferroelectrics Lett. **1**, 103 (1983).
25. J. Blanc and D. L. Staebler, Phys. Rev. B **4**, 3548 (1971).
26. H.-J. Hagemann and H. Ihrig, Phys. Rev. B **20**, 20 (1979).
27. S. A. Long and R. N. Blumenthal, J. Am. Ceram. Soc. **54**, 515 (1971).
28. S. A. Long and R. N. Blumenthal, J. Am. Ceram. Soc. **54**, 577 (1971).
29. N. G. Eror and D. M. Smyth, J. Solid State Chem. **24**, 235 (1978).
30. N.-H. Chan, R. K. Sharma, and D. M. Smyth, J. Am. Ceram. Soc. **64**, 556 (1981).
31. N.-H. Chan and D. M. Smyth, J. Electrochem. Soc. **123**, 1584 (1976).
32. A. M. J. H. Seuter, Philips Res. Rep. Suppl. **3**, 1 (1974).
33. H.-J. Hagemann, A. Hero, and U. Gonser, Phys. Status Solidi A **61**, 63 (1980).
34. H.-J. Hagemann and D. Hennings, J. Am. Ceram. Soc. **64**, 590 (1981).
35. H.-J. Hagemann, "Akzeptorionen in BaTiO₃ und SrTiO und ihre Auswirkung auf die Eigenschaften von Titanat Keramiken," Ph.D. dissertation (Rheinisch-Westfalische Technische Hochschule, Aachen, Federal Republic of Germany, 1980).
36. F. A. Kroger and H. J. Vink, in *Solid State Physics*, F. Seitz and D. Turnbull, eds. (Academic, New York, 1956), Vol. 3, p. 307.
37. J. I. Pankove, *Optical Processes in Semiconductors* (Dover, New York, 1971).
38. S. H. Wemple, M. Didomenico, Jr., and I. Camlibel, J. Phys. Chem. Solids **29**, 1797 (1968).
39. R. Wernicke, Philips Res. Rep. **31**, 526 (1976).
40. N. V. Kukhtarev, Sov. Tech. Phys. Lett. **2**, 438 (1976).
41. F. P. Strohkendl, J. M. C. Jonathan, and R. W. Hellwarth, Opt. Lett. **11**, 312 (1986).
42. R. A. Mullen and R. W. Hellwarth, J. Appl. Phys. **58**, 40 (1985).
43. D. A. Temple and C. Warde, J. Opt. Soc. Am. B, **3**, 337 (1986).

P. G. Schunemann

P. G. Schunemann was born at Peabody, Massachusetts, on March 20, 1962. He received the B.S. degree in materials science and engineering in 1984 and the M.S. degree in ceramics in 1987, both from the Massachusetts Institute of Technology (MIT). His research at MIT focused on the crystal growth of high-purity and iron-doped BaTiO and the characterization of its electronic, optical, and photorefractive properties. Since April of 1987, he has been employed by Sanders Associaties in Merrimack, New Hampshire, where he has continued his research on BaTiO and other nonlinear-optical materials. His fields of interest include high-purity synthesis, defect chemistry, and single-crystal growth of inorganic materials.

H. L. Tuller

H. L. Tuller is professor of ceramics and electronic materials and the director of the crystal physics and optical electronics laboratory in the Department of Materials Science and Engineering at MIT. He received B.S. and M.S. degrees in electrical engineering and a Ph.D. in solid state science and engineering from Columbia University, New York, in 1966, 1967, and 1973, respectively. He served as a research associate in the Department of Physics at the Technion in Israel until 1975, when he joined the MIT faculty. His research interests include charge and mass transport, optical properties of ceramics and glasses, defect theory, and materials development for sensors.

4 Photoinduced Optical Absorption in BaTiO$_3$: Fe

Photoinduced Optical Absorption in BaTiO$_3$:Fe

Doyle A. Temple[a] and Cardinal Warde

Departments of Physics and Electrical Engineering and Computer Sciences

Massachusetts Institute of Technology

Cambridge, Massachusetts 02139

Measurements of the steady state photoinduced absorption $\Delta\alpha$ have been performed on single crystalline samples of pure and iron doped BaTiO$_3$. The results show that $\Delta\alpha$ has a sublinear intensity dependence, similar to that observed in photorefractive grating decay measurements.

[a]Present address, Department of Physics and Astronomy, Louisiana State University.

Baton Rouge, LA 70803

▼

Determination of the origin of the centers responsible for the photorefractive effect in $BaTiO_3$ is complicated by the presence of several competing effects including stimulated photorefractive scattering (commonly known as beam fanning), [1,2] anisotropic scattering, [3,4,5] and photoinduced absorption. [6-10] To better aid in modelling of these charge transport processes, experimental methods must be employed that effectively de-couple these competing effects.

The first measurements of the photoinduced absorption in $BaTiO_3$ were performed by Motes et al [6-8] and Brost et al. [9] More recently, Pierce et al [10] showed that absorption gratings could be produced in $BaTiO_3$ using a configuration that does not allow photorefractive beam coupling. Using this method, these autors were able to determined the trap density associated with the absorption gratings.

Iron has long been suspected as being the active photorefractive centers in $BaTiO_3$. Klein and Schwartz [11] found a good correlation between the iron concentration and the photorefractive trap density in various commercial samples. Although these samples had several impurities that could be photorefractive centers, the strongest correlation was with the iron concentration. Godefroy et al [12] measured the diffraction efficiency in unpoled, iron-doped samples and found a peak near 750 ppm. Previously, the diffraction efficiency and photorefractive speed of iron doped $BaTiO_3$ samples were reported by Schunemann et al. [13] More recently, we reported measurements of the photorefractive trap density in the iron doped samples using the light induced grating erasure technique. [14] In this paper, we describe a method of measuring photoinduced absorption effects using a configuration which is free from photorefractive beam coupling, allowing accurate quantification of the photoinduced absorption, $\Delta\alpha$.

The crystals used in our experiments were grown from a melt containing high-purity $BaCO_3$ and TiO_2 and extreme care was taken to minimize melt contamination by the furnace. Spark mass spectrographic analysis of the pure crystals showed less than 0.3 ppm iron (see Table for a list of the other impurities present). After growth of two high purity boules, several iron doped boules were grown from the same melt using the composition 0.34 % $BaCO_3$ and 0.66 % $[(1-x)TiO_2 + (x/2)Fe_2O_3]$ where x is the concentration in ppm. In these experiments 50 ppm, 500 ppm and 1000 ppm concentrations were used. Chemical analysis of these boules indicates a segregation coefficient near unity (see Table). At least two samples

from each of these boules were cut along (100) planes and then mechanically and electrically poled. One sample was used as grown and the other annealed at 800 °C in a reducing oxygen partial pressure of 10^{-4} atmospheres. For a more complete description of the growth and preparation of these samples the reader is referred to Ref. 13.

Two problems associated with photoinduced absorption measurements are wave-mixing effects and nonuniform illumination along the path of the probe beam. Nonuniform photoinduced absorption along the path of the probe beam results when both the pump and probe beams pass through the center of the sample. This causes the intensity of the pump beam to change along the path of the probe beam. Calculation of $\Delta\alpha$ would require a detailed knowledge of the analytical equations describing the photoinduced absorption, which is the unknown being determined. Nonuniform illumination effects can be minimized by two simple changes. First, a small diameter probe beam, approximately 1 mm, is directed parallel to, and just below the crystal surface to be illuminated. Second, expanding the diameter of the pump beam so that it is much larger than the crystal to approximate uniform illumination.

The experimental setup shown in Fig. 1 minimizes these problems in several ways. Wave mixing effects are eliminated by: (1) using two separate lasers for the pump and probe beams and (2) intersecting the beams in the x-y plane of the crystal, which by symmetry forbids beam coupling of the writing beams in $BaTiO_3$.[5] Using this setup, $\Delta\alpha$ is approximately constant along the path of the probe beam. Finally, the intensity of the probe beam is kept below $1\mu W/cm^2$ to minimize photoinduced absorption effects due to the probe beam. Under these conditions the photo-induced change in the absorption, measured by the probe beam, is given by [7]

$$\Delta\alpha = \frac{1}{L}\ln\frac{I_t^{(without\ pump)}}{I_t^{(with\ pump)}}. \tag{1}$$

where L is the thickness of the crystal parallel to the probe beam. $I_t^{(without\ pump)}$ is the transmitted probe beam intensity without the pump beam present. and $I_t^{(with\ pump)}$ is the intensity of the probe beam with the pump beam present. For these experiments, the pump source was a 3-watt argon ion laser operating at 488 nm. The pump beam was expanded and collimated using two lenses and passed through a 1/2 wave plate and a polarizer before entering the crystal. The half wave plate allowed the intensity of the pump beam to be easily varied by simply rotating plate.

A second 100 mW air cooled argon ion laser operating at 488 nm was used for the probe beam. This beam was expanded and collimated to a diameter of approximately 5 cm and directed through a polarizer positioned in a rotator, followed by another polarizer aligned along the crystal axis, and finally through a 1 mm diameter aperture. The intensity of the probe beam was modulated at a frequency of 1000 Hz using an optical beam chopper, and synchronously detected using a photomultiplier tube and a lock-in amplifier. In all of these measurements the pump and probe beam polarizations were the same, that is, both parallel to the a axis (ordinary polarization) or c axis (extraordinary polarization). The change in the absorption was measured at various pump beam intensities for both ordinary and extraordinary polarization.

The results of these measurements are shown in Figs.2 and 3. The change in the absorption for the pure as-grown crystal is not shown since there was none detected at the intensities used in this work. The rise time of the induced absorption was faster than the resolution of our detection system, which was a few milliseconds, while the dark decay time was on the order of 10-20 minutes. Because of this, the measurements started at the low pump intensities and proceeded to the high intensities. After a run, the crystal was allowed to return to the dark equilibrium conditions. As shown in the figures, the photoinduced absorption $\Delta\alpha$ increases nonlinearly with intensity for all the samples. However, since the experiment was designed to minimize intensity variations across the crystal surface, very high intensities were not achievable and we were unable to observe saturation.

As shown in table 3, both the absorption and the change in the absorption were found to increase with iron content for a given polarization, pump beam intensity, and oxidation state. Also, for any particular dopant level, the absorption and the photoinduced absorption of the as grown sample was always larger than that of the reduced sample. The sublinear intensity behavior of the photoinduced absorption resembles that of the sublinear photoconductivity measured by Ducharme and Feinberg. [15] The erasure rate of our as-grown samples was previously reported to increase sublinearly with intensity [14] and therefore seem to correspond to the type B crystals discussed by Mahgereftreh. [16] Since the intensity dependence of the photoinduced absorption and the photoconductivity are similar, it is likely that shallow levels, as described in the models of Mahgereftreh [16] and Brost, [17] play a role in the photoinduced absorption. If the shallow acceptor levels were the source of the photoinduced absorption,

then annealing a type B crystal in reducing atmospheres, should result in partial filling of the shallow acceptor levels and thus a decrease in the photoinduced absorption. As shown in the figures and table 3, the crystals that were annealed in reduced oxygen partial pressures did show a decrease in the photoinduced absorption.

In conclusion, we have performed photoinduced absorption measurements on pure and Fe doped samples of $BaTiO_3$. Our results show that: (1) there is a photoinduced absorption effect that increases with the addition of iron, (2) the photoinduced absorption increases sublinearly with intensity, and (3) annealing the crystals in reduced oxygen partial pressures lowers the photoinduced absorption. At present it is not clear if the charge centers responsible for the photoinduced absorption are due to iron, or if the charge compensating defects, such as oxygen vacancies or Fe-oxygen vacancy complexes are the cause. Further experiments, such as correlation of the EPR spectra with the photorefractive trap density and photoinduced absorption, would be needed to clarify the exact nature of the photorefractive centers.

References

1. Jack Feinberg, J. Opt. Soc. Am. **72**, 46 (1982)

2. G. Valley, J. Opt. Soc. Am. **B4**, 14 (1987)

3. N. V. Kuktarev, E. Kratzig, H. C. Kulich, and R. A. Rupp, Appl. Phys. B **35**, 17 (1984)

4. M. Ewbank, P. Yeh, and J. Feinberg, Opt. Commun., **59**, 423 (1986)

5. D. A. Temple and C. Warde, J. Opt. Soc. Am. B **3**,337 (1986)

6. Andy Motes and Jin Joong Kim, Opt. Lett. **12**, 199 (1987)

7. Andy Motes and Jin Joong Kim, J. Opt. Soc. Am. **B4**, 1379 (1987)

8. A. Motes, G. Brost, J. Rotge, and J. Kim, Opt. Lett. **13**, 509 (1988)

9. G. A. Brost, R. A. Motes, and J. R. Rotge, J. Opt. Soc. Am. **B5**, 1879 (1988)

10. R.M. Pierce, R.S. Cudney, G.D. Bacher and Jack Feinberg, Opt. Lett. **15**, 414 (1990)

11. M. B. Klein and R. N. Schwartz, J. Opt. Soc. Am. B **3**, 293 (1986)

12. G. Godefroy, G. Ormancey, P. Jullien, W. Ousi-Benomar, and Y. Semanou, Digest of IEEE International Symposium on Applications of Ferroelectrics (ISAF) (IEEE, New York, 1986, paper PA-1).

13. P. G. Schunemann, D. A. Temple, R. S. Hathcock, C. Warde, H.L. Tuller, and H. P. Jenssen, J. Opt. Soc. B5, 1685 (1988)

14. D. A. Temple, R. S. Hathcock, and C. Warde, J. Appl. Phys. **67**, 6667 (1990)

15. S. Ducharme and J. Feinberg , J. Appl. Phys. **56**, 839 (1984)

16. Daniel Mahgerefteh and Jack Feinberg, Phys. Rev. Lett. **64**, 2195 (1990)

17. G.A. Brost and R. A. Motes, Optics Lett. **15**, 1194 (1990)

Tables

Table I: Spark-Source Mass Spectrographic Analysis of Undoped
$BaTiO_3$. After Ref.(13)

Element	Level (ppm) present in $BaTiO_3$
B^{3+}	5
Na^+	≤ 2
Mg^{2+}	2
Al^{3+}	0.5
$Si4+$	4
P^{5+}	0.05
S^{2-}	< 2
Cl^-	10
K^+	≤ 0.1
Ca^{2+}	2
$Cr^{3,2+}$	≤ 0.02
$Mn^{2,3,4+}$	≤ 0.02
$Fe^{2,3,4+}$	0.3
$Ni^{2,3+}$	0.04
$Cu^{1,2+}$	
As^{5+}	0.1
Sr^{2+}	50

Table II: Chemical analysis of the $BaTiO_3$ samples. After Ref.(13)

[a] Atomic absorption (Northern Analytical).

[b] Spark-source mass spectrometry (Northern Analytical).

Iron Doping Level added to the Melt (ppm)	Iron Level in $BaTiO_3$ Crystals Analysed (ppm)[a]
0	0.3[b]
50	49
500	530
1000	980

Table III:The absorption coefficient at 488 nm was measured using a Perkin-Elmer Lambda 9 double beam spectrometer. The photoinduced absorption data is given at a laser intensity of 0.5 W/cm². All of the data is for ordinary polarization.

Fe Concentration	Absorption (cm^{-1})		$\Delta\alpha$ (cm^{-1})	
	As Grown	Reduced	As Grown	Reduced
Pure	0.53	0.47	-	0.11
50 ppm Fe	0.76	0.66	0.7	0.31
500 ppm Fe	1.73	0.63	1.1	0.9
1000 ppm Fe	-	1.23	1.05	1.05
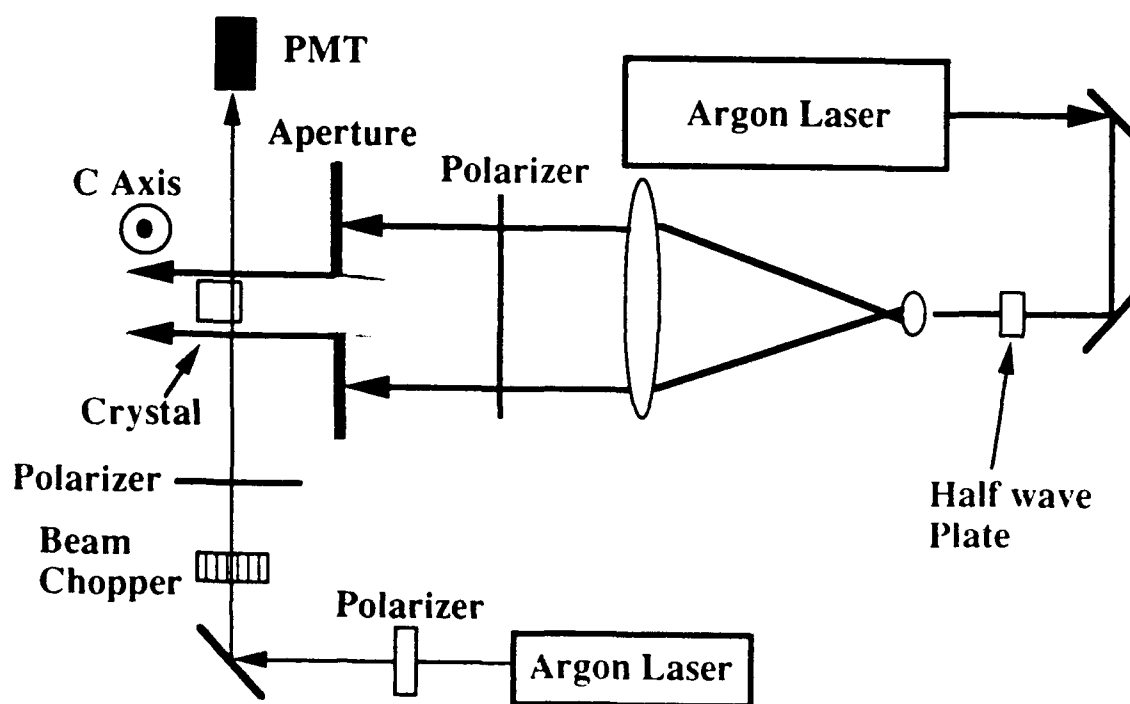
1. Setup used to study photo-induced absorption.
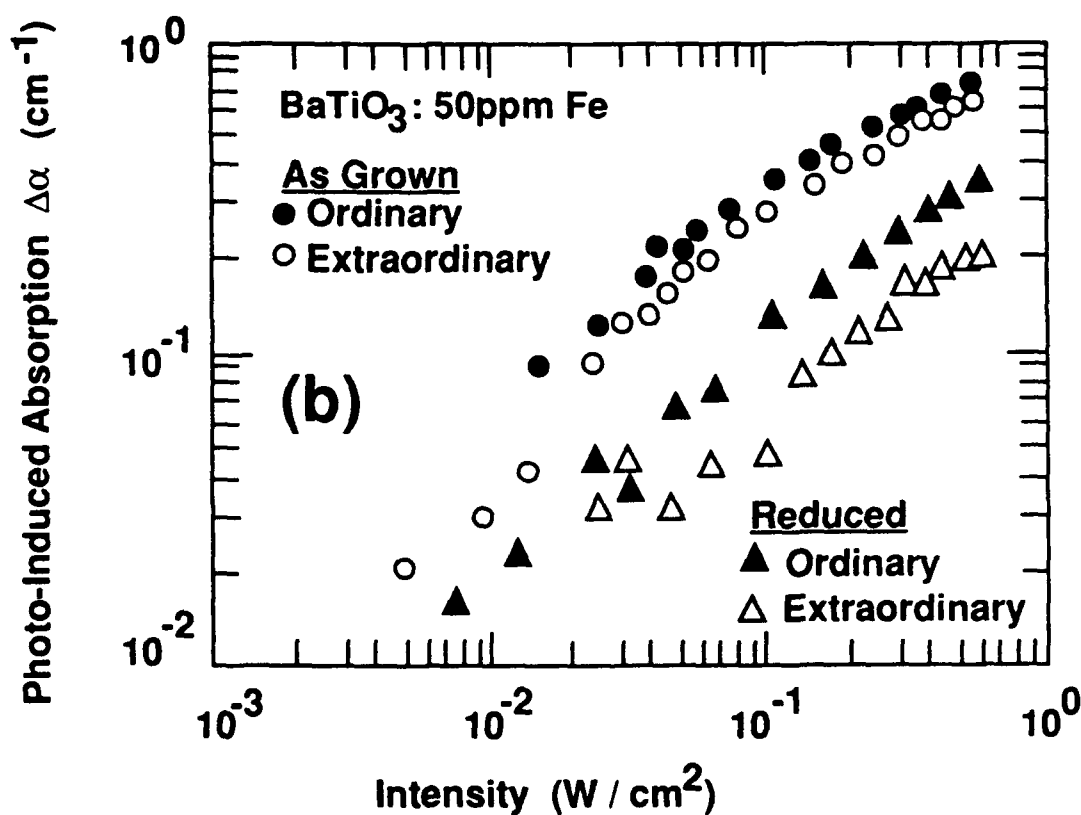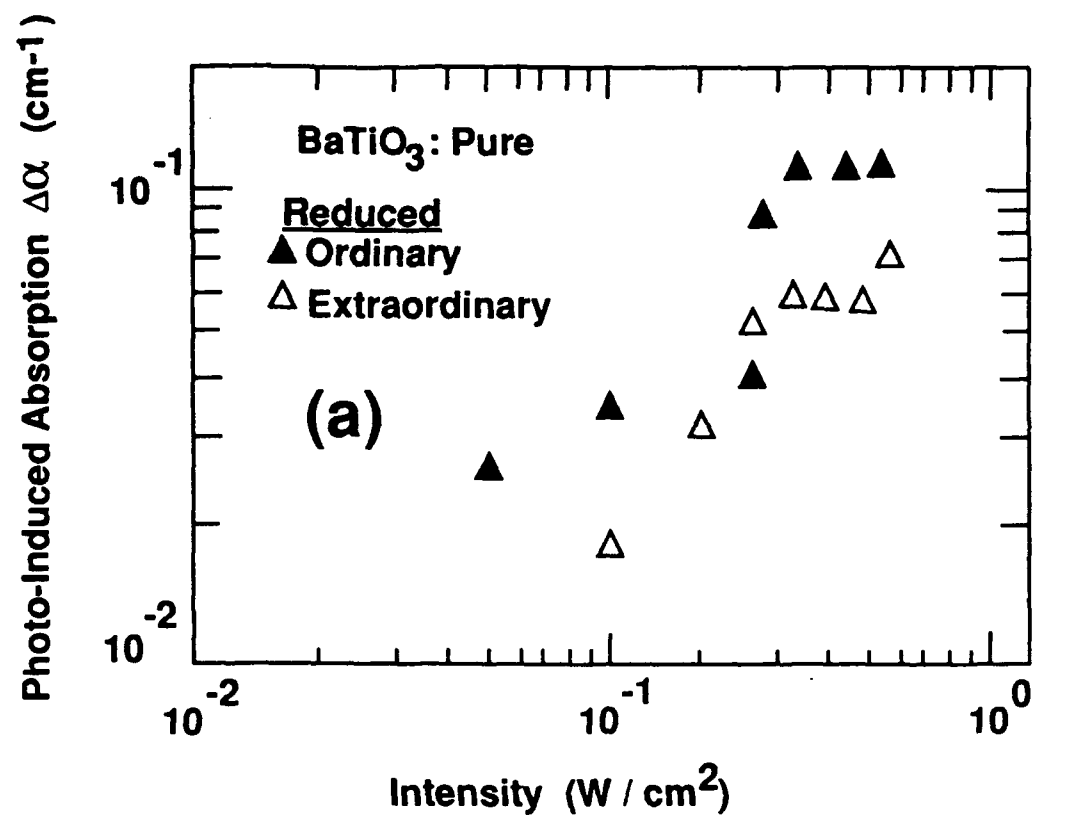
2. The photo-induced absorption in BaTiO$_3$ plotted as a function of the pump beam intensity for (a) pure and (b) 50 ppm Fe.
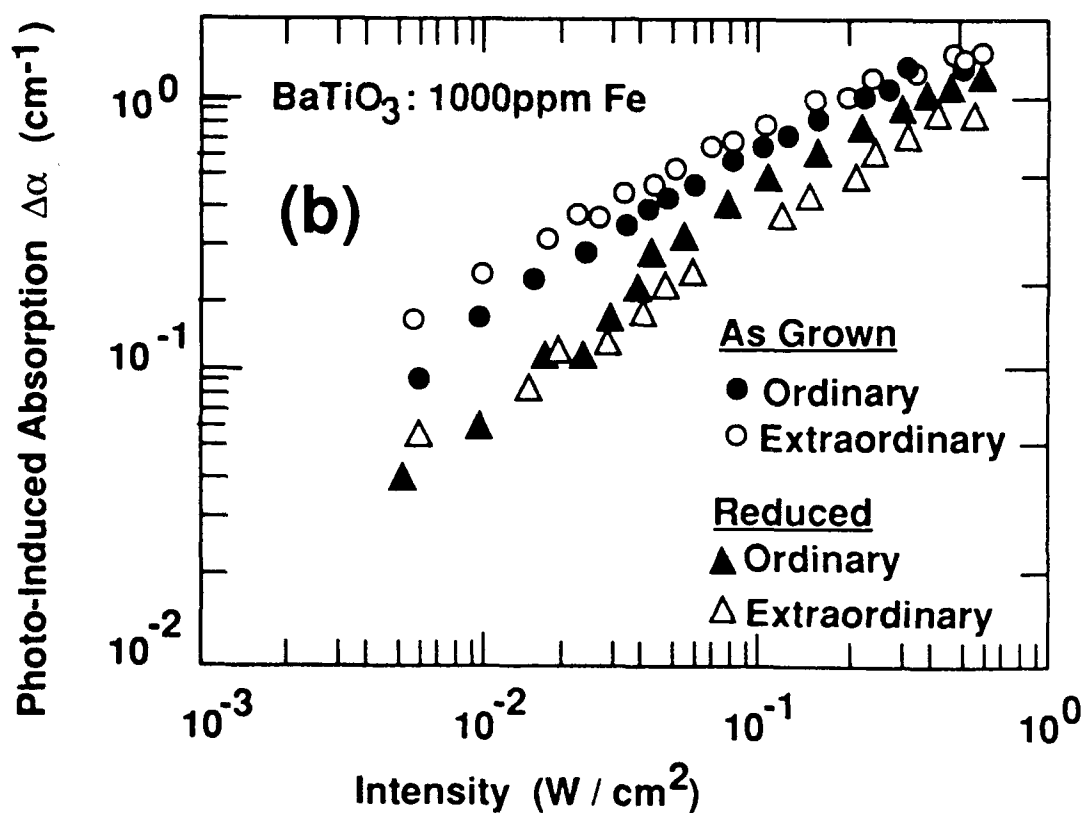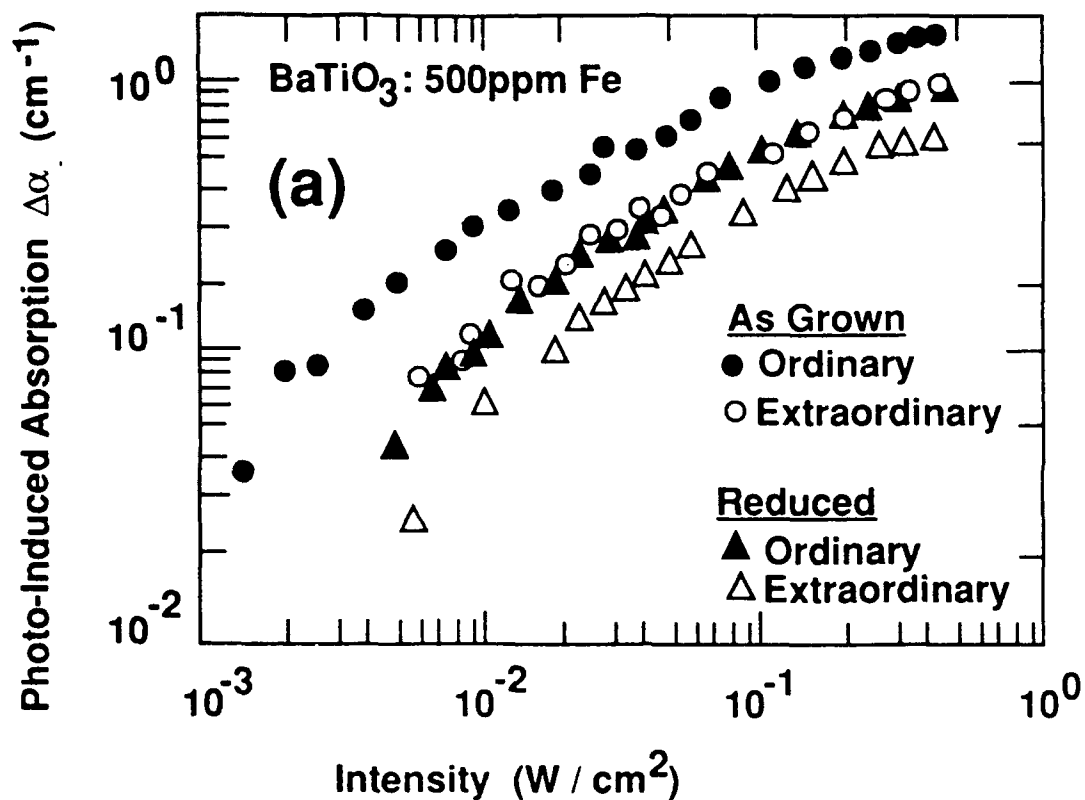
3. The photo-induced absorption in $BaTiO_3$ plotted as a function of the pump beam intensity for (a) 500 ppm Fe and (b) 1000 ppm Fe.

5 Intensity Dependent Photorefractive Properties of BaTiO$_3$

Intensity dependent photorefractive properties of BaTiO₃

Doyle A. Temple,[a] R. Scott Hathcock, and Cardinal Warde

Department of Physics and Center for Materials Science and Engineering, Massachusetts Institute of Technology, Cambridge, Massachusetts 02139

We have used the light-induced grating erasure technique to measure the photorefractive properties of pure and iron doped BaTiO₃. Our experiments were performed using an anisotropic configuration which forbids beam coupling and self-diffraction between the writing beams, resulting in plane parallel intensity fringes that do not change with time. This allowed direct measurement of the charge transport processes without any feedback on the grating due to wave-mixing processes. The results from these experiments show that the photorefractive parameters known as the trap density N_{pr} and the mobility-recombination time product $\mu\tau_r$ vary with intensity and are not material constants.

I. INTRODUCTION

The photorefractive properties of BaTiO₃ and other photorefractive materials, have been studied by a number of researchers using a variety of optical techniques.[1-6] Many of the experimental results are found to be described by the hopping model[1] or the band transport model.[7] One method for optical characterization of photorefractive materials is the light-induced grating erasure technique.[5] Using this technique, Feinberg found that the grating spacing dependence of the photorefractive gratings in BaTiO₃ was well described by the models,[1,7] and could be used to determine the photorefractive trap density N_{pr}. Mullin and Hellwarth performed similar experiments in Bi₁₂SiO₂₀ (BSO) and showed that the technique could also be used to determine the mobility recombination time product $\mu\tau_r$.[5] However, Ducharme and Feinberg found that the photoconductivity of BaTiO₃, determined from the light-induced grating decay rates of photorefractive gratings, varies nonlinearly with intensity.[8] More recently, Brost et al.[9] found that their beam coupling data showed that the photorefractive trap density in BaTiO₃ varied with intensity.

In this paper we report the results of light-induced grating erasure measurements on pure and Fe doped BaTiO₃ using anisotropic gratings that do not allow beam coupling or self-diffraction between the writing beams. The results show the photorefractive parameters known as the trap density N_{pr} and the mobility recombination time product $\mu\tau_r$ are functions of intensity.

II. THEORY

A. Photorefractive response time

Consider the band transport model of Kukhtarev[7] in which there are donor and acceptor levels in the band gap of the crystal. For this example, we have chosen (1) the acceptor density to be larger than the donor density, $N_A > N_D$, and (2) the transport is dominated by hole conduction.[8] If all the electrons from the donors are transferred to the acceptors, the density of unfilled acceptors is $N_A - N_D$. These unfilled acceptors are assumed to be available to be redistributed by the light among all the acceptor levels. If the applied intensity pattern is in the form of a sinusoidal fringe pattern

$$I(x) = I_0[1 + m\cos(Kx)], \tag{1}$$

where $m \ll 1$, and K is the spatial frequency of the fringes, the resulting charge distribution may also be sinusoidal. For this case, the charge transport solutions of Kukhtarev[7] and Feinberg[1] both predict an exponential response for the photorefractive gratings given by

$$\frac{1}{\tau} = \frac{\sigma_{ph}}{\epsilon}\left(\frac{1 + (\epsilon kT/e^2 N_{pr})K^2}{1 + (\tau_r\mu k_b T/e)K^2}\right), \tag{2}$$

where

$$\sigma_{ph} = \frac{e\mu[(s/h\nu)I_0 + \beta_r](N_A - N_D)}{\gamma_r N_D}, \tag{3}$$

is the photoconductivity, μ is the mobility, γ_r is the recombination constant, ν is the light frequency, s is the photoionization cross section, h is Planck's constant, β_r is the thermal generation constant, ϵ is the static dielectric constant, k_b is the Boltzmann constant, T is the lattice temperature,

$$\tau_r = 1/(\gamma_r N_D), \tag{4}$$

is the recombination time and

$$N_{pr} = N_D \tag{5}$$

is the photorefractive trap density. The only intensity dependence in Eq. (2) is the photoconductivity, given by Eq. (3), which is predicted to be linear in intensity. Also, Eqs. (4) and (5) give the mobility recombination time product and the photorefractive trap density as material constants.

B. Anisotropic diffraction

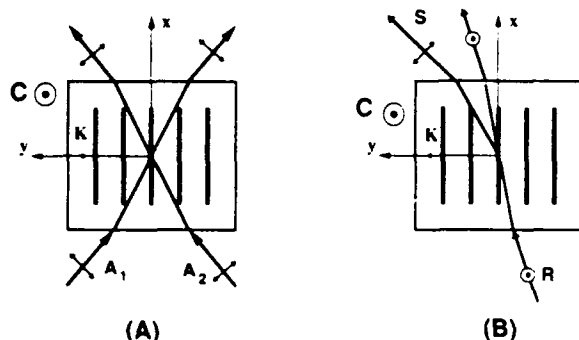For the experiments reported here anisotropic gratings were used. That is the grating vector lies in the x-y plane of

46

FIG. 1. Beam geometry illustrating (a) writing and (b) readout of an anisotropic photorefractive grating in the x-y plane. In (a) the writing beams A_1 and A_2 intersect in the crystal producing a photorefractive grating with a wave vector $\mathbf{K} = \mathbf{k}_2 - \mathbf{k}_1$. In (b) an extraordinary polarized readout beam R scatters into an ordinary polarized beam S, where $\mathbf{K} = \mathbf{k}_S - \mathbf{k}_R$.

FIG. 2. Optical system used for light-induced grating erasure as a function of grating vector $\mathbf{K}$.

the crystal.[10,11] One of the advantages of anisotropic diffraction is that there are certain configurations in which gratings can be produced with no beam coupling or self-diffraction allowed between the writing beams.[12] For two waves intersecting in a photorefractive crystal the amount of coupling or self-diffraction between the writing beams is proportional to the effective susceptibility.[13]

$$\chi_{\text{eff}} = (\,\hat{e}_1^* \cdot \hat{e}_2\,)[\,\hat{e}_1^* \cdot (\,-\,\bar{\bar{\epsilon}}_0 \cdot \mathbf{E} \cdot \tilde{R} \cdot \epsilon_0\,) \cdot \hat{e}_2\,], \qquad (6)$$

where $\hat{e}_1$ and $\hat{e}_2$ are the polarization vectors of the writing beams, $\hat{e}_R$ and $\hat{e}_S$ are the polarization vectors of the readout and scattered beams respectively, $\bar{\bar{\epsilon}}_0$ is the second rank optical dielectric tensor, $\tilde{R}$ is the third rank electro-optic tensor, and $\mathbf{E}$ is the space charge field. If the two waves interfere in the x-y plane of 4 mm symmetry BaTiO$_3$ as shown in Fig. 1(a), the effective susceptibility is zero when the polarizations of the writing beams are both ordinary or both extraordinary.[12] In this case, the feedback between the charge transport processes and the wave diffraction processes is eliminated, resulting in intensity fringes that are parallel planes and that do not change with time. Thus for very small modulation, $m \ll 1$, the solutions derived by Kukhtarev[7] and Feinberg.[1] are very close to the actual experimental conditions. Since the feedback from the wave-mixing processes on the charge transport processes of grating formation has been eliminated, each can be studied independently. This is therefore an excellent configuration for the measurement of photorefractive parameters.

Equation (6) does allow anisotropic diffraction to occur for readout of this grating. In this instance, the effective susceptibility is

$$\chi_{\text{eff}} = (\,\hat{e}_1^* \cdot \hat{e}_2\,)[\,\hat{e}_R^* \cdot (\,-\,\bar{\bar{\epsilon}}_0 \cdot \mathbf{E} \cdot \tilde{R} \cdot \bar{\epsilon}_0\,) \cdot \hat{e}_S\,]. \qquad (7)$$

where $\hat{e}_R$ and $\hat{e}_S$ are the polarization vectors of the readout and scattered beams. For a negative uniaxial crystal the phase matching angles for anisotropic diffraction as shown in Fig. 1(b) are given by[12]
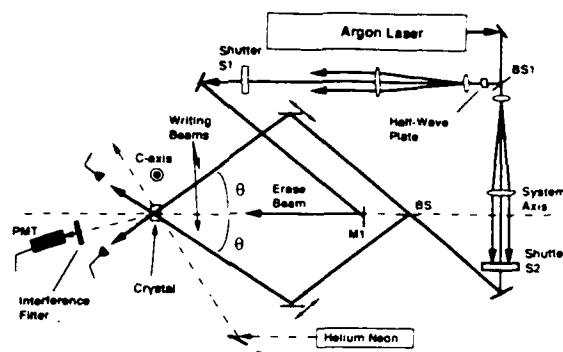
$$\sin(\alpha_R) = \left[\frac{n_0^2 - n_e^2}{4\sin(\theta)} \left(\frac{\lambda_W}{\lambda_R} \right) - \frac{\lambda_R}{\lambda_W} \sin(\theta) \right], \qquad (8)$$

and

$$\sin(\alpha_S) = [n_0^2 - n_e^2 + \sin^2(\alpha_R)]1/2, \qquad (9)$$

where α_R and α_S are the angles outside the crystal of the extraordinary polarized readout beam and ordinary polarized scattered beam measured from the surface normal, n_0 and n_e are the indices of refraction at the readout beam wavelength, θ is the angle of the writing beams with the surface normal, and λ_W and λ_R are the writing and readout beam wavelengths.

III. EXPERIMENTAL METHODS

A. Light-induced grating erasure

The light-induced grating erasure technique involves writing a photorefractive grating in the crystal with two coherent plane waves, then removing the writing beams and flooding the crystal uniformly with an erase beam.[1,4] The grating decay rate is simultaneously monitored with a low power ($1\ \mu\text{W/cm}^2$) readout beam incident at the Bragg angle.

The optical setup used for the light-induced decay rate experiment is shown in Fig. 2. In this setup an argon ion laser was used for the writing beams and the erase beam. As shown in Fig. 2, a beam splitter labeled BS1, was placed just after the laser to produce two separate beams that were expanded and collimated using spatial filters. The beam reflected by BS1, was used as the erase beam. This beam was directed onto mirror M1 then through the center of the crystal mount with the line between M1 and the crystal mount defining the system axis. The intensity of the erase beam was varied using a rotating half wave plate followed by a polarizer. The beam transmitted through the beam splitter BS1 was directed through the second beam splitter BS to produce two writing beams. These beams were directed symmetrically about the system axis. Optical table rails were mounted parallel to the two writing beam paths with mirrors mounted on each rail to redirect the beams onto the crystal. The rails were calibrated to allow accurate angular measurements. The intensity of one of the writing

beams was varied using rotating polarizer followed by a fixed polarizer. This was necessary to ensure that the modulation index was small $m < 1$.

For $BaTiO_3$, phase matching for anisotropic diffraction is limited to an angular range of $3° < \alpha < 20°$ for 488 nm writing beams and 633 nm readout beams, where α is the incident angle of the readout beam outside of the crystal. We note here that extreme care must be taken so as not to confuse higher diffracted orders which are easily observed in the anisotropic configuration in $BaTiO_3$.[14] Also, we found that small shifts in the position of the erase beam in the crystal caused significant variations in the decay rates. Therefore, the crystal and the erase beam were not moved during the experiments.

A HeNe laser was used to readout the gratings (see Fig. 2). This beam was expanded using two lenses and the intensity was varied using a rotating polarizer followed by a fixed polarizer. The beam was directed along the optical rail by two mirrors and modulated by a beam chopper at a frequency of 1000 Hz. The readout beam angle could be varied by moving a mirror along the rail and redirecting the beam to the crystal. The diffracted beam was synchronously detected using a photomultiplier tube and a lock-in amplifier with the output of the lock-in captured by an AT&T 6300 computer equipped with a Data Translation data acqustion board. The sampling rate was set at 80 Hz and the grating decay rates were found to be well fitted by a single exponential. Also, a 633 nm interference filter was placed in front of the photomultiplier tube to eliminate bleaching from the argon laser.

A typical measurement was made as follows: First shutter S1 was opened and any gratings present in the crystal were erased. Shutter S1 was closed and shutter S2 opened allowing the writing beams to intersect in the crystal forming a photorefractive grating. This grating was monitored by measuring the diffraction of a HeNe beam incident upon the crystal at the Bragg angle. Eq. (8). When the diffraction efficiency reached saturation, shutter S2 was closed and simultaneously S1 opened, erasing the grating. After three or four decay times were measured, the angles of the writing beams were changed and the measurement repeated. After one complete scan of the angular range was finished, the erase beam intensity was increased and the measurement repeated. The writing beams, and the erase beam were ordinary polarized for all the measurements reported here.

B. Sample preparation

The crystals used in our experiments were grown from a melt containing high purity starting materials and extreme care was taken to minimize melt contamination by the furnace. After growth of two high purity boules, several iron doped boules were grown from this melt at the concentrations 50, 500, and 1000 ppm in the melt. Samples from each of these boules were cut along (100) planes and then mechanically and electrically poled. One sample from each doping concentration was annealed at 800 °C in a reducing oxygen partial pressure or 10^{-4} atm. Another sample was prepared from a melt containing pure TiO_2 and
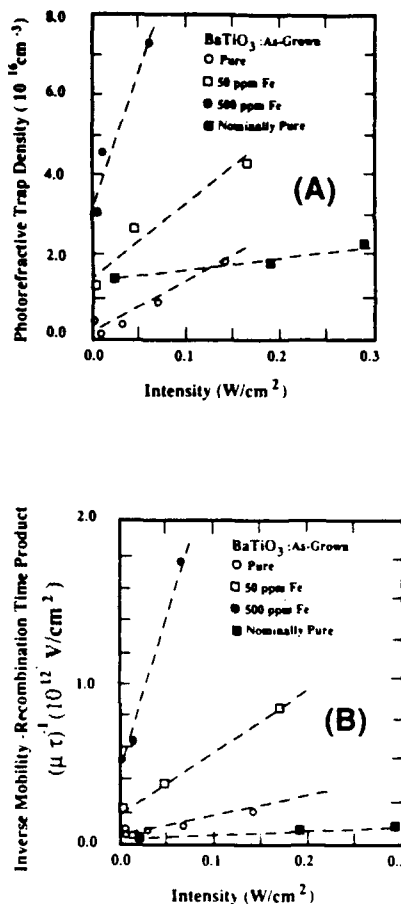

FIG. 3. Intensity dependence of (A) the trap density and (B) the mobility recombination time product in as grown $BaTiO_3$. The dashed lines are qualitative guides.

reagent grade BaO. This sample will be referred to as nominally pure since it was grown from the type of feed materials commonly used in the growth of $BaTiO_3$. For a more complete description of the growth and preparation of these samples the reader is referred to Ref. 15. Beam coupling measurements indicate that all the crystals exhibited p type conduction.[16]

IV. RESULTS AND DISCUSSION

The decay rate versus grating vector data was fitted to Eq. (2) for each erase beam intensity, and the parameters known as the photoconductivity σ_{ph}, the photorefractive trap density N_{pr}, and mobility recombination time product $\mu\tau$, were calculated from these fits. The results are plotted in Figs. 3, 4, and 5. The decay rate of the 1000 ppm crystals showed nonexponential behavior and was not suitable for this type of analysis.

The plots shown in Figs. 3 and 4 indicate that, for a given crystal, the trap density and the inverse of the mobility-recombination time product have very similar intensity dependencies. Since it is unlikely that the mobility is intensity dependent this would seem to indicate that the trap density is related to the recombination time as in Eqs. (4) and (5). This behavior was found for all the samples
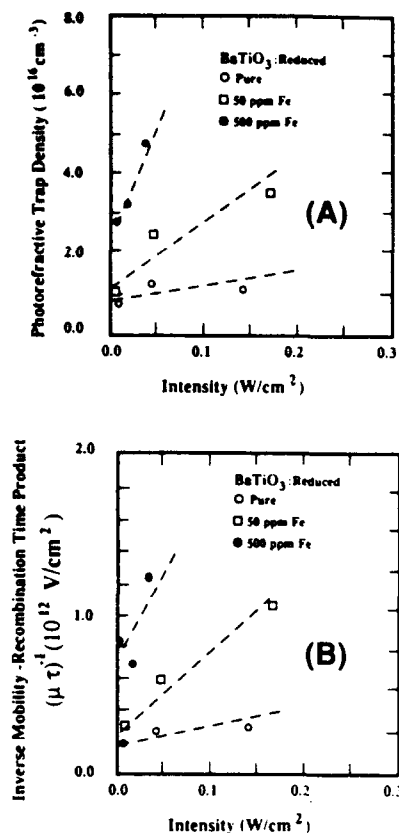
FIG. 4. Intensity dependence of (A) the trap density and (B) the mobility recombination time product in reduced BaTiO₃. The dashed lines are qualitative guides.

FIG. 5. Intensity dependence of the photoconductivity in (A) as grown BaTiO₃ crystals and (B) reduced BaTiO₃ crystals. The dashed lines are qualitative guides.

measured including the high purity sample and the nominally pure sample. The nonlinear intensity dependence of the photoconductivity, shown in Fig. 5, was found to be similar to that observed by Ducharme and Feinberg.[2,8]

Intensity dependent trap densities can be explained by the normal models through trap depletion. However, it is not unreasonable to assume that the intensity dependent recombination time and trap density are in some way related to the nonlinear photoconductivity. Since the transport seems to be well fitted by a diffusion type photoconductivity, as evidenced by the grating spacing dependence, modification of the model to include the intensity dependent effects may be possible. One possibility is a model, proposed by Rose, in which there exists a distribution of levels in the band gap.[17] However, direct of Rose's model does not seem appropriate since it disagrees with temperature dependencies reported by Ducharme and Feinberg.[8]

In conclusion, we have used the light-induced grating erasure technique to measure the intensity dependence of the photorefractive properties of pure and Fe doped BaTiO₃. Our results show that direct interpretation of the photorefractive models would lead to an intensity dependent trap density and recombination time with a strong correlation between the two. Further experiments, such as accurate measurements of the temperature dependence over a wider range of intensities, are needed before a sub-
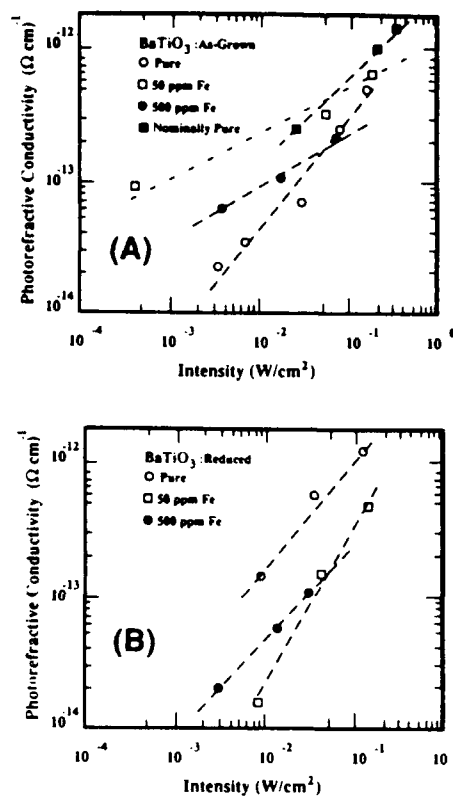
stantial modification of the photorefractive charge transport models can be accomplished.

[1] J. Feinberg, D. Heiman, A. R. Tanguay, Jr., and R. W. Hellwarth, J. Appl. Phys. 51, 1297 (1980).
[2] S. Ducharme and J. Feinberg, J. Opt. Soc. Am. B. 3, 283 (1986).
[3] M. B. Klein and R. N. Schwartz, J. Opt. Soc. Am. B. 3, 293 (1986).
[4] E. Kratzig, F. Welz, R. Orlowski, V. Doorman, and M. Rosenkranz, Solid State Commun. 34, 817 (1980).
[5] R. A. Mullin and R. W. Hellwarth, J. Appl. Phys. 58, 40 (1985).
[6] M. Carrascosa and F. Agullo-Lopez, IEEE J. Quantum Electron. 22, 1369 (1986).
[7] N. Kukharev, Sov. Tech. Phys. Lett. 2, 438 (1976).
[8] S. Ducharme and J. Feinberg, J. Appl. Phys. 56, 839 (1984).
[9] G. A. Brost, R. A. Motes, and J. R. Rotge, J. Opt. Soc. Am. B 5, 1879 (1988).
[10] S. I. Stepanov, M. P. Petrov, and A. A. Kashilin, Sov. Tech. Phys. Lett. 3, 345 (1977)
[11] N. V. Kukhtarev, E. Kratzig, H. C. Kulich, and R. A. Rupp, Appl. Phys. B. 35, 17 (1984).
[12] D. A. Temple and C. Warde, J. Opt. Soc. Am. B. 3, 337 (1986).
[13] J. Feinberg, in Phase Conjugate Optics, edited by R. Fisher (Academic, New York, 1984), Chap. 11.
[14] D. A. Temple and C. Warde, J. Opt. Soc. Am. B. 5, 1800 (1988).
[15] P. G. Schunemann, D. A. Temple, R. S. Hathcock, H. L. Tuller, H. P. Jenssen, D. R. Gabbe, and C. Warde, J. Opt. Soc. B 5, 1685 (1988)
[16] Beam coupling was measured in these samples by the authors and will be described in more detail in a future publication.
[17] A. Rose, Concepts in Photoconductivity and Allied Problems (Krieger, Huntington, NY, 1978)

6   (a) Anisotroptic Scattering in Photorefractive
Crystals
(b) Anisotropic Scattering in Photorefractive
Crystals : Reply to Comment

Anisotropic scattering in photorefractive crystals

Doyle A. Temple and Cardinal Warde

*Department of Electrical Engineering and Computer Science and Center for Materials Science and Engineering,
Massachusetts Institute of Technology, Cambridge, Massachusetts 02139*

A well-defined ring of anisotropically scattered light is observed when a linearly polarized laser beam is incident upon a birefringent photorefractive crystal such as $BaTiO_3$, $LiNbO_3$, and $LiTaO_3$. An analysis is presented that accurately predicts the cone angle, polarization, and the location of the discontinuities in these rings. Unlike the photovoltaic model proposed recently by others, the analysis presented herein is based on the standard photorefractive theory and is independent of the photovoltaic activity of the crystal. The analysis also illustrates the strict phase matching and electro-optic tensor symmetry constraints that must be satisfied in order to observe beam coupling and normal and anisotropic self-diffraction. Preliminary experimental results are presented for $BaTiO_3$ and $LiNbO_3$ and are found to be in excellent agreement with standard photorefractive theory.

INTRODUCTION

Anisotropic scattering of a linear, ordinary polarized laser beam into a conical ring of extraordinary polarized light was recently observed in $LiTaO_3$:Cu.[1] A theory based on the photovoltaic effect has been advanced to explain this phenomenon. It is claimed that the ring is a result of scattering from noisy dynamic gratings that are formed by photogalvanic currents in this material.[1]

In contrast, we show that standard photorefractive theory can explain the cone angle, polarization, and the location of the discontinuities in the anisotropically scattered diverging rings of light that have been observed in $BaTiO_3$ and doped $LiNbO_3$ and $LiTaO_3$.

Standard photorefractive theory shows that (a) the configuration most often used for wave mixing in photorefractive materials (which we shall refer to as the standard configuration) does not give rise to anisotropic diffraction and that (b) the interaction geometry that gives rise to anisotropic gratings in birefringent crystals is such that the c axis does not lie in the plane containing the grating vector $\mathbf{K}$ and the propagation vector $\mathbf{k}_R$ of the readout beam. We shall refer to the specific configuration in which the c axis is perpendicular to $\mathbf{K}$ and $\mathbf{k}_R$ as the anisotropic configuration.

In the anisotropic configuration, we further show (1) that beam coupling and normal self-diffraction are forbidden in some crystals for certain polarizations of the writing beams and (2) that anisotropic self-diffraction of the writing beams can occur only for specific grating periods and specific write light polarization.

Finally, we report a set of preliminary experiments on $BaTiO_3$ and $LiNbO_3$:Fe that confirm that the rings are adequately described by the standard photorefractive theory. The standard model was previously employed to explain anisotropic diffraction from holographic gratings in $LiNbO_3$:Fe (Refs. 2–4) and $BaTiO_3$,[5] but the conditions that permit grating formation without beam coupling and the observation of anisotropic scattering into ring segments were not reported.

THEORY

Consistent with standard photorefractive theory, we consider the holographic recording system shown in Fig. 1 in which two plane waves $\bar{\mathcal{E}}_1(\mathbf{r}, t)$ and $\bar{\mathcal{E}}_2(\mathbf{r}, t)$ with wave vectors $\mathbf{k}_1$ and $\mathbf{k}_2$ intersect in a photorefractive crystal. The steady-state plane-wave fields are of the form

$$\bar{\mathcal{E}}(\mathbf{r}, t) = \hat{e}A(r)\exp[i(\mathbf{k}\cdot\mathbf{r} - \omega t)] + \text{c.c.}, \qquad (1)$$

where A, ω, and $\hat{e}$ are the wave amplitude, frequency, and polarization vector, respectively, of the beams. The intensity pattern of the interfering beams induces a space-charge electric field $\mathbf{E}_{sc}$ by the photorefractive effect with the same spatial variation as the fringe pattern. That is, ignoring the spatial dc bias, we have

$$\mathbf{E}_{sc} = E(\hat{e}_1^* \cdot \hat{e}_2)\frac{\mathbf{A}_1^* \mathbf{A}_2}{I_0}\exp[i(\mathbf{K}\cdot\mathbf{r} + \phi)] + \text{c.c.}, \qquad (2)$$

where $\mathbf{r}$ is the position coordinate. $\mathbf{E} = E\hat{K}$ is the dc component of the space-charge field.[6,7] $I_0 = |A_1|^2 + |A_2|^2$, $\mathbf{K} = \mathbf{k}_2 - \mathbf{k}_1$ is the grating vector of the fringe pattern, and ϕ is the phase shift between the space-charge field and the intensity fringe pattern. The magnitude of ϕ depends on the specific charge-migration processes in the crystal.[6,7] The change in the susceptibility induced by this space-charge field is given by[8]

$$\Delta\bar{\chi} = -\bar{\epsilon}\cdot\bar{r}\cdot\mathbf{E}_{sc}\cdot\bar{\epsilon}, \qquad (3)$$

where $\bar{r}$ is the third-rank electro-optic tensor and $\bar{\epsilon}$ is the second-rank optical dielectric tensor. Using Eqs. (2) and (3), the change in the susceptibility can be written as

$$\Delta\bar{\chi} = \delta\bar{\chi}(\hat{e}_1^* \cdot \hat{e}_2)\frac{\mathbf{A}_1^* \mathbf{A}_2}{I_0}\exp[i(\mathbf{K}\cdot\mathbf{r} + \phi)] + \text{c.c.}, \qquad (4)$$

where

$$\delta\bar{\chi} = -\bar{\epsilon}\cdot\bar{r}\cdot\mathbf{E}\cdot\bar{\epsilon}. \qquad (5)$$

Now consider readout of this phase grating by a plane
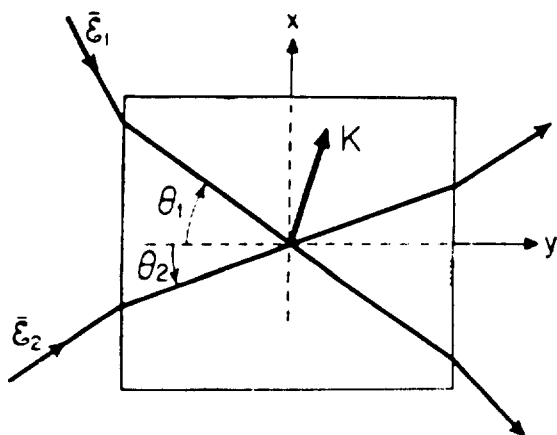
D. A. Temple and C. Warde

Fig. 1.   Setup for recording phase holograms in a photorefractive crystal.

wave of frequency ω_R. Using the slowly varying field approximation,[9] we can derive the following coupled-wave equations for the incident and diffracted readout beams (see Fig. 2):

$$\frac{\partial R}{\partial y} = -i\kappa_R e^{i\epsilon}\left(\frac{A^*_1 A_2}{I_0}\right)S, \qquad (6a)$$

$$\frac{\partial S}{\partial y} = -i\kappa_S e^{-i\epsilon}\left(\frac{A_1 A^*_2}{I_0}\right)R, \qquad (6b)$$

where R and S are the wave amplitudes of the incident and the diffracted readout beams, respectively. Here, the coupling coefficients κ_R and κ_S are given by

$$\kappa_R = \frac{\pi\chi_{eff}}{\eta_R\lambda_R\cos\alpha_R}, \qquad \kappa_S = \frac{\pi\chi_{eff}}{\eta_S\lambda_S\cos\alpha_S}, \qquad (7)$$

where $\lambda_R = \lambda_S$ is the wavelength of the readout and the diffracted beams. η_R, η_S, α_R, and α_S are the indices of refraction and the internal angles of the incident and the diffracted readout beams, respectively, and the effective susceptibility χ_{eff} is given by

$$\chi_{eff} = (\hat{e}_1\cdot\hat{e}_2)(\hat{e}_R\cdot\delta\bar{\chi}\cdot\hat{e}_S). \qquad (8)$$

where $\hat{e}_1$ and $\hat{e}_2$ are the polarization vectors of the writing beams and $\hat{e}_R$ and $\hat{e}_S$ are the polarization vectors of the incident and diffracted readout beams, respectively. We have also assumed that the phase-matching condition

$$\mathbf{K} = \mathbf{k}_R - \mathbf{k}_S \qquad (9)$$

is satisfied.

Therefore, in order for diffraction to be observed, generally two conditions must be simultaneously satisfied: (a) phase matching [Eq. (9)] and (b) χ_{eff} must be nonzero [Eq. (8)]. For the special case of anisotropic diffraction, the symmetry of the $\delta\chi$ tensor must be such that χ_{eff} is nonzero when $\hat{e}_R$ and $\hat{e}_S$ are orthogonal, and the refractive indices experienced by $\mathbf{k}_R$ and $\mathbf{k}_S$ must permit the phase-matching condition to be satisfied. It should be noted that beam coupling and self-diffraction are also described by Eq. (8) with the substitution $R = A_2$, $S = A_1$, $\hat{e}_R = \hat{e}_2$, $\hat{e}_S = \hat{e}_1$, and $\lambda_R = \lambda_S = \lambda$. In this case we get

$$\chi_{eff} = (\hat{e}_1^*\cdot\hat{e}_2)(\hat{e}_2\cdot\delta\chi\cdot\hat{e}_1^*). \qquad (10)$$

Based on this special form of χ_{eff}, it must be emphasized that with $(\hat{e}_1^*\cdot\hat{e}_2)\neq 0$ it becomes possible to write an anisotropic grating that exhibits no isotropic self-diffraction or two-beam coupling between the writing beams $(\hat{e}_2\cdot\delta\chi\cdot\hat{e}_1^* = 0)$. Specific examples are given in the section that follows.

SYMMETRY PROPERTIES OF THE COUPLING COEFFICIENT

Standard Configuration
In the standard configuration, the c axis is coplanar with both the grating vector and the wave vector of the readout beam. That is, the c axis is parallel to the x axis of the coordinate system, as shown in Fig. 2(a). The nonzero elements of the electro-optic tensor can be found in Ref. 9. Using these in Eq. (5), we find that $\delta\bar{\chi}$ for the standard configuration has the same form for the 4-mm, 2-mm, and 3-m crystal classes. That is,

$$\delta\bar{\chi} = \begin{pmatrix} \delta\chi_{11} & \delta\chi_{12} & 0 \\ \delta\chi_{21} & \delta\chi_{22} & 0 \\ 0 & 0 & \delta\chi_{33} \end{pmatrix}. \qquad (11)$$

Since $\delta\chi_{13} = \delta\chi_{31} = \delta\chi_{23} = \delta\chi_{32} = 0$, it follows from Eq. (8) that ordinary waves (z polarized) cannot couple to extraordinary waves (x-y polarized) and vice versa (i.e., anisotropic diffraction is forbidden). Since the diagonal elements of this tensor are nonzero, conventional-polarization isotropic beam coupling is allowed.

Anisotropic Configuration
In the anisotropic configuration, the c axis is perpendicular to the plane containing the grating vector and the wave vector of the readout beam. That is, the c axis is oriented along the z axis of the coordinate system, as in Fig. 2(b). In this case $\delta\bar{\chi}$ has the following forms:

For 3-m symmetry

$$\delta\bar{\chi} = -E\cos\gamma\begin{pmatrix} -n_o^4 r_{22} & -n_o^4 r_{22} & n_o^2 n_e^2 r_{42} \\ -n_o^4 r_{22} & n_o^4 r_{22} & 0 \\ n_o^2 n_e^2 r_{42} & 0 & 0 \end{pmatrix}. \qquad (12)$$

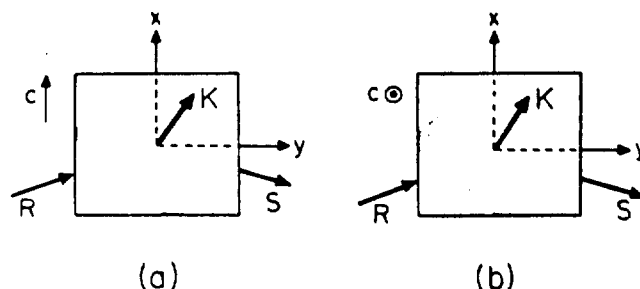(a)   (b)

Fig. 2.   Orientation of the c axis relative to the coordinate system of Fig. 1 for (a) the standard configuration and (b) the anisotropic configuration.
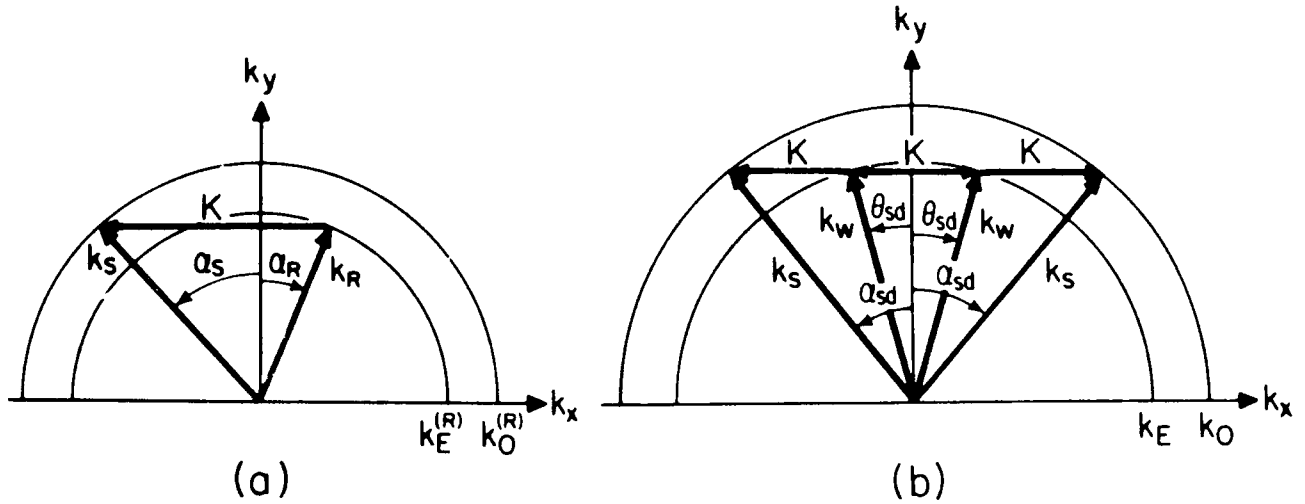
Fig. 3. (a) Wave-vector diagram for readout of an anisotropic grating of wave vector **K** in a negative birefringent crystal. (b) Wave-vector diagram illustrating anisotropic self-diffraction of extraordinary polarized write beams k_u into ordinary polarized beams k, (of −1 and +2 orders) in a negative birefringent crystal.

For 4-mm symmetry

$$\delta\tilde{\chi} = -En_o^2n_e^2r_{42}\begin{pmatrix} 0 & 0 & \cos\gamma \\ 0 & 0 & \sin\gamma \\ \cos\gamma & \sin\gamma & 0 \end{pmatrix} . \qquad (13)$$

For 2-mm symmetry

$$\delta\tilde{\chi} = -En_o^2n_e^2\begin{pmatrix} 0 & 0 & r_{51}\cos\gamma \\ 0 & 0 & r_{42}\sin\gamma \\ r_{51}\cos\gamma & r_{42}\sin\gamma & 0 \end{pmatrix} , \qquad (14)$$

where n_o and n_e are the ordinary and extraordinary indices of refraction, respectively, and γ is the angle that the grating vector **K** makes with the x axis. Since in each of these cases $\delta\chi_{13}$, $\delta\chi_{31}$, $\delta\chi_{23}$, and $\delta\chi_{42}$ are nonzero, it follows that for all three crystal classes anisotropic diffraction is allowed when the phase-matching condition [Eq. (9)] is satisfied. That is, diffraction of an ordinary wave (x–y-polarized) into an extraordinary wave (z-polarized) and vice versa is possible. However, since the elements along the main diagonal of the tensor are identically zero in the 4-mm and 2-mm crystals, coupling between the writing beams (ordinary or extraordinary polarizations) is forbidden. Additionally, since $\delta\chi_{33}$ is the only diagonal element that is zero in 3-m crystals [Eq. (12)], only coupling between extraordinary writing beams is forbidden in this case.

Phase Matching

To illustrate phase matching in an anisotropic photorefractive grating, we consider a grating formed in a negative birefringent ($n_o > n_E$) uniaxial crystal using the anisotropic configuration of Fig. 2(b). For gratings written with two beams, each of which makes an external θ' with the y axis, the grating vector is given by

$$\mathbf{K} = \frac{4\pi}{\lambda_W}\sin\theta'\hat{x}, \qquad (15)$$

where λ_W is the wavelength of the beams.

From the phase-matching condition [Eq. (9)] it follows that diffraction of an extraordinary readout probe beam of wavelength λ_R into an ordinary beam is allowed in this crystal when

$$\sin\alpha'_R = \left[\frac{\eta_0^2 - \eta_e^2}{4\sin\theta}\left(\frac{\lambda_W}{\lambda_R}\right) - \frac{\lambda_R}{\lambda_W}\sin\theta\right] . \qquad (16)$$

where α'_R is the external angle of incidence of the readout probe beam measured from the y axis and η_0 and η_E are the indices of refraction of the crystal at λ_R. Additionally, the external angle α'_s of the diffracted ordinary beam is given by

$$\sin\alpha'_s = \left[\eta_0^2 - \eta_e^2 - \sin^2\alpha'_R\right]^{1/2}. \qquad (17)$$

This phase-matching condition is also illustrated by the readout wave-vector diagram shown in Fig. 3(a). From reciprocity, an ordinary polarized probe beam incident upon the grating at an angle α'_s can diffract into an extraordinary beam at an external angle α'_R. To describe positive birefringent crystals, one simply interchanges η_0 and η_E in Eqs. (16) and (17).

Equation (16) can also be used to describe anisotropic self-diffraction of an extraordinary beam into an ordinary beam and vice versa. With the substitution $\lambda_R = \lambda_W$ and $\alpha_R = \theta$, the external Bragg angle for anisotropic self-diffraction into a −1 order and a +2 order becomes

$$\sin\theta'_{-d} = \frac{1}{2}\left(\frac{\eta_0^2 - \eta_e^2}{2}\right)^{1/2} . \qquad (18)$$

This indicates that only extraordinary beams can experience anisotropic self-diffraction in negative birefringent crystals by the standard photorefractive effect. This fact is confirmed by the wave-vector diagram of Fig. 3(b) that illustrates how the phase-matching condition is satisfied for anisotropic self-diffraction of extraordinary polarized beams in a negative uniaxial crystal.
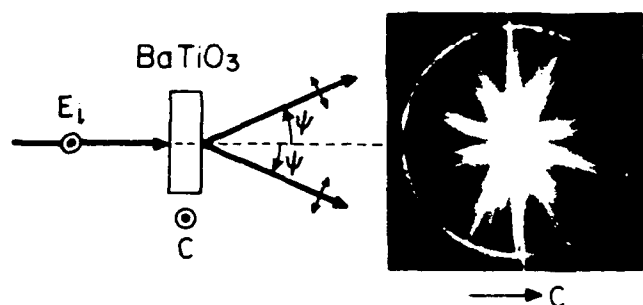
Fig. 4. Anisotropic scattering of an extraordinary polarized beam incident normally upon a BaTiO₃ crystal. Strong forward scattering into a ring of ordinary polarized light with discontinuities along the c axis is illustrated in the photograph.

EXPERIMENTAL RESULTS

Anisotropic Gratings

Anisotropic gratings were produced in single crystals of BaTiO₃ and doped LiNbO₃ by using the configuration of Fig. 2(b). Both writing beams of wavelength 488 nm had an intensity of 30 mW/cm² and were incident symmetrically about the a axis of each crystal at an angle θ.

Normal coupling between the writing beams was not observed in BaTiO₃ for either ordinary or extraordinary polarization over a wide range of incident angles. Examination of Eqs. (8) and (13) for the anisotropic configuration shows that for BaTiO₃ (4-mm symmetry) χ_{eff} is zero when $\hat{e}_R$ and $\hat{e}_S$ are both ordinary or both extraordinary, and hence beam coupling is indeed forbidden.

In negative birefringent BaTiO₃, the indices of refraction at 633 nm are $n_e = 2.36$ and $n_o = 2.42$.[10] For a grating written with 488-nm light at an incident angle of 20° (grating spacing $\Lambda = 0.7\ \mu m$), Eqs. (17) and (18) predict a Bragg angle of 17.2° and 24.7° for extraordinary and ordinary 633-nm-wavelength readout beams. The corresponding measured Bragg angles were 17.5° and 24.5° for extraordinary and ordinary beams, respectively. The intensity of the 633-nm readout laser beam was kept at 0.7 mW/cm² for all polarizations used. Both the ordinary and the extraordinary readout beams were observed to have the same diffraction efficiency (~20%).

As shown by the theory, anisotropic self-diffraction of

extraordinary beams is allowed in BaTiO₃ when the phase-matching condition [Eq. (9)] is satisfied [see Eqs. (8), (13), and (18) and Fig. 3(b)]. For 488-nm writing beams (n_e = 2.45 and n_o = 2.53),[10] the Bragg angle calculated by using Eq. (18) for anisotropic self-diffraction into a −1 and a +2 order is 12.5°. Experimentally, both writing beams were observed to undergo anisotropic self-diffraction at an input Bragg angle of 12.5°, with a diffraction efficiency of approximately 25% in the −1 order and less than 1% in the +2 order. From Eq. (18), it follows that there would be no anisotropic self-diffraction in BaTiO₃ for ordinary polarized writing beams, and none was observed. Similar results for anisotropic self-diffraction into the −1 order were reported recently by Kukhtarev et al.[5]

We have also observed anisotropic self-diffraction when one of the writing beams was an ordinary wave and the other was an extraordinary wave. In this case only the input extraordinary beam was observed to scatter weakly into a −1 order. Since the Bragg angle was the same, 12.5°, and we measured a 1% depolarization in the transmitted beams, we conclude that both writing beams experience depolarization in the crystal, allowing them to interfere and write an anisotropic photorefractive grating.

The Rings

When a single extraordinary (c-polarized) laser beam was incident upon the front surface of the BaTiO₃ and LiNbO₃:Fe crystals, a well-defined diverging ring of scattered light polarized perpendicular to the c axis (ordinary beam) was observed, in each case, leaving the back face of the crystal. The intensity in the ring was found to be maximum in the direction perpendicular to the c axis and zero along the c axis, as shown in the photograph of Fig. 4 for the BaTiO₃ crystal. The ring generated by the LiNbO₃:Fe crystal was much weaker than that produced by the BaTiO₃ crystal. We believe that the rings are formed by diffraction of the incident beam from noisy anisotropic gratings that satisfy the phase-matching condition for diffraction into −1-order beams. These gratings are a subset of those produced through interference between light scattered from optical imperfections in the crystal and the incident beam.

For simplicity, consider this process in the a–b plane of the crystal [Fig. 5(a)]. The incident beam $\mathbf{k}_i$ scatters in many

(a)   (b)
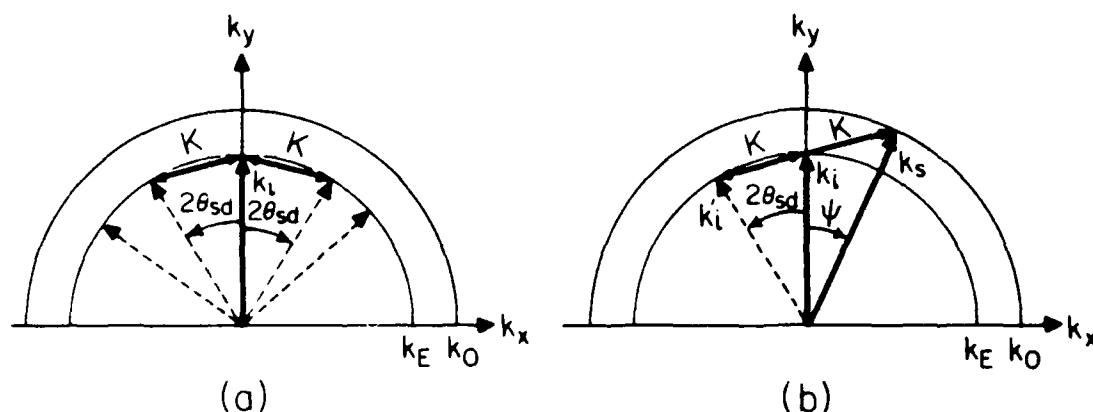
Fig. 5. Wave-vector diagrams illustrating how the rings are formed by scattering in BaTiO₃ and LiNbO₃. (a) Shows how a typical grating vector in the a–b plane is written by interference between the incident extraordinary polarized beam and a randomly scattered beam. (b) Shows one of the specific grating vectors in the a–b plane that allows anisotropic self-diffraction of the incident beam into a −1-order beam on the ring.

directions, but only two of the scattered beams $\mathbf{k}'$, lie at an angle $2\theta_{sd}$ such that the grating vector $\mathbf{K}$ allows anisotropic self-diffraction of the incident beam into a -1-order beam $\mathbf{k}$, [Fig. 5(b)]. Following an analysis similar to that of Eq. (18), the external apex angle of the ring in the a–b plane is given by

$$\sin \psi' = \left[n_o^2 - \left(\frac{3n_e^2 + n_o^2}{4n_e} \right)^2 \right]^{1/2} . \qquad (19)$$

For BaTiO$_3$ this equation leads to an apex angle 2ψ of 50° for normally incident 488-nm light. This is in excellent agreement with the measured apex angle of 50.2°. Similarly, in LiNbO$_3$:Fe the calculated and measured angles of the ring in the a–b plane are 52° and 51°, respectively. In general, this type of phase matching is allowed in a ring around the incident beam. The discontinuity observed in the ring corresponds to the case in which the c axis lies in the plane containing the grating vector and the incident beam (standard configuration). This is consistent with the photorefractive theory that shows that anisotropic diffraction is forbidden in both LiNbO$_3$ and BaTiO$_3$ for this case.

A similar anisotropically scattered ring has been reported by Odulov et al.[1] in a LiTaO$_3$:Cu crystal (positive birefringence) with an ordinary polarized input beam. These authors assume that the ring was produced by noisy gratings formed by the photovoltaic effect from interference between orthogonally polarized light beams. Their photovoltaic model predicts an apex angle of 15° in LiTaO$_3$ ($n_o = 2.248$ and $n_E = 2.252$ at $\lambda = 440$ nm), which appears to be in relatively good agreement with their measured value of 13°. However, the photovoltaic theory does not predict the observed discontinuity in the ring along the c axis, and, when applied to BaTiO$_3$, it predicts an apex angle of 75°, which does not agree with the observed value of 50.2°.

If, however, we assume that the ring observed in LiTaO$_3$ was produced by an anisotropic grating through the normal photorefractive effect, Eq. (19) would predict an apex angle of 11°, which is also in good agreement with the measured value.

CONCLUDING REMARKS

Using standard photorefractive theory, we have described the symmetry and phase-matching conditions that must be satisfied in order to write anisotropic gratings in birefringent photorefractive crystals. We have identified the specific configurations for writing anisotropic gratings that do not permit coupling between the writing beams. Such gratings were written in BaTiO$_3$, and indeed no beam coupling was observed. However, these gratings could be read out by a laser beam of a different wavelength.

Anisotropic self-diffraction was shown to occur for only one polarization of the writing beams and at only one grating spacing. For BaTiO$_3$, LiNbO$_3$:Fe, and LiTaO$_3$, anisotropic self-diffraction into -1 and $+2$ orders is possible, and we have observed both orders in BaTiO$_3$.

A ring of anisotropically scattered light has been observed when each of these materials was illuminated with a single laser beam. This ring was shown to be formed by diffraction from noisy anisotropic gratings that satisfy the phase-matching condition for self-diffraction into a -1 order. A previous model,[1] which was based on gratings produced by the photovoltaic effect, does not consistently predict the observed apex angle and the discontinuities in the ring of light scattered from these materials. In contrast, the photorefractive analysis presented herein consistently predicts both the apex angle and the discontinuities in the ring for each of the above materials.

REFERENCES

1. S. Odulov, K. Belabaev, and I. Kiseleva, "Degenerate stimulated parametric scatering in LiTaO$_3$," Opt. Lett. 10, 31 (1985).
2. S. I. Stepanov, M. P. Petrov, and A. A. Kamshilin, "Optical diffraction with polarization-plane rotation in a volume hologram in an electro-optic crystal," Sov. Tech. Phys. Lett. 3, 345 (1977).
3. N. V. Kukhtarev and S. G. Odulov, "Wavefront inversion in anisotropic self-diffraction of laser beams," Sov. Tech. Phys. Lett. 6, 503 (1980).
4. N. V. Kukhtarev, "Wavefront reversal of optical beams in anisotropic media," Sov. J. Quantum Electron. 11, 878 (1981).
5. N. V. Kukhtarev, E. Kratzig, H. C. Kulich, R. A. Rupp, and J. Albers, "Anisotropic self-diffraction in BaTiO$_3$," Appl. Phys. Lett. B 35, 17–21 (1984).
6. N. V. Kukhtarev, V. B. Markov, S. G. Odulov, M. S. Soskin, and V. L. Vinetskii, "Holographic storage in electro-optic crystals. I. Steady state," Ferroelectrics 22, 949 (1979).
7. J. Feinberg, D. Heiman, A. R. Tanguay, Jr., and R. W. Hellwarth, "Photorefractive effects and light-induced charge migration in barium titanate," J. Appl. Phys. 51, 1297 (1980).
8. J. Feinberg, "Optical phase conjugation in photorefractive materials," in Phase Conjugate Optics, R. Fisher, ed. (Academic, New York, 1983).
9. A. Yariv and P. Yeh, Optical Waves in Crystals (Wiley, New York, 1984).
10. S. H. Wemple, M. DiDomenico, Jr., and I. Camlibel, "Dielectric and optical properties of melt-grown BaTiO$_3$," J. Phys. Chem. Solids 29, 1797 (1968).

Anisotropic scattering in photorefractive materials: reply to comment

Doyle A. Temple and Cardinal Warde

Department of Electrical Engineering and Computer Science, Massachusetts Institute of Technology, Cambridge, Massachusetts 01239

In response to Odoulov's comment [J. Opt. Soc. Am. B 4, 1333 (1987)], we show that, for gratings established through the tensor photovoltaic effect, anisotropic scattering along the c axis in 3m crystals is not forbidden by symmetry.

In an earlier paper, Odoulov *et al.*[1] reported on the observation of a single ring of anisotropically scattered light with an apex half-angle of 6.5° for a LiTaO₃ crystal that was pumped with a single ordinary polarized beam. A tensor photovoltaic model, which predicted an angle of 7.5°, was advanced in that paper. In our previous paper[2] we proposed a photorefractive three-wave mixing interaction that explained the rings that we had observed in BaTiO₃ and LiNbO₃, and it predicted an angle of 5.5° for LiTaO₃. Because (1) the measured cone angle in LiTaO₃ was equally close to the calculated photovoltaic and photorefractive values, and (2) the photovoltaic model does not accurately predict the apex angle of the rings that we observed in BaTiO₃ and LiNbO₃ or explain the nulls in the rings along the c axis, we concluded that the authors had not sufficiently proved that the single ring that they had observed in LiTaO₃ was due to the photovoltaic effect.

In light of their new data, which now show two rings, we agree that the ring that they originally observed may be due to the photovoltaic effect. However, our statement that the photovoltaic model, as presented in their paper, does not forbid anisotropic scattering along the c axis is correct, as is shown below.

A normal photorefractive grating is produced by a spatially varying intensity pattern that induces charge redistribution through diffusion. Because of the nature of this process, the space-charge field is directed along the grating vector. Using this constraint, it was shown in Ref. 2 that anisotropic diffraction along the c axis of 3m crystals is forbidden by symmetry for normal photorefractive gratings.

On the other hand, photovoltaic-induced gratings are produced by an asymmetry in the photoionization and recombination processes, which are in turn related to the spatial dependence of the ellipticity of the polarization of the optical field within the crystal. Consider two waves (ordinary and extraordinary), intersecting in the plane containing the c axis (see Fig. 1).

Let the ordinary-polarized pump wave

$$\mathbf{E}_p = \hat{x} A_p \exp[i(\mathbf{k}_p \cdot \mathbf{r} - \omega t)] + \text{c.c.} \tag{1}$$

and the extraordinary scattered wave

$$\mathbf{E}_s = A_s (\hat{z} \cos\theta - \hat{x} \sin\theta)\exp[i(\mathbf{k}_s \cdot \mathbf{r} - \omega t)] + \text{c.c.} \tag{2}$$

intersect in the crystal at an angle θ in the plane containing the c axis, as shown. According to Refs. 1, 4, and 5, the associated photovoltaic currents are given by

$$J_i = \beta_{ijk} E_j E_k^*, \tag{3}$$

where β_{ijk} are the photovoltaic tensor elements and E_j and E_k are the electric-field amplitudes of the light waves.

Based on the symmetry of the β_{ijk} tensor for 3m crystals (independent symmetric elements are β_{333}^s, β_{133}^s, β_{222}^s, and β_{131}^s and the antisymmetric elements are β_{131}^a and β_{113}^a), we see that spatially oscillating currents along the grating vector $\mathbf{K} = \mathbf{k}_s - \mathbf{k}_p$ are forbidden for the geometry shown in Fig. 1. However, current J_1 perpendicular to the grating vector is not forbidden, as can be seen when Eqs. (1) and (2) are substituted into Eq. (3). Since the resulting space-charge field is given by $E_i^{sc} = J_i/\sigma_{ii}$, where σ_{ii} is the photoconductivity, the photovoltaic model predicts a space-charge field that is directed along the x axis and spatially modulated in the y-z plane of Fig. 1. For 3m crystals, such a space-charge field would induce a change in susceptibility through the electro-optic effect that is given by

$$\Delta\chi_{ij} = -\epsilon_{ii} r_{imn} E_n^{sc} \epsilon_{mj} \tag{4}$$

and has the form

$$\Delta\chi = \begin{bmatrix} 0 & \Delta\chi_{12} & \Delta\chi_{13} \\ \Delta\chi_{21} & 0 & 0 \\ \Delta\chi_{31} & 0 & 0 \end{bmatrix}. \tag{5}$$
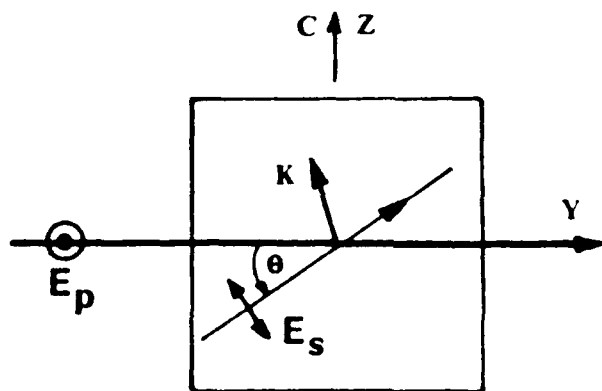

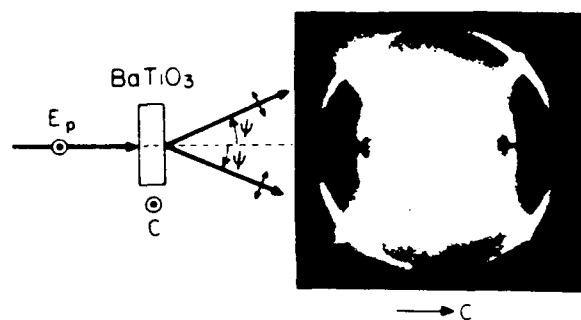Fig. 1. The scattering configuration under consideration.

56

Fig. 2.   Anisotropic scattering of a single extraordinary-polarized pump beam into two ordinary-polarized rings (with nulls) in a heavily doped BaTiO₃:Fe crystal (1000 parts in 10⁶ Fe in melt).

The symmetry of Eq. (5) shows that coupling between orthogonally polarized beams in the y-z plane is allowed. The strength of this coupling is, of course, dependent on the photoconductivity and the magnitude of the photovoltaic and electro-optic tensor elements involved, but it is not forbidden by symmetry. Therefore, unlike in the standard photorefractive case, the photovoltaic space-charge fields for the configuration in Fig. 1 are perpendicular to the grat-

ing vector $\mathbf{K}$ and can lead to anisotropic diffraction along the c axis.

In addition to the single ring (apex half-angle of 25.1°) that we reported earlier in Ref. 2 for an nominally undoped BaTiO₃ crystal, we recently observed a second anisotropically scattered ring from a heavily doped BaTiO₃:Fe crystal (1000 parts in 10⁶ Fe in melt). This second ring is much weaker than the first and contains two pairs of nulls located along the c and a axes, as shown in Fig. 2. This second ring satisfies the phase-matching equation

$$2\mathbf{k}_p'' = \mathbf{k}_{s1}'' + \mathbf{k}_{s2}'' \tag{6}$$

with a measured apex half-angle of 37.5°.

The authors are also with the Center for Materials Science and Engineering, Massachusetts Institute of Technology.

REFERENCES

1. S. G. Odoulov, K. Belabaev, and I. Kiseleva, Opt. Lett. **10**, 31 (1985).
2. D. A. Temple and C. Warde, J. Opt. Soc. Am. B. **3**, 337 (1986).
3. V. I. Belinicher, Phys. Lett. A **66**, 213 (1978).
4. E. M. Avakyan, K. G. Belabaev, and S. G. Odoulov, Sov. Phys. Solid State **25**, 1887 (1983).
5. S. G. Odoulov, JETP Lett. **35**, 10 (1982).

7 High-Order Anisotropic Diffraction in Photorefracitve Crystals

High-order anisotropic diffraction in photorefractive crystals

D. A. Temple and C. Warde

Department of Physics, Massachusetts Institute of Technology, Cambridge, Massachusetts 02139

High-order anisotropic diffraction and anisotropic self-diffraction in barium titanate (BaTiO₃), strontium barium niobate (Sr$_x$Ba$_{1-x}$Nb$_2$O$_6$, or SBN), and barium strontium potassium sodium niobate (Ba$_{2-x}$Sr$_x$K$_{1-y}$Na$_y$Nb$_5$O$_{15}$, or BSKNN) have been observed: up to fourth order in BaTiO₃ and SBN and up to fifth order in BSKNN. It is shown that the scattered beams arising from anisotropic self-diffraction are composed of multiple orders. To model anisotropic diffraction, high-order terms have been included in Kukhtarev's solution of the transport equations for diffusion-dominated transport. Light-induced grating decay rates and diffraction efficiencies were measured as a function of grating vector and modulation index for the first three orders in BaTiO₃ and were found to be in good agreement with the model.

1. INTRODUCTION

Anisotropic photorefractive gratings[1,2] are characterized by the property that, under the proper phase-matching conditions, an ordinary polarized readout beam can diffract into an extraordinary polarized beam and vice versa. Holographic recording of anisotropic photorefractive gratings in electro-optic crystals has been studied extensively in recent years.[1-9] In the simplest case this involves gratings whose wave vectors lie in the plane perpendicular to the c axis.

The diffraction efficiencies and rise times of these gratings were used to determine the photoconductivities and diffusion lengths of these materials. Measurement of the phase-matching angles was used to determine the birefringence.[3] The signal-processing applications include such novel techniques as dynamic light deflection,[4] spatial light modulation,[5] wave-front inversion,[6,7] and, more recently, amplified reflection through anisotropic four-wave mixing.[8] Also, anisotropic scattering into conical rings of light was shown to be the result of anisotropic gratings written through interference between the incident pump beam and beams scattered in the crystal owing to optical inhomogeneities.[3,9] The angular dependence of this cone was used to determine the dispersion of the birefringence in KNbO₃.[3] In general, the polarization orthogonality of the readout and diffracted beams results in an improved signal-to-noise ratio, as pointed out by Stepanov et al.[1]

Anisotropic diffraction into a second order was observed previously[9] in BaTiO₃ by using the configuration for anisotropic self-diffraction.[2,9] In this case extraordinary polarized writing beams intersect in the x-y plane of the crystal to form an anisotropic photorefractive grating. These writing beams simultaneously diffract into both a first and a second order. Modeling in this instance is complicated by the coupling of the two writing beams to the four diffracted beams.

In this paper we investigate high-order anisotropic diffraction in barium titanate (BaTiO₃), strontium barium niobate (Sr$_{1-x}$Ba$_x$Nb$_2$O$_6$, or SBN), and barium strontium potassium sodium niobate (Ba$_{2-x}$Sr$_x$K$_{1-y}$Na$_y$Nb$_5$O$_{15}$, or BSKNN), and we report the first observation, to our knowledge, of anisotropic self-diffraction into orders higher than the second in these materials. We also show that the aniso-

tropically scattered beams arising from anisotropic self-diffraction are composed of multiple orders. To model high-order anisotropic diffraction, we use a perturbation approach, similar to that used by Refregier et al.,[10] for including high-order terms in the model of Kukhtarev et al.[11] Using this model, we derive (1) approximate solutions for the grating vector dependence of the second- and third-order light-induced grating decay rates and (2) the modulation index dependence of the diffraction efficiency of these orders. We have measured both of these characteristics for the first three orders in BaTiO₃ and have found reasonable fits to the model. We also report our measurements on anisotropic self-diffraction into orders as high as the fourth order in BaTiO₃ and SBN and the fifth order in BSKNN.

2. ANISOTROPIC DIFFRACTION

To review the coupling permitted for anisotropic gratings in 4-mm crystals, consider the grating formed by the intersection of two coherent ordinary polarized plane waves with amplitudes A_1 and A_2 and wave vectors $\mathbf{k}_1$ and $\mathbf{k}_2$ incident symmetrically about the y axis of a 4-mm crystal, as shown in Fig. 1(a). In this case the grating vector $\mathbf{K} = \mathbf{k}_1 - \mathbf{k}_2$ is along the x axis of the crystal. The resulting interference fringes induce a sinusoidal distribution in the photogenerated carriers, which set up a space-charge field with the same spatial periodicity as the fringe pattern. This space charge then modulates the refractive index through the electro-optic effect.

Now consider readout of this grating, as in Fig. 1(b), by a steady-state plane-wave field of the form

$$\mathbf{A}(r, t) = \hat{e}A(r)\exp[i(\mathbf{k} \cdot \mathbf{r} - \omega t)] + \text{c.c.}, \qquad (1)$$

where $\hat{e}$ and ω are the polarization vector and the frequency, respectively. The coupled-wave equations governing diffraction are

$$\frac{\partial R}{\partial y} = -i\kappa_r S, \qquad (2)$$

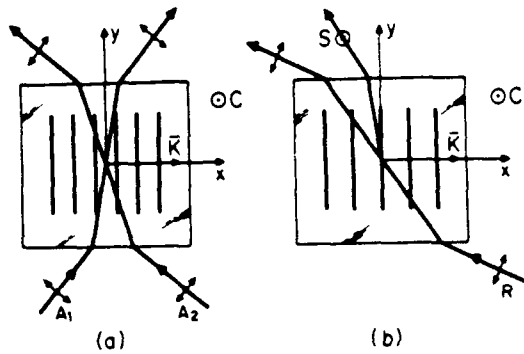$$\frac{\partial S}{\partial y} = -i\kappa_s R. \qquad (3)$$

Fig. 1. Schematic diagrams illustrating (a) writing and (b) readout of an anisotropic photorefractive grating in a 4-mm crystal. In (a) the writing beams A_1 and A_2 intersect in the crystal, producing a photorefractive grating with a wave vector $\mathbf{K} = \mathbf{k}_2 - \mathbf{k}_1$. In (b) an ordinary polarized readout beam R scatters into an extraordinary polarized beam S, where $\mathbf{k}_s = \mathbf{k}_R + \mathbf{K}$.
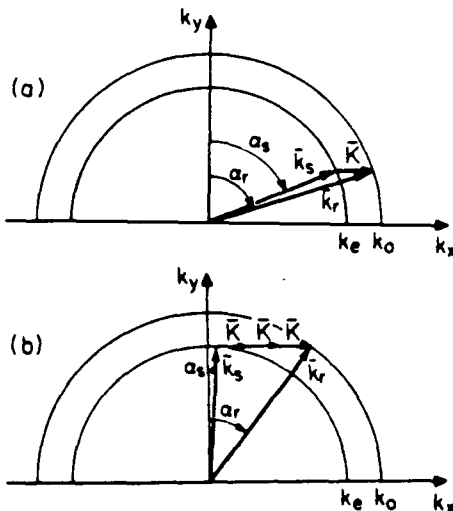

Fig. 2. Phase-matching diagrams showing (a) anisotropic first-order readout of a grating of wave vector $\mathbf{K}$ and (b) anisotropic third-order readout of the same grating.

where R and S are the wave amplitudes of the readout and diffracted beams, respectively. The coupling coefficients are given by

$$\kappa_r = \frac{\pi \chi_{\text{eff}}}{n_r \lambda_r \cos(\alpha_r^{\text{in}})}, \tag{4}$$

$$\kappa_s = \frac{\pi \chi_{\text{eff}}}{n_s \lambda_s \cos(\alpha_s^{\text{in}})}, \tag{5}$$

where $\lambda_r = \lambda_s$ is the wavelength of the readout and diffracted beams and n_r, n_s, α_r^{in}, and α_s^{in} are the indices of refraction (n's) and angles (α's) inside the crystal of the readout and diffracted beams, respectively. The effective susceptibility χ_{eff} is

$$\chi_{\text{eff}} = (\hat{e}_2{}^* \cdot \hat{e}_1)(\hat{e}_r \cdot \delta\bar{\chi} \cdot \hat{e}_s), \tag{6}$$

where

$$\delta\bar{\chi} = -\bar{\epsilon} \cdot \hat{\bar{r}} \cdot \mathbf{E}_{\text{sc}} \cdot \bar{\epsilon}. \tag{7}$$

$\hat{\bar{r}}$ is the third-rank electro-optic tensor, $\bar{\epsilon}$ is the second-rank optical dielectric tensor, and $\mathbf{E}_{\text{sc}}$ is the space-charge field.

As shown previously,[9] for this crystal orientation, ordinary polarized writing beams cannot self-diffract from such a grating ($\hat{e}_1{}^* \cdot \delta\chi \cdot \hat{e}_2 = 0$). In this case, the intensity fringe pattern in the crystal is uniform, assuming small absorption. Without this coupling the assumptions in the charge-transport models of Kukhtarev et al.[11] and Feinberg et al.[12] are more valid than for the case of strong beam coupling. Equations (2)–(7) also show that an ordinary polarized readout beam can diffract only into an extraordinary polarized beam for gratings produced as in Fig. 1(a).

The phase-matching condition required for observing anisotropic diffraction into high orders is illustrated in Fig. 2. As shown in Fig. 2(a), the readout beam can undergo first-order diffraction into an extraordinary polarized beam when the phase-matching condition $\mathbf{K} = \mathbf{k}_s - \mathbf{k}_r$ is satisfied. However, as illustrated in Fig. 2(b), for a given grating vector $\mathbf{K}$ the phase-matching condition may be satisfied for higher orders of K. This condition can be expressed as $M\mathbf{K}_s = \mathbf{K}_s - \mathbf{K}_r$ or as

$$\sin(\alpha) = \frac{\lambda_W (n_0{}^2 - n_e{}^2)}{M\lambda_r \sin\theta} - \frac{\lambda_r M \sin\theta}{\lambda_W}, \tag{8}$$

where α is the angle of the extraordinary beam outside the crystal; n_o and n_e are the ordinary and extraordinary indices of refraction, respectively, at the readout-beam wavelength; λ_W and λ_r are the writing- and readout-beam wavelengths, respectively; M is the diffracted order; and θ is the writing-beam angle outside the crystal.

Because ordinary polarized writing beams in 4-mm crystals do not experience beam coupling for grating vectors in the x–y plane, these gratings fit closely the model of Kogelnik.[13] Therefore the diffraction efficiency of Mth order is given by

$$\eta = \left| \frac{S(d)}{R(0)} \right|^2 = \sin^2 |D| d, \tag{9}$$

where

$$|D|^2 = \frac{\pi^2 (\hat{e}_1 \cdot \hat{e}_2{}^*)^2 (\hat{e}_R \cdot \delta\bar{\chi} \cdot \hat{e}_S)^2}{n_r n_s \lambda_r{}^2 \cos\alpha_r \cos\alpha_s} \tag{10}$$

and

$$\delta\bar{\chi} = -\bar{\epsilon} \cdot (\hat{\bar{r}} \cdot \mathbf{E}_M) \cdot \bar{\epsilon}, \tag{11}$$

where E_M is the Mth-order space-charge field, d is the crystal thickness, n_r and n_s are the refractive indices of the readout and scattered beams, respectively, α_r and α_s are the angles of propagation in the crystal, $I_0 = I_1 + I_2$, and λ_r is the readout-beam wavelength.

3. LIGHT-INDUCED GRATING DYNAMICS

The equations used to describe the photorefractive response of a material are given by[11]

$$\frac{\partial n_e}{\partial t} = \frac{\partial N_D{}^+}{\partial t} + \frac{1}{e} \nabla J, \tag{12}$$

$$\frac{\partial N_D{}^+}{\partial t} = \left(\frac{\sigma}{h\nu} I + \beta \right)(N_D - N_D{}^+) - \gamma_R n N_D{}^+, \tag{13}$$

$$J = e\mu n E_{\text{sc}} + eD\nabla n, \tag{14}$$

60

$$\nabla(\epsilon\epsilon_0 E_{sc}) = e(N_D^+ - N_A - n), \tag{15}$$

where n_e, N_D, N_A, and N_D^+ are the concentrations of the free electrons, donors, acceptors, and ionized donors, respectively, e is the charge on an electron, J is the current density, σ is the photoconductivity, I is the intensity, D is the diffusion constant, γ_R is the recombination rate, β is the thermal generation rate, ϵ is the relative dielectric constant, μ is the mobility, and E_{sc} is the space-charge field. For anisotropic gratings in the $x-y$ plane of 4-mm crystals, the fringes are flat and planar for ordinary polarized writing beams, and the fringe intensity distribution is given by

$$I = I_0\left[1 + \frac{m}{2}\exp(iKx) + \text{c.c.}\right]. \tag{16}$$

Hence the generation rate at any point in the grating is constant, assuming no charge depletion. We assume solutions of the form

$$N_D^+ = N_{D o}^+ + \tfrac{1}{2}[N_{D1}^+ \exp(iKx) + \text{c.c.}], \tag{17}$$

$$n = n_0 + \tfrac{1}{2}[n_1 \exp(iKx) + \text{c.c.}], \tag{18}$$

$$J = J_0 + \tfrac{1}{2}[J_1 \exp(iKx) + \text{c.c.}], \tag{19}$$

$$E_{sc} = E_0 + \tfrac{1}{2}[E_1 \exp(iKx) + \text{c.c.}], \tag{20}$$

where N_{D1}^+, n_1, J_1, and E_1 are the modulated portion of the ionized donor density, free-electron density, current density, and space-charge field, respectively, and $m = 2(\hat{e}_1 \cdot \hat{e}_2)(I_1 I_2)^{1/2}/(I_1 + I_2)$. Then the decay rate of the first-order space-charge field is given by[11,12]

$$\frac{1}{\tau} = \frac{e\mu n_0}{\epsilon}\left[\frac{1 + \left(\dfrac{\epsilon kT}{N_T e^2}\right)K^2}{1 + \left(\dfrac{\mu kT}{\gamma N_A e}\right)K^2}\right], \tag{21}$$

where $N_T = (N_D/N_A)(N_D - N_A)$.

To solve for the high-order harmonics of the grating we can use a perturbation approach[10] by assuming high-order solutions of the form

$$N_D^+ = N_{D o}^+ + \tfrac{1}{2}[N_{D1}^+ \exp(iKx) + \cdots$$
$$+ N_{DM}^+ \exp(MiKx) + \text{c.c.}], \tag{22}$$

$$n = n_0 + \tfrac{1}{2}[n_1 \exp(iKx) + \cdots + n_M \exp(MiKx) + \text{c.c.}], \tag{23}$$

$$J = J_0 + \tfrac{1}{2}[J_1 \exp(iKx) + \cdots + J_M \exp(MiKx) + \text{c.c.}], \tag{24}$$

$$E_{sc} = E_0 + \tfrac{1}{2}[E_1 \exp(iKx) + \cdots + E_M \exp(MiKx) + \text{c.c.}]. \tag{25}$$

For a second-order perturbation, we (1) neglect orders in the harmonic solutions higher than the second order; (2) assume that the second-order space-charge field does not significantly affect the first-order space-charge field, that is, the first-order solution is still valid; and (3) neglect any gratings written by interference of high-order diffracted beams. Using these assumptions, we substitute Eqs. (22)–(25) into Eqs. (12)–(15) and group terms with $\exp(2iKx)$. From this we find the time dependence of the second-order space-charge field to be

$$\frac{dE_2}{dt} = -\frac{E_2}{\tau_2} - A(K)mE_1 - B(K)E_1^2, \tag{26}$$

where

$$\frac{1}{\tau_2} = \frac{e\mu n_0}{\epsilon}\left[\frac{1 + (kT\epsilon/e^2 N_T)(2K)^2}{1 + (\mu kT/\gamma N_A)(2K)^2}\right], \tag{27}$$

$A(K)$ and $B(K)$ are functions of K, and E_1 is the first-order space-charge field derived previously.[11,12]

For light-induced erasure of a previously written grating, the general solution of Eq. (26) is

$$E_2 = E_{2a}\exp\left(\frac{-t}{\tau_2}\right) + \left(\frac{A_1 m}{1/\tau - 1/\tau_2}\right)\exp\left(\frac{-t}{\tau}\right)$$
$$+ \left(\frac{B_1}{2/\tau - 1/\tau_2}\right)\exp\left(\frac{-2t}{\tau}\right), \tag{28}$$

where we have used the fact that the first-order field decays at a rate $\exp(-t/\tau)$. This shows that in general the erasure rate of the second order is nonexponential. However, depending on the relative sizes of τ_2, A_1, and B_1, the decay rate could resemble that of a single exponential with a decay time of τ_2. Also, because the first-order space-charge field is proportional to m, we see from Eq. (26) that the second-order space-charge field is proportional to m^2.

Similarly, using the results for the first- and second-order space-charge fields and applying third-order perturbation theory, we find that the expression governing the time dependence of the third-order space-charge field is

$$\frac{dE_3}{dt} = -\frac{E_3}{\tau_3} - F(E_1^3, E_2 E_1), \tag{29}$$

where F is a complex function of the first- and second-order fields. This shows that in general the decay rate of the third order is also nonexponential. However, when the driving term F is small the grating can show an exponential decay with a single decay time τ_3, where

$$\frac{1}{\tau_3} = \frac{e\mu n_0}{\epsilon}\left[\frac{1 + \dfrac{\epsilon kT}{e^2 N_T}(3K)^2}{1 + \dfrac{\mu kT}{\gamma N_A}(3K)^2}\right]. \tag{30}$$

Now, because the complex function F contains terms such as E_1^3 and $E_1 E_2$, we see from Eq. (29) that the third-order space-charge field is proportional to m^3. It is interesting to note that when the decay rates of the three orders are single exponentials, the decay times have the same form: the first order is a function of K, the second order is a function of $2K$, and the third order is a function of $3K$.

BaTiO$_3$, SBN, and BSKNN crystals were cut along the (100) axis, polished to optical quality, and poled to obtain approximately single-domain material. In particular, the BaTiO$_3$ crystal was grown from a melt containing high-purity BaO and TiO$_2$, with extra precautions taken to minimize melt contamination from the furnace.

High-order diffraction efficiencies and decay rates of anisotropic diffraction were measured for the high-purity sample of BaTiO$_3$ up to third order. The writing and erase beams all originated from an argon-ion laser (Coherent Innova 70) operating in the TEM$_{00}$ mode with $\lambda = 488$ nm.

The readout beam (λ = 633 nm) was chopped at a frequency of 1000 Hz, and the diffracted beam was sychronously detected by using a photomultiplier tube and a lock-in amplifier. The output of the lock-in amplifier was fed to an AT&T 6300 computer equipped with a Data Translation data-acquistion board with the sampling rate set at 80 Hz.

The light-induced decay rates of the first three orders in $BaTiO_3$ were found to be well fitted by a single exponential. Beam-coupling measurements on this sample determined the dominant conduction mechanism to be holes with practically no hole–electron competition. Nonexponential decays were observed for high-order anisotropic diffraction in the SBN and BSKNN crystals; thus our most detailed experi-
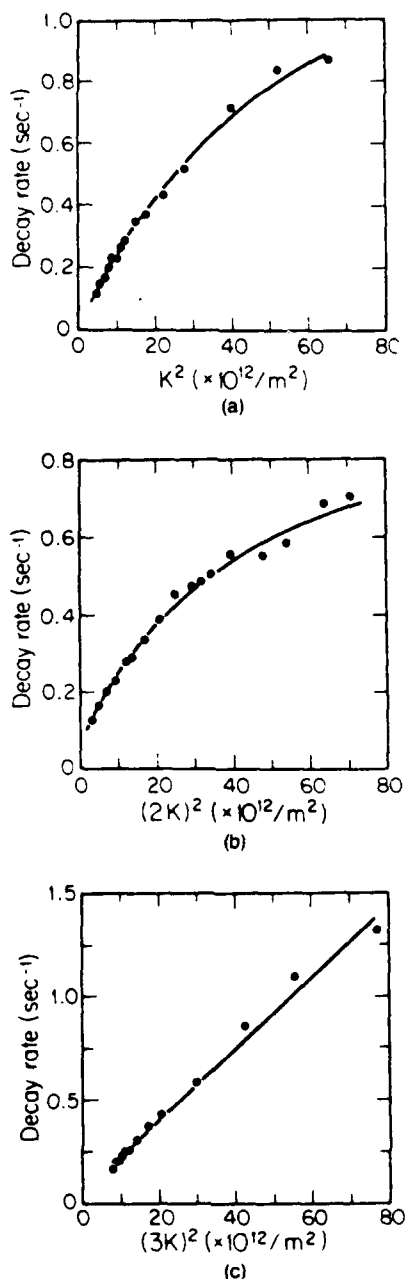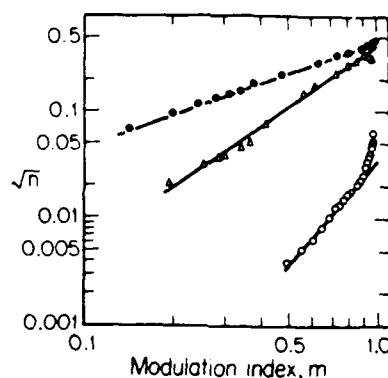

Fig. 4. Square root of the diffraction efficiency plotted versus the modulation index m for the three orders of anisotropic diffraction in $BaTiO_3$. The first, second, and third orders are plotted as filled circles, open triangles, and open circles, respectively. The solid curves are the theoretical fits to the linear regions.

ments were conducted on the $BaTiO_3$ crystal. The decay rates of the three orders were measured as a function of grating vector and were fitted to Eqs. (21), (27), and (30) by using a nonlinear least-squares-fitting routine. The writing-beam intensities were I_1 = 0.2 mW/cm^2 and I_2 = 31 mW/cm^2 for the first order, I_1 = 7.3 mW/cm^2 and I_2 = 21 mW/cm^2 for the second order, and I_1 = 19 mW/cm^2 and I_2 = 34 mW/cm^2 for the third order. Because grating decay rates in $BaTiO_3$ usually exhibit a nonlinear intensity dependence, the erase-beam intensity was held constant throughout the experiments at 11.5 mW/cm^2 for the first order, 4.5 mW/cm^2 for the second order, and 4 mW/cm^2 for the third order. The readout-beam intensity I_R was kept below 1 μW/cm^2 in all experiments.

The results of the light-induced grating-erasure-versus-grating-vector experiments are shown in Fig. 3. A nonlinear dependence of the decay rate on the square of the grating vector was observed for anisotropic diffraction into the first and second orders. The theoretical fit of Eqs. (21), (27), and (30) to the data is also plotted as solid lines in Fig. 3. This gives effective trap densities, N_T, of (1.5 ± 0.6) × 10^{16}/cm^3, (0.65 ± 0.7) × 10^{16}/cm^3, and (2.1 ± 0.4) × 10^{16}/cm^3 from the first-, second-, and third-order data, respectively. Taking the uncertainties into account, we find that these values are in fair agreement.

The diffraction efficiency was also measured as a function of the modulation index for each order. In this experiment one of the writing-beam intensities was kept constant at 27 mW/cm^2 and the intensity of the other varied. The square root of the diffraction efficiency is plotted versus m in Fig. 4 for the three orders. In this model the square root of the diffraction efficiency is linearly proportional to the space-charge field in the absence of beam coupling and for low diffraction efficiencies [Eq. (9)]. Fitting our data for the three orders to this equation, we find the values of M in m^M to be 1, 1.9, and 3.2 for the first, second, and third orders, respectively. We see that the theoretical fit (solid line in the figures) is in good agreement with the measured efficiencies for the first two orders with a reasonable fit for the third order at small m.

This result is in contrast to the results of Huignard and Ledu[14] for $Bi_{12}SiO_{20}$. They found that the diffraction efficiencies of the different orders followed the equation

Fig. 3. Decay rates of the first three diffraction orders as a function of grating vector for a $BaTiO_3$ crystal. (a) The first order is plotted versus K^2, (b) the second order is plotted versus $(2K)^2$, and (c) the third order is plotted versus $(3K)^2$. The filled circles are the data points, and the solid curves are the theoretical fit.

$$E_M \propto \left[\frac{1 - (1 - m^2)^{1/2}}{m} \right]^M. \tag{31}$$

We find that our data do not fit this equation for large m.

4. ANISOTROPIC SELF-DIFFRACTION

Anisotropic self-diffraction occurs when the phase-matching conditions are satisfied for the writing beams. The configuration that we used to study anisotropic self-diffraction is shown in Fig. 5. Here, two extraordinary polarized writing beams, A_1 and A_2, of wave vector k_1 and k_2 intersect in the x–y plane of a 4-mm crystal to form an anisotropic grating of wave vector $K = k_1 - k_2$. For plane-wave light fields of the form

$$A(r, t) = \hat{e}A(r) \exp[i(k \cdot r - \omega t)] + c.c., \tag{32}$$

using the slowly varying field approximation we can derive the following coupled-wave equations governing self-diffraction:

$$-2ik_4 \cos(\theta_{in}) \frac{\partial A_1}{\partial y} = \kappa_1^* A_3 + \kappa_4 A_4, \tag{33}$$

$$-2ik_2 \cos(\theta_{in}) \frac{\partial A_2}{\partial y} = \kappa_3 A_4 + \kappa_2^* A_3, \tag{34}$$

$$-2ik_3 \cos(\psi_{in}) \frac{\partial A_3}{\partial y} = \kappa_1 A_1 + \kappa_2 A_2, \tag{35}$$

$$-2ik_4 \cos(\psi_{in}) \frac{\partial A_4}{\partial y} = \kappa_3^* A_2 + \kappa_4^* A_4. \tag{36}$$

Here θ_{in} and ψ_{in} are the angles of the writing and diffracted beams, respectively, inside the crystal. The coupling constants are given by

$$\kappa_1 = \epsilon_0 \frac{\omega^2}{c^2} \hat{e}_3 \cdot \tilde{\chi}_1 \cdot \hat{e}_1, \tag{37}$$

$$\kappa_2 = \epsilon_0 \frac{\omega^2}{c^2} \hat{e}_3 \cdot \tilde{\chi}_2 \cdot \hat{e}_2, \tag{38}$$

$$\kappa_3^* = \epsilon_0 \frac{\omega^2}{c^2} \hat{e}_4 \cdot \tilde{\chi}_1^* \cdot \hat{e}_2, \tag{39}$$

$$\kappa_4^* = \epsilon_0 \frac{\omega^2}{c^2} \hat{e}_4 \cdot \tilde{\chi}_2^* \cdot \hat{e}_1, \tag{40}$$
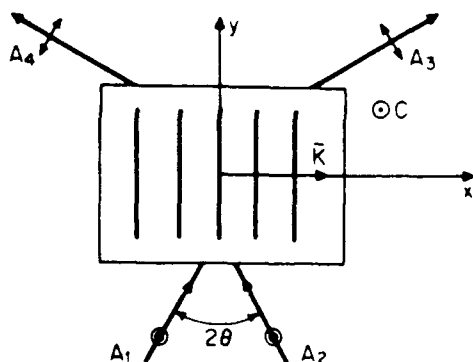
with

Fig. 5. Setup for observing anisotropic self-diffraction in photorefractive crystals. The angle θ is the phase-matching angle defined in Eq. (43).
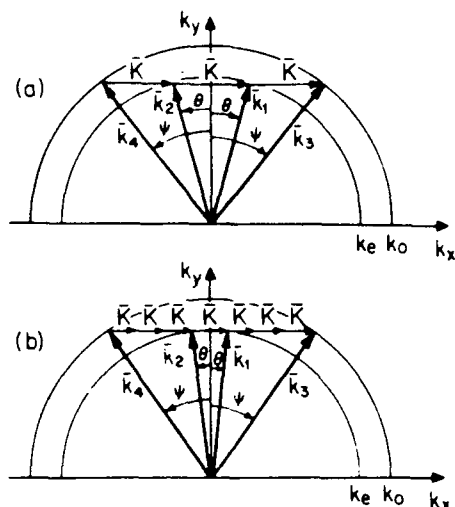

Fig. 6. Phase-matching diagrams showing examples of anisotropic self-diffraction of extraordinary polarized beams into ordinary polarized (a) first and second orders and (b) third and fourth orders.

Table 1. Phase-Matching Angles of the Writing Beams Outside the Crystal for High-Order Anisotropic Self-Diffraction

Orders	BaTiO$_3$	SBN	BSKNN
First and second[a]	12	8.5	10.2
Second and third	6.9	4.9	6.2
Third and fourth	4.9	3.5	4.2
Fourth and fifth	—	—	3.4

[a] Measured values.

$$\tilde{\chi}_1 = -\tilde{e} \cdot \tilde{\tilde{R}} \cdot E_M \cdot \tilde{e}, \tag{41}$$

$$\tilde{\chi}_2 = -\tilde{e} \cdot \tilde{\tilde{R}} \cdot E_{M+1} \cdot \tilde{e}, \tag{42}$$

where E_M and E_{M+1} are the M- and $M + 1$-order space-charge fields, ϵ_0 is the free-space permittivity, and c is the free-space speed of light. We also see that although the writing beams A_1 and A_2 do not experience self-diffraction into each other, they are indirectly coupled because E_M is proportional to $(I_1 I_2)^{M/2}$.

The anisotropic self-diffraction phase-matching diagram is shown in Fig. 6(a). Close examination of this figure clearly shows that each diffracted beam is composed of two orders. For instance, beam A_3 is the result of self-diffraction of beam A_1 into first order ($k_3 = k_1 + K$) and beam A_2 into second order ($k_3 = k_2 + 2K$). This can be observed experimentally simply by blocking beam A_1 or A_2 and noting the presence of the diffracted beam A_3. Thus a measure of the rise or decay rate of these diffracted beams involves more than one time constant. Because the diffraction intensity of the orders goes as m^{2M}, where m is the modulation index and M is the order of the diffracted beam, the departure from a single time constant should be significant only for large m gratings.

Figure 6(b) shows typical phase-matching conditions required to observe anisotropic self-diffraction into orders higher than the second order. In the particular case shown the diffracted beams are composed of both third and fourth orders ($k_3 = k_1 + 3K = k_2 + 4K$). In general, anisotropic self-diffraction occurs in pairs of order $-M$ and $M + 1$. The

phase-matching conditions can be expressed mathematically by

$$\sin(\theta) = \left[\frac{n_{\cdot}^2 - n_{r}^2}{(2M+1)^2 - 1} \right]^{1/2}, \tag{43}$$

$$\sin(\psi) = (2M+1)\left[\frac{n_{\cdot}^2 - n_{r}^2}{(2M+1)^2 - 1} \right]^{1/2}, \tag{44}$$

where θ and ψ are the angles outside the crystal of the writing and diffracted beams, respectively. If the high-order space-charge fields are neglected, Eqs. (33)–(36) and (43) and (44) reduce to those of Kukhtarev et al.[2]

High-order self-diffraction experiments were performed on the crystals using a Coherent Innova 70 argon-ion laser, with $\lambda = 488$ Å, operating in the TEM$_{00}$ mode. The beams were roughly collimated to approximately 5 mm in diameter with an intensity ratio $I_1/I_2 = 3$.

First, the angles for anisotropic self-diffraction into first and second orders ($M = 1$), as in Fig. 6(a), were measured for each sample. These were $\theta = 12°$, $8.5°$, and $10.8°$ for the BaTiO$_3$, SBN, and BSKNN crystals, respectively. From Eq. (43) these values of θ imply that $n_o^2 - n_r^2 = 0.346$ for BaTiO$_3$, 0.1734 for SBN, and 0.281 for BSKNN. Using these values of $n_o^2 - n_r^2$ in Eq. (43), we calculated the angles of the writing beams needed to observe the higher orders. These are shown in Table 1. Note that up to the fifth order was observed in BSKNN. The measured angles were all within the experimental error, $\pm 0.1°$ of the calculated values.

5. SUMMARY

In conclusion, we have observed high-order anisotropic self-diffraction in BaTiO$_3$, SBN, and BSKNN. The phase-matching angles were measured and found to be in excellent agreement with the theory. Also, it was shown that the beams that are diffracted through anisotropic self-diffraction are composed of two distinct orders. To model high-order anisotropic diffraction, we included high-order terms in Kukhtarev's solution of the transport equations. The light-induced decay rates versus grating vector squared and the diffraction efficiencies versus modulation index were measured for the first three orders in BaTiO$_3$ and were found to be in fair agreement with the model.

ACKNOWLEDGMENTS

REFERENCES

1. S. I. Stepanov, M. P. Petrov, and A. A. Kashilin, "Optical diffraction with polarization-plane rotation in a volume hologram in an electrooptic crystal," Sov. Tech. Phys. Lett. 3, 345 (1977).
2. N. V. Kukhtarev, E. Kratzig, H. C. Kulich, and R. A. Rupp, "Anisotropic self-diffraction in BaTiO$_3$," Appl. Phys. B 35, 17 (1984).
3. R. A. Rupp and F. W. Drees, "Light-induced scattering in photorefractive crystals," Appl. Phys. B 39, 223 (1986).
4. E. Voit, C. Zaldo, and P. Gunter, "Optically induced variable light deflection by anisotropic diffraction in photorefractive KNbO$_3$," Opt. Lett. 11, 309 (1986).
5. E. Voit and P. Gunter, "Photorefractive spatial light modulation by anisotropic self-diffraction in KNbNO$_3$ Crystals," Opt. Lett. 12, 10 (1987).
6. N. V. Kuktharev and S. G. Odulov, "Wave front inversion in anisotropic self-diffraction of laser beams," Sov. Tech. Phys. Lett. 6, 503 (1980).
7. N. V. Kuktharev, "Wavefront reversal of optical beams in an anisotropic media," Sov. J. Quantum Electron. 11, 878 (1981).
8. D. A. Temple and C. Warde, "Amplified reflection through anisotropic four-wave mixing in BaTiO$_3$," submitted to Opt. Lett.
9. D. A. Temple and C. Warde, "Anisotropic scattering in photorefractive crystals," J. Opt. Soc. Am. B 3, 337 (1986).
10. P. Refregier, L. Solymar, H. Rajbenbach, and J. Huignard, "Beam coupling in photorefractive Bi$_{12}$SiO$_{20}$ crystals with moving gratings. Theory and experiments," J. Appl. Phys. 58, 949 (1985).
11. N. V. Kukhtarev, V. B. Markov, S. G. Odulov, M. S. Soskin, and V. L. Vineteskii, "Holographic storage in electrooptic crystals I. Steady state," Ferroelectrics 22, 949 (1979).
12. J. Feinberg, D. Heiman, A. R. Tanguay, Jr., and R. W. Hellwarth, "Photorefractive effects and light induced charge migration in barium titanate," J. Appl. Phys. 51, 1297 (1980).
13. H. Kogelnik, "Coupled wave theory for thick hologram gratings," Bell Syst. Tech. J. 48, 2909 (1969).
14. J. P. Huignard and B. Ledu, "Collinear Bragg diffraction in photorefractive Bi$_{12}$SiO$_{20}$," Opt. Lett. 7, 310 (1982).

8 Amplified Reflection Through Anisotropic Four-Wave Mixing in BaTiO$_3$

Amplified reflection through anisotropic four-wave mixing in BaTiO₃

D. A. Temple

Department of Physics. Massachusetts Institute of Technology, Cambridge, Massachusetts 02139

J. Chang

Department of Material Science. Massachusetts Institute of Technology, Cambridge, Massachusetts 02139

C. Warde

Department of Electrical Engineering and Computer Science. Massachusetts Institute of Technology, Cambridge, Massachusetts 02139

We have demonstrated cw non-phase-conjugate amplified reflection in single-crystal BaTiO₃ using anisotropic four-wave mixing. We show that the reflected beam is polarized orthogonally to the readout beam and that it is a true reflection of the image beam, not a phase conjugate. The maximum reflectivity measured was approximately 200%.

Amplified reflection has been observed previously in BaTiO₃ using isotropic four-wave mixing.[1-3] In the normal configuration shown in Fig. 1(a), the object A_1 and pump A_2 beams intersect in the crystal to form a photorefractive grating. A second pump beam A_3 counterpropagating with the first pump beam scatters from this grating into a fourth beam A_4, which has the same polarization as the pump beam A_3 and is the phase conjugate of the object beam A_1. In BaTiO₃ the phase-conjugate reflectivity has been found to exceed 100%.[1]

The configuration for observing amplified reflection through anisotropic four-wave mixing in BaTiO₃ is shown in Fig. 1(b). As seen from the phase-matching diagram (Fig. 2), it is a simple variation of the configuration used for observing anisotropic self-diffraction.[4-6] In this system, two coherent ordinary-polarized plane waves A_1 and A_2 with wave vectors k_1 and k_2 intersect in the x–y plane of the crystal, producing an anisotropic grating through the photorefractive effect. An ordinary-polarized plane wave A_3 of wave vector k_3 is used to read out the grating, as in Fig. 2, producing an extraordinary-polarized wave A_4 of wave vector k_4. Unlike the normal phase-conjugate reflection shown in Fig. 1(a), the unique features of this system are (1) the readout beam is always ordinary polarized and the reflected beam is always extraordinary polarized, (2) ordinary-polarized writing beams cannot couple to the grating, which eliminates beam-coupling effects,[6] (3) the reflected beam is a real reflection of the image beam A_1, not a phase conjugate, and (4) anisotropic diffraction in BaTiO₃ makes use of the r_{13} electro-optic coefficient exclusively. The major disadvantages of this mirror are that strict phase-matching conditions must be met in order to achieve maximum efficiency and phase-conjugate reflection is not possible in this configuration.

To model this mirror, consider the three ordinary-polarized plane waves A_1, A_2, and A_3 intersecting in the x–y plane of a photorefractive crystal as in Fig. 1(b). Although there are three gratings formed by interference between beams A_1 and A_2, A_1 and A_3, and A_2 and A_3, the ordinary-polarized writing beams A_1 and A_2 are not properly phase matched to couple to any of these gratings.[6] Hence, the only allowed coupling is diffraction of the readout beam A_3 into beam A_4. Therefore we only need to consider the grating produced by interference between beams A_1 and A_2, where $K = k_2 - k_1$. Now, by using the slowly varying field approximation,[7,8] we can derive the coupled-wave equations for this process. For plane waves of the form

$$E(r, t) = A(r)\exp[i(k \cdot r - \omega t)] + c.c.,\qquad(1)$$

the coupled equations are

$$\frac{dA_3}{dy} = i\kappa_3\left(\frac{A_2^* A_1}{I_0}\right)A_4 \exp(i\phi).\qquad(2)$$

$$\frac{dA_4}{dy} = i\kappa_4\left(\frac{A_2^* A_1}{I_0}\right)A_3 \exp(i\phi).\qquad(3)$$

The coupling coefficients are given by

$$\kappa_3 = \frac{\pi^2(\hat{e}_2{}^* \cdot \hat{e}_1)(\hat{e}_3 \cdot \bar{\chi}_{eff} \cdot \hat{e}_4)}{n_e\lambda^2 \cos(\theta)},\qquad(4)$$

$$\kappa_4 = \frac{\pi^2(\hat{e}_2{}^* \cdot \hat{e}_1)(\hat{e}_4 \cdot \bar{\chi}_{eff} \cdot \hat{e}_3)}{n_o\lambda^2 \cos(\phi)},\qquad(5)$$

where A and ω are the wave vector and frequency of the beams, respectively, $I_0 = I_1 + I_2$, $\hat{e}_1$, $\hat{e}_2$, $\hat{e}_3$, and $\hat{e}_4$ are the polarization vectors, λ is the wavelength, θ and
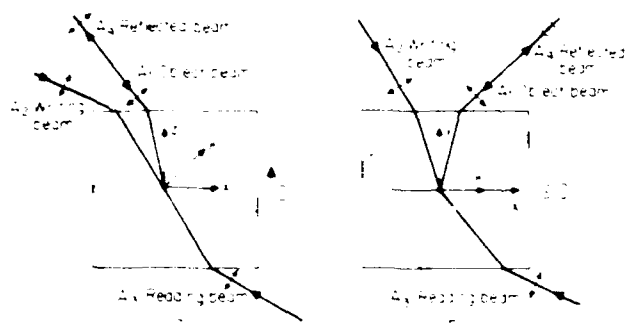
Fig. 1. Configurations for observing (a) normal four-wave mixing and (b) anisotropic four-wave mixing. In both cases beams A and A_z write a photorefractive grating. This grating is read out by beam A, which scatters into beam A_z.
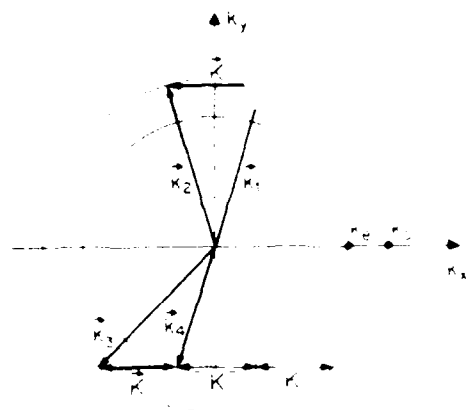

Fig. 2. Phase-matching diagram for observing anisotropic four-wave mixing in a negative birefringent photorefractive crystal.

ψ are the angles of the writing and readout beams. ϕ is the phase between the intensity fringes and the index-grating planes, and n and n_e are the ordinary and extraordinary indices of refraction. The effective susceptibility is given by

$$\tilde{\chi}_{\mathrm{eff}} = -\tilde{\epsilon} \cdot (\bar{r} \cdot \mathbf{E}_{sc}) \cdot \tilde{\epsilon},\qquad (6)$$

where $\tilde{\epsilon}$ is the second-rank optical dielectric constant. $\bar{r}$ is the third-rank electro-optic coefficient. and $\mathbf{E}_{sc}$ is the space-charge field. From Eqs. (2) and (3) we see that the reflected beam is a standard reflection of the image beam. $A_4 \propto A_1$, propagating back along the direction of the image beam. $\mathbf{k}_4 = -\mathbf{k}_1$. Thus, the crystal acts as if it were a standard mirror with its surface normal parallel to $\mathbf{k}_4$. This is similar to the phase-conjugation case except that the reflection is a standard reflection. When the beam ratios are such that $I_2, I_3 \gg I_1$, the reflectivity R can be approximated by

$$R = \left|\frac{A_4(d)}{A_1(0)}\right|^2 = \left(\frac{r_z E_{sc} l\pi}{\lambda}\right)^2 n_o n_e \left[\frac{\sin(\psi)\cos(2\theta)}{\cos(\theta)\cos(\psi)}\right]$$
$$\times \left[\frac{(I_2 I_3)}{(1 + I_2 I_3)^2}\right]. \qquad (7)$$

where l is the interaction length of the readout beam

I_1. Since the angles are fixed owing to the phase-matching conditions, this relation shows that the reflectivity can only be maximized by optimizing the beam overlap, a severe limitation for this system. For small modulation ($m \ll 1$) the space-charge field E_{sc} can be approximated by[8]

$$E_{sc} = \frac{(kT/e)K}{1 + (\epsilon kT/e^2 N_T)K^2}. \qquad (8)$$

where e is the charge on an electron, ϵ is the dielectric constant. k is the Boltzmann constant. T is the temperature. $K = (4\pi/\lambda)\sin\theta$ is the magnitude of the grating vector, and N_T is the trap density. Using a trap density of $1.5 \times 10^{16}\ cm^{-3}$, which was determined previously, values for the refractive index and dielectric constant determined by Wemple et al.,[10] $r_{42} = 820$ m/V (Ref. 11), and an interaction length of approximately 4 mm in Eq. (7), we estimate the maximum reflectivity to be approximately 400%. This is in reasonable agreement with the maximum reflectivity that we were able to attain, which was 200%. The difference is probably due to our estimate of the interaction length l or to the fact that Eq. (6) neglects reflections at the crystal surface.

Extraordinary-polarized writing beams can also be used to write the gratings. However, in this case the process is greatly complicated by self-diffraction of each writing beam into both a first and second order.[6] Qualitatively we expect this to cause the grating planes to vary in the crystal owing to the large variation of the writing-beam phases and intensities, as each is diffracted into the two orders. This should have the effect of reducing the grating strength and therefore the reflectivity. For this case, we measured a reflectivity of approximately 30% for the same writing- and readout-beam intensities.
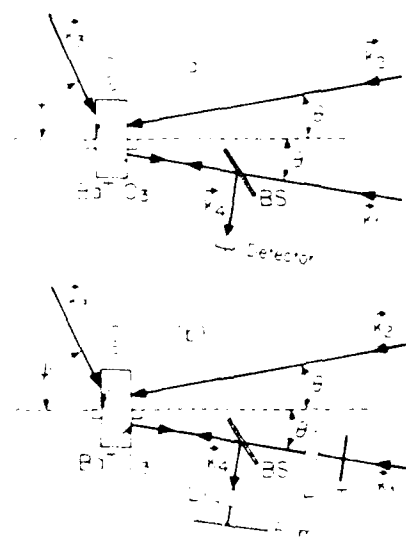

Fig. 3. Optical setups used to study anisotropic four-wave mixing. In setup (a), all the waves are collimated and the reflectivity was measured as a function of the pump-beam ratio. Setup (b) was used to demonstrate mirror action using a resolution chart as the transparency T. The angles were $\psi_1 = \psi_2 = 12.5°$ and $\psi = 40°$. Lenses shown have different focal lengths.
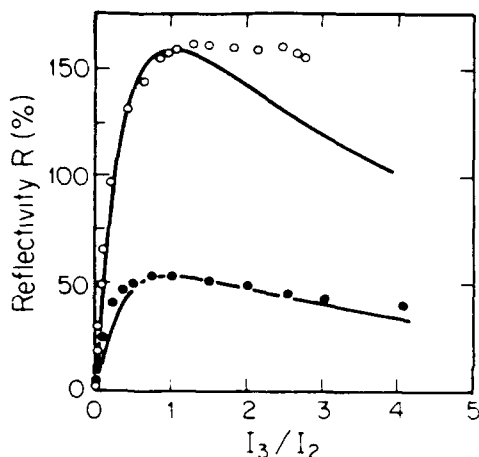
Fig. 4. Graph of the mirror reflectivity as a function of the pump-beam ratio I_3/I_2. The intensities of the writing beams I_1 and I_2 were kept constant, with the filled circles representing $I_1 = 850 \mu W$ and $I_2 = 3.4$ mW and the open circles representing $I_1 = 100 \mu W$ and $I_2 = 20$ mW.
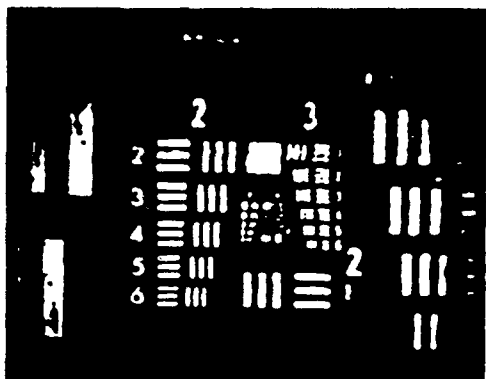

Fig. 5. Photograph of the object after anisotropic reflection.

The systems used for studying amplified reflection through anisotropic four-wave mixing are shown in Fig. 3. All the beams originated from an argon-ion laser operating at 488 nm in the TEM$_{00}$ mode. For the configuration in Fig. 3(a), the reflectivity I_4/I_1 was measured as a function of the readout-pump-beam intensity I_3. The writing-beam intensities were held constant, and all the beams were collimated in an effort to approximate the theory.[1,2] The results of these measurements are plotted in Fig. 4, with the filled circles representing $I_1 = 850 \mu W$ and $I_2 = 3.4$ mW and the open circles representing $I_1 = 100 \mu W$ and $I_2 = 20$ mW. The lines are the theoretical fits to Eq. (7). As shown, the reflectivity was found to be a fairly good fit to the model in the region of undepleted pumps.

The reflecting properties of this mirror were investigated by using the system shown in Fig. 3(b). Here,

the object beam I_1 was expanded and recollimated, and a resolution chart placed in the path was imaged with a lens L (focal length 38 cm) through a beam splitter BS onto the crystal. The crystal was slightly rotated to avoid overlap of the surface reflection of A_2 with the anisotropic reflected image A_4. A photograph of an amplified reflected image is shown in Fig. 5. The lens in front of the film was used for reimaging and magnification; its focal length was much different from that in front of transparency T. Three separate observations confirmed the reflecting properties of this mirror: (1) when an aberrator was placed in the path of beam 1 between the beam splitter and the crystal the reflected image at the screen was greatly distorted; (2) when transparency T was removed and the lens of focal length $f = 38$ cm placed 22 cm in front of the crystal, the reflected beam was found to focus at a distance 16 cm in front of the crystal and the transmitted beam was found to focus at a distance 16 cm behind the crystal; and (3) when a conventional mirror was used in place of the crystal the position of the focal point was unchanged.

In summary, we have demonstrated non-phase-conjugate amplified reflection using anisotropic four-wave mixing in photorefractive $BaTiO_3$. The reflected beam was shown to be a true reflection of the image beam, with a measured amplification of approximately 200%. This has potential for improving the signal-to-noise ratio of image amplification without producing a phase-conjugate image[12] or contrast reversal.[13]

References

1. J. Feinberg and R. W. Hellwarth, Opt. Lett. **5**, 519 (1980).
2. J. Feinberg, D. Heiman, A. R. Tanguay, Jr., and R. W. Hellwarth, J. Appl. Phys. **51**, 1297 (1980).
3. B. Fischer, M. Cronin-Golomb, J. White, and A. Yariv, Opt. Lett. **6**, 519 (1981).
4. N. V. Kukhtarev and S. G. Odulov, Sov. Tech. Phys. Lett. **6**, 503 (1980).
5. R. A. Rupp and F. W. Drees, Appl. Phys. B **39**, 223 (1986).
6. D. A. Temple and C. Warde, J. Opt. Soc. Am. B **3**, 337 (1986).
7. R. Hellwarth, J. Opt. Soc. Am. **67**, 1 (1977).
8. A. Yariv and D. Pepper, Opt. Lett. **1**, 16 (1977).
9. N. V. Kukhtarev, V. B. Markov, S. G. Odulov, M. S. Soskin, and V. L. Vinetskii, Ferroelectrics **22**, 949 (1979).
10. S. H. Wemple, M. DiDomenico, Jr., and I. Camlibel, J. Phys. Chem. Solids **29**, 1797 (1968).
11. A. Yariv, *Quantum Electronics*, 2nd ed. (Wiley, New York, 1975).
12. S. I. Stepanov and M. P. Petrov, Opt. Commun. **53**, 64 (1985).
13. A. Partovi, E. M. Garmire, and L. Cheng, Appl. Phys. Lett. **51**, 299 (1987).

9 Photorefractive Properties of BaTiO$_3$: Cr

Photorefractive Properties of BaTiO$_3$:Cr

R. S. HATHCOCK, D. A. TEMPLE, AND C. WARDE, MEMBER, IEEE

Abstract—Unusual beam fanning has been observed in heavily doped BaTiO$_3$:Cr along with an increased photovoltaic effect. The nature and symmetry of this beam fanning are described, and the results of the photovoltaic measurements are presented.

INTRODUCTION

BARIUM TITANATE (BaTiO$_3$) is a photorefractive material with large electrooptic coefficients. Beam fanning has been observed in nominally "undoped" samples of the material, and this phenomena is believed to be important in the process that is responsible for the excellent self-pumped phase conjugating property of the crystal [1]-[3].

Although models of the photorefractive effect have existed since the early work of Chen [4]-[6], the details of the effect in BaTiO$_3$ (i.e., the excitation and trapping centers), and the exact nature of beam fanning have not yet been firmly established. Recent papers have pointed to iron as the cause of the photorefractive effect in BaTiO$_3$ [7], but as we shall see herein it is not the only dopant that can alter the photorefractive properties of the material. In this paper, we discuss some of the properties of BaTiO$_3$ doped with chromium.

SAMPLE PREPARATION

A BaTiO$_3$ boule was grown by the top seeded solution method [8] with 20 ppm chromium in the melt. A sample was cut from the boule, polished, and electrically poled to yield a crystal with final dimensions of 6.7 × 5.6 × 3.6 mm. An undoped sample grown from a nominally pure melt with dimensions 4.1 × 4.9 × 4.1 mm was used for comparison.

DIFFRACTION EFFICIENCY

Attempts were made to measure the rise time and saturation level of the diffraction efficiency of the BaTiO$_3$:Cr sample by writing a grating with an Ar-ion laser (wavelength 488 nm) and reading the grating with a HeNe laser (wavelength 632.8 nm). These attempts were frustrated by the observation that the diffracted intensity did not rise to a steady-state value as was the case for the nominally pure sample. Instead, the diffracted beam intensity initially rose, but then decayed toward zero, as shown in Fig. 1.
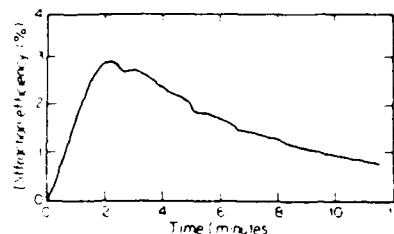
Fig. 1. Diffraction efficiency as a function of time for a BaTiO$_3$:Cr crystal. The writing beams were on continuously from $t = 0$.

Observation of the crystal during the writing process revealed that light from the writing beams was being scattered out of the crystal along well-defined paths (beam fanning). This scattered light became noticeable at approximately the same time that the intensity of the diffracted HeNe laser beam began decaying, and the rise in intensity of the scattered light continued to correlate with the further decay in the intensity of the diffracted beam. Clearly, while some beam fanning is essential for self-pumped phase conjugation, strong beam fanning can be detrimental since it may affect or limit the diffraction efficiency as illustrated in Fig. 1.

BEAM FANNING

Beam fanning in the Cr doped BaTiO$_3$ crystal was studied using a collimated (2 mm diameter) Ar-ion laser beam, with a wavelength of 488 nm. Three cases of beam fanning for a single pump beam initially incident along one of the high symmetry axes of the crystal are discussed below: 1) initial propagation antiparallel to the c axis, 2) initial propagation parallel to the c axis, and 3) initial propagation parallel to an a axis. The c axis was found optically using the crossed polarizer technique, and the $+c$ axis was determined by observing the voltage developed across the c axis when the crystal was heated. The face which becomes negative upon heating the crystal in the dark is the $+c$ face.

The most striking beam fanning was observed for the case of the incident beam propagating antiparallel to the c axis of the crystal. Initially the beam propagated through the crystal, but after a short time two distinct beam paths were observed within the crystal diverging from the incident beam. Fig. 2(a) is a photograph of the crystal illustrating this phenomenon. The fanning beams are observable through light scattered from crystal imperfections. At steady state, most of the incident power was diverted into these two paths. The two paths were always observed to lie in the plane of polarization of the
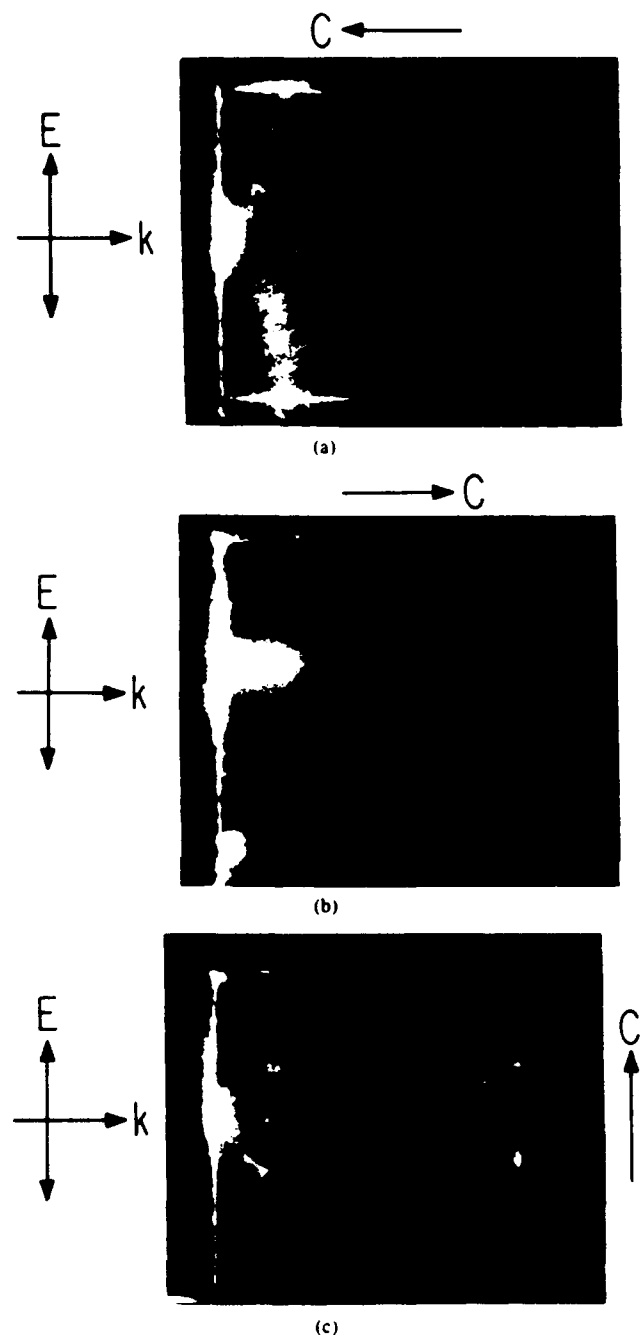
C ←———

E

———→ k

(a)

———→ C

E

———→ k

(b)

E

C

———→ k

(c)

Fig 2 Beam fanning in a BaTiO, Cr crystal (a) Beam propagating antiparallel to the *c* axis (b) Beam propagating parallel to the *c* axis (c) Beam propagating parallel to the *a* axis

incident light, and diverged from the path of the incident beam close to the entrant surface. The two beams did not remain collimated within the crystal. The fanning beams diverged within a range of angles between approximately 55 and 80° from the propagation direction of the incident beam.

For the case of the incident pump beam propagating in the direction of the +*c* axis, no fanning beams were observed inside the crystal. The incident beam, however, was strongly attenuated as it propagated into the crystal

[see Fig. 2(b)] and two strong backscattered beams were observed outside the crystal. These backscattered beams had properties similar to the fanning beams discussed above: 1) the build-up time is approximately the same, 2) the two backscattered beams lie in the plane of polarization of the incident beam, and 3) the backscattered beams do not remain collimated. Fig. 2(b) shows the beam path within the crystal for this configuration.

The final case is that of propagation along an *a* axis. Since the *a* axis is not polar, there is no distinction between antiparallel and parallel. When the polarization of the incident beam is along the *c* axis, as before, the incident beam initially propagates through the crystal. Then, as time progresses, a single fanning beam, which is directed toward the +*c* axis and lies in the plane formed by the *c* axis and the propagation direction, is observed. In steady state, most of the power is transferred to the fanning beam. Fig. 2(c) shows the trajectory of this single fanning beam inside the crystal. This is the same scattering geometry that gives rise to a pair of anisotropically scattered cones of transmitted light with nulls along the *c* axis in earlier work on undoped $BaTiO_3$ and $BaTiO_3 : Fe$. The apex half angles of the cones were 25.1° and 37.5° [9], [10]. When the polarization of the input beam is parallel to the other *a* axis the light is scattered at large angles (approaching 90°) to the incident beam direction. The scattering is out of the plane formed by the polarization and propagation vectors of the incident beam, and is toward the *c* axis. This case is more closely related to the configuration used in self-pumped phase-conjugate mirrors, and yields results similar to those previously observed by others in "undoped" crystals [1]-[3].

The general properties of the fanning beams did not vary with wavelength for the visible lines (514.5, 496.5, 488.0, and 476.5 nm) of the Ar-ion laser. Also the beam fanning pattern was found to be independent of the intensity of the incident beam except that at lower intensities, longer times were required in order to observe the fanning beams.

In order to determine whether the Gaussian intensity distribution of the laser beam influenced the beam fanning, several beamstop experiments were performed. Aperturing the beam to a smaller diameter decreased the width of the fanning beam, as expected. Blocking one-half of the beam in order to obtain a sharp intensity gradient caused a decrease in the intensity of the fanning beam on the blocked side, but the general shape and direction of the fanning beam remained the same as in the unblocked case. Finally, a beam stop was placed in the center of the Gaussian beam. Except for the reduced intensity, no change in the beam fanning was observed.

No fanning was observed for the red line of a HeNe laser. It is not clear whether this was due to the low power of the HeNe laser, the relatively low absorption of the crystal in the red, or a combination of both. The intensity of the HeNe laser beam was approximately 15 mW/cm^2, which is small compared with the intensity of the Ar-ion laser beam of approximately 500 mW/cm^2.

A photorefractive beam-coupling model in which the directional properties of the fanning beams are determined by the symmetry of the crystal (4 mm), the polarization of the incoming laser beam and the symmetry of the electrooptic tensor can be used to explain the case for input light propagation along the c axis. We assume that the beam fanning along preferred directions initiates from scattering off gratings established by interference between the input beam and randomly-scattered beams. The initial fanning beam itself then also suffers beam fanning, leading to beam trajectories inside the crystal which are determined by the polarization of the incident light, the sign of the dominant charge carriers, the symmetry and magnitude of the electrooptic tensor elements, and the refractive indexes of the crystal through a set of phase matching and beam coupling conditions

In cases 1) and 2) (propagation along the c axis), the optical properties of the crystal are isotropic about the incident beam. Thus beam fanning in these two cases must be invariant under a $180°$ rotation of the crystal about the incident beam. Since the fanning beams are started by random scattering and reaches a steady state, some sort of feedback mechanism is active. If beam coupling is the feedback mechanism, then the scattered beams of interest must have a polarization component parallel to that of the incident beam (this is required in order for the two beams to interfere). Assuming diffusion is the transport mechanism (no external fields were applied), the photorefractive grating vector will lie in the plane defined by the propagation vectors of the incident and scattered beams.

In order to show that the strongest fanning beams in the crystal must lie in the plane of polarization of the incident beam, we must examine the coupling due to the electrooptic effect. Let us define a coordinate system with the $+z$ axis in the direction of the c axis and the x and y axes along the equivalent a and b axes of the crystal. We will assume that the incident pump beam is propagating along the z axis and, without loss of generality, polarized along the x axis. The interference between a typical scattered beam and the incident beam will create a sinusoidal electric field with a grating vector which is the difference between the two propagation vectors. Through the electrooptic effect this creates a grating in the impermittivity. However, only those gratings which can couple energy from the pump to the scattered signal beam will be reinforced and build up to a steady-state strength.

It can be shown that the impermittivity tensor for this geometry has the form

$$K = \begin{bmatrix} K_0 & 0 & 0 \\ 0 & K_0 & 0 \\ 0 & 0 & K_e \end{bmatrix} + \begin{bmatrix} \Delta K_{11} & 0 & \Delta K_{13} \\ 0 & \Delta K_{22} & \Delta K_{23} \\ \Delta K_{13} & \Delta K_{23} & \Delta K_{33} \end{bmatrix} \tag{1}$$

From this form, it is seen that the x-polarized pump can transfer energy by beam coupling only to beams polarized in the xz plane. This means that only randomly-scattered beams polarized in the xz plane (extraordinary beams) will

be reinforced by energy diffracted out of the pump beam. By considering the propagation of light in anisotropic media, we see that such beams must either have their propagation vector in the xz plane or exactly along the y axis. Thus a pump beam incident along the c axis can generate a fanning beam which lies in the plane formed by this axis and the polarization vector of the pump beam, and the fanning beam will be polarized in this plane. This is precisely what was observed experimentally in Fig. 2(a). A second beam polarized parallel the polarization of the pump and propagating perpendicular to the plane defined by the polarization and propagation vectors of the pump is also permitted. This may partly explain the intense scattering of the pump beam observed just inside the crystal in Fig. 2(a) and (b).

ABSORPTION

Fig. 3 shows the absorption spectra of the Cr doped and undoped crystals. As can be seen, the addition of Cr has two major effects on the absorption: 1) the band edge is effectively moved toward lower energy, which gives the crystal its reddish color, and 2) the absorption becomes more anisotropic. There is little structure in the absorption curves except for a broad peak at about 600 nm in the c axis absorption. Without further data, it is not possible to assign the peak to Cr transitions.

PHOTOVOLTAIC EFFECT

Another significant characteristic of this heavily doped $BaTiO_3$:Cr crystal is the magnitude of its bulk photovoltaic effect. Bulk photovoltaic currents in noncentrosymmetric crystals, including $BaTiO_3$, have been observed by many researchers [11]–[13]. Phenomenological models of the photovoltaic effect have been presented by Glass [13] and Belinicher and Sturman [14]. Following the notation of Belinicher and Sturman, the current density $J_i^{(0)}$ is given by

$$J_i^{(0)} = \beta_{ijk} E_j^{(\omega)} E_k^{(-\omega)} \tag{2}$$

where β_{ijk} is the bulk photovoltaic tensor, and $E_j^{(\omega)}$ and $E_k^{(-\omega)}$ are components of the optical field of frequency ω. In $BaTiO_3$, the nonzero photovoltaic tensor elements are $\beta_{113} = \beta_{131} = \beta_{223} = \beta_{232} = \beta_{15}$, $\beta_{333} = \beta_{33}$, and $\beta_{311} = \beta_{322} = \beta_{31}$.

Fig. 4(a) schematically shows the arrangement used for measuring the bulk photovoltaic currents as a function of the angle θ between the optical polarization and the c axis. From (2), the current density along the c axis is given by

$$J_3^{(0)} = |E|^2 [\beta_{311} \sin^2 \theta + \beta_{333} \cos^2 \theta]. \tag{3}$$

Although allowed by (2), no measurable current was observed along the a axis for any value of θ. The measured c axis currents normalized by the light intensity are shown in Fig. 4(b). The solid line is a fit to the above functional form, and the inset shows that the current varies linearly with intensity.

Fig. 3 shows the absorption curves for both the Cr doped and undoped crystals. Because the absorption of
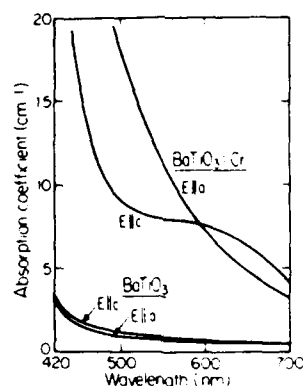
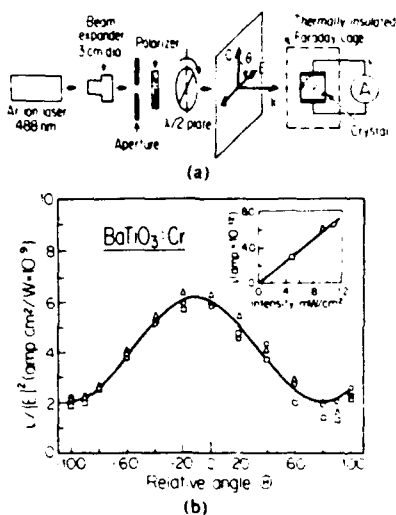Fig. 3. Polarization dependence of the absorption coefficient of nominally "undoped" BaTiO₃ and BaTiO₃:Cr crystals

Fig. 4. (a) Schematic diagram of the apparatus used to measure photovoltaic current (b) The c axis photovoltaic current normalized to intensity as a function of the angle between the polarization vector of the light and the c axis for a BaTiO₃ Cr crystal. The solid line is a numerical fit, and the inset shows the maximum current versus intensity

the doped crystal is not negligible, it must be included in the photovoltaic model. Since the current is linear with intensity, the equation for the current becomes

$$i_3 = |E|^2 W \int_0^L dl \left\{ B_{311} \sin^2 \theta \exp\left(-\alpha_1 l\right) \right. $$

$$\left. + B_{333} \cos^2 \theta \exp\left(-\alpha_3 l\right) \right\} \tag{4}$$

where W and L are the dimensions of the electrodes perpendicular to, and along the direction of propagation of the light beam, respectively, and α_1 and α_3 are the a or c axis absorption coefficients, respectively.

Using the parameters obtained by curve fitting the data, and the absorption of the crystal, the photovoltaic tensor coefficients at the 488 nm wavelength were found to be $\beta_{333} = 1.1 \times 10^{-7}$ and $\beta_{311} = 6.7 \times 10^{-8}$ A/W. These

values are an order of magnitude larger than those measured on the undoped crystal. Dividing β_{333} by the absorption at 488 nm gives a Glass constant k_1 of 1.2×10^{-8} A·cm/W which is an order of magnitude larger than that reported in LiNbO₃ [13].

SUMMARY

The increased absorption of the Cr doped BaTiO₃ crystal (whether it is due to Cr or some compensating defect) is probably the source of the increased photovoltaic activity. Unlike the case of LiNbO₃ [13], dividing the photovoltaic tensor elements for the Cr and undoped samples by the respective absorption coefficient of each sample did not yield the same Glass constant; however further research needs to be done on samples doped with varying amounts of Cr. Since the behavior of the beam fanning can be explained by a photorefractive beam coupling model, it seems likely that the increase in beam fanning is simply due to an increase in the two beam coupling coefficient which, in turn, is probably due to the high absorption of the Cr doped crystal. Unfortunately, standard beam coupling gain measurements could not be performed reliably due to strong beam fanning.

REFERENCES

[1] M. Cronin-Golomb, B. Fischer, J. O. White, and A. Yariv, Appl. Phys. Lett., vol 41, p. 689, 1982.
[2] J. Feinberg, Opt. Lett., vol. 7, p. 486, 1982.
[3] K. R. MacDonald and J. Feinberg, J. Opt. Soc. Amer., vol. 73, p. 548, 1983.
[4] F. S. Chen, J. Appl. Phys., vol. 40, p. 3389, 1969
[5] D. W. Vahey, J. Appl. Phys., vol. 46, p. 3310, 1975.
[6] N. V. Kukhtarev, V. B. Markov, S. G. Odulov, M. S. Soskin, and V. L. Vinetskii, Ferroelect., vol. 22, p. 949, 1979.
[7] M. B. Klein and R. N. Schwartz, J. Opt. Soc. Amer. B, vol. 3, p. 293, 1986.
[8] V. Belruss, J. Kalnajs, A. Linz, and R. C. Folweiler, Mat. Res. Bull., vol 6, p. 899, 1971
[9] D. A. Temple and C. Warde, J. Opt. Soc. Amer B, vol. 4, p. 1335, 1987
[10] ——, J. Opt. Soc. Amer B, vol. 3, p. 339, 1986
[11] M. L. Barsukova, B. Kh. Karimov, R. M. Magomadov, and V. M. Fridkin, Sov. Phys. Solid State, vol. 22, p. 1677, 1980
[12] W. H. T. Koch, R. Munser, W. Ruppel, and P. Wurfel, Ferroelect., vol 13, p. 305, 1976
[13] A. M. Glass, D. von der Linde, and T. J. Negran, Appl. Phys. Lett., vol 25, p. 233, 1974
[14] V. I. Belincher and B. I. Sturman, Sov. Phys. Usp., vol. 23, p. 199, 1980

R. S. Hathcock, photograph and biography not available at the time of publication.

D. A. Temple, photograph and biography not available at the time of publication.

C. Warde (M'76), photograph and biography not available at the time of publication.

10 Photoconductivity in Photorefractive SBN

Photoconductivity in Photorefractive SBN

R. S. Hathcock, D. A. Temple, and C. Warde
Departments of Materials Science, Physics, and Electrical Engineering and
Computer Science
Massachusetts Institute of Technology
Cambridge Massachusetts 02139

R. R. Neurgaonkar
Rockwell International Science Center, P.O. Box 1085
Thousand Oaks, California 91360

Czochralski grown SBN:Fe and SBN:Ce crystals have been studied by photoconductivity and temperature dependent conductivity in order to understand the nature of trapping centers in these materials.

INTRODUCTION

The tungsten bronze crystal $Sr_{0.6}Ba_{0.4}Nb_2O_6$ (SBN-60) is a photorefractive material that has recently been grown in large single crystals. SBN-60 has only one phase transition at 75 ^0C, the paraelectric-ferroelectric transition, and therefore is not damaged by cooling.[1] Also, since its tetragonal distortion is relatively large, compared with $BaTiO_3$, 90^0 domains are uncommon. However, like $BaTiO_3$, the origin of the photorefractive effect and the role of defects and impurities in the effect are unknown.

As part of a program to study the nature of dopants in SBN-60, Neurgaonkar et al.[2] have grown Ce and Fe doped SBN crystals. The sensitivity of Ce doped SBN is two orders of magnitude larger than the undoped material while the response time is reduced approximately one order of magnitude. In order to better understand the nature of the charge transport and trapping, these materials were investigated using photoconductivity and temperature-dependent conductivity techniques.

EXPERIMENTAL RESULTS

The experimental apparatus consists of a sample chamber, a Keithly 617 electrometer, an Ar-ion laser, and an AT&T personal computer. The sample chamber is a Faraday cage with an optical window, and it houses a teflon crystal holder. The Faraday cage is nessecary in order to reduce electrical noise, and teflon is used for the crystal holder as its resistivity is much greater than that of the crystal. The computer controls a shutter which exposes the crystal to the laser beam, and it records the current measured by the electrometer. The dark conductivity was measured as a function of temperature by heating the Faraday cage and monitoring the crystal temperature with a thermistor probe near the crystal.

Photoconductivity rise and decay curves were recorded over a range of intensities and for several lines of the Ar-ion laser. The rise and decay

times of the SBN:Ce were too short to be resolved by the electrometer so a storage oscilloscope was used to record the response of this crystal. In order to achieve sufficient signal, the intensity was set to the maximum availible from the laser. The photocurent response time (1/e point) was found to have a decay time of approximately 22 ms and a rise time of 18 ms. These response times are of the same order of magnitude as those observed in photorefractive studies of this material.[1]

The response of the SBN:Fe crystal was much slower. Figure 1. shows typical rise and decay curves for the SBN:Fe crystal for two different intensities at a wavelength of 488nm. These curves were fitted to a sum of exponentials.[3] The decay curves are best fit to a sum of three exponentials plus a constant dark current, while the rise curves are composed of the steady state current minus the sum of two exponentials. The steady state photocurrent as a function of intensity is shown in Fig 2. From this plot we find that the photocurrent is given by:

$$i_{ph} = 3.6*I^{0.58}$$

where i_{ph} is in nA and I is in mW/cm^2. The three time constants for the decay curves are:

$$\tau_1 = 0.5 \pm 0.2 \ sec$$

$$\tau_2 = 2.6 \pm 0.4 \ sec$$

$$\tau_3 = 18 \pm 9 \ sec$$

The largest time constant may be due to thermal decay. Since the decay time constants are expected to change with temperature and no attempt was made to control the temperature in the photoconductivity experiments, the uncertainty in the above time constant values was expected.

The time constants for the rise curves vary with intensity. Further experiments are being conducted in order to measure the time constants as a function of temperature, and such measurements should yield the depths of the traps. An Arrhenius plot [ln(i) vs 1/T] of the dark current for SBN:Fe is shown in Fig 3. This shows a trap depth of approximately 0.8 eV.

Photoconductivity studies indicate that SBN:Ce is significantly faster than SBN:Fe. Based on the observed multiple time constant decay data, the response time of SBN:Fe appears to be associated with several trapping levels or distributions of trapping levels.

REFERENCES

1. R. R Neurgaonkar and W. K. Cory, J. Opt. Soc. Am. B. 3, 274 (1986).

2. R. R Neurgaonkar, Semi-Arnual Tech. Rep. No. 4, Contract N0014-82-C-2466.

3. G. Golub and R. Leveque, Proc. 1979 Army Num. Anal. and Computers Conf., ARO Report 79-3, pp. 1.
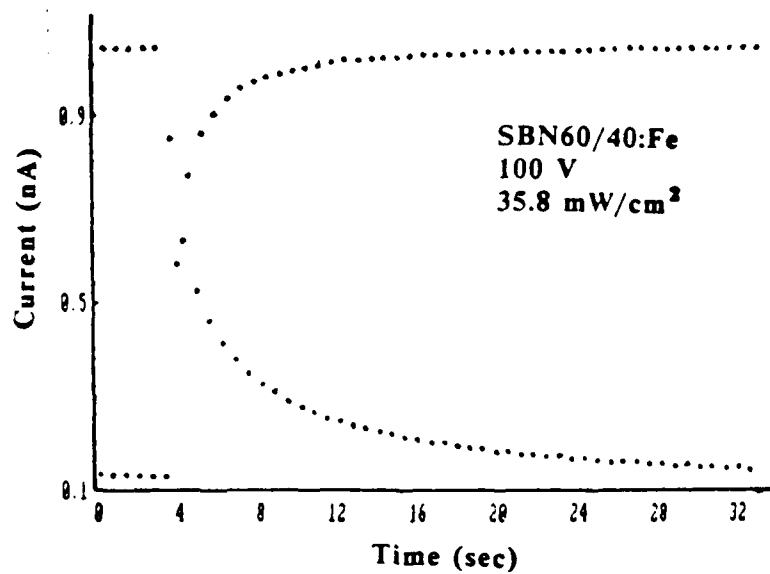
(a)
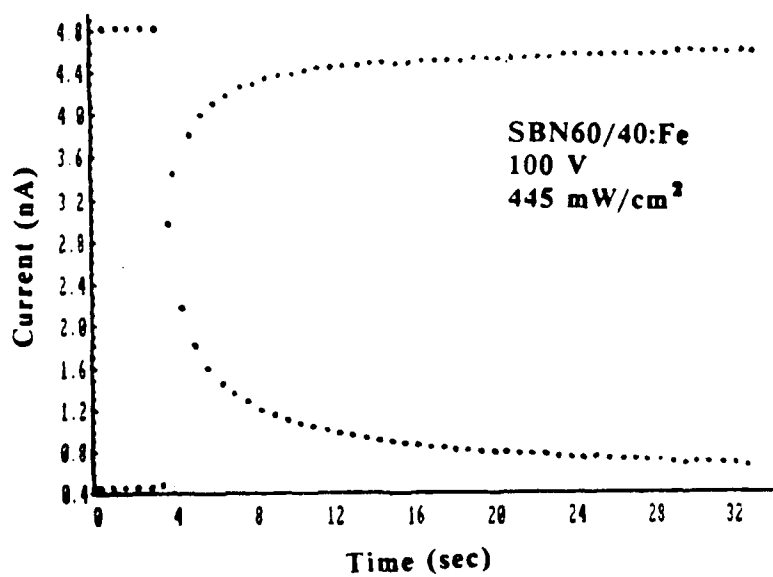
(b)

Fig. 1. Photocurrent rise and decay in SBN:Fe for laser
intensities: (a) 35.8 mW/cm^2; (b) 445 mW/cm^2

Fig. 2. Log of the saturation photocurrent vs log of the intensity in mW/cm^2
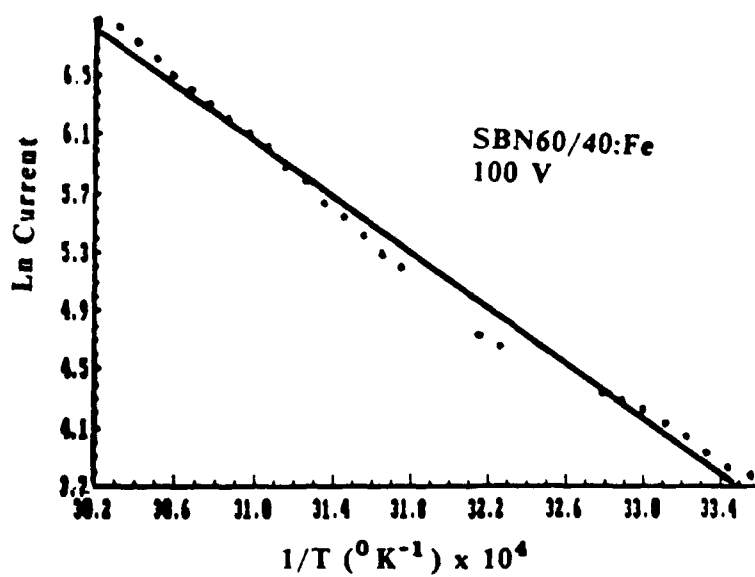
Fig. 3. Arrhenius plot of the dark current yielding an activation energy of 0.8 eV

78

11 Collaboration with Related Research Group

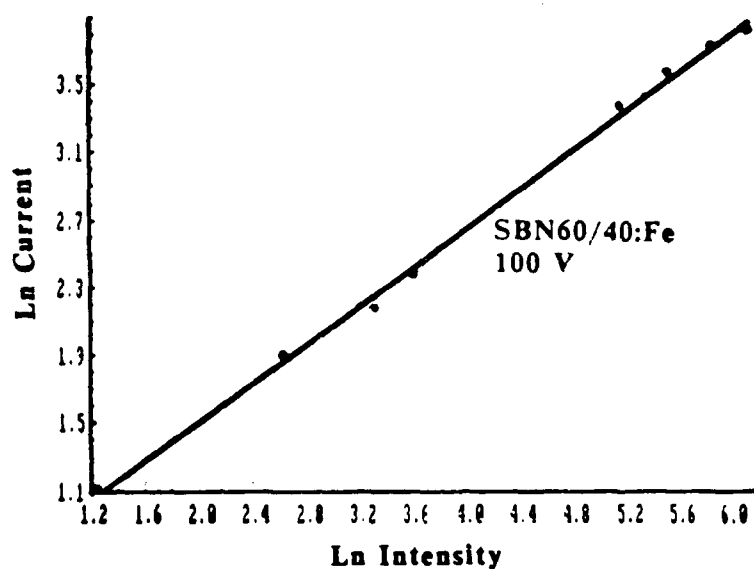Our collaboration with related research groups included :

1. An exchange of crystals ($BaTiO_3$ for SBN) with Dr. R. R. Neurgoankar of Rockwell. We jointly participated in the measurement of the photoconductivity in the SBN sample (see Section 10)

2. An exchange of crystals ($BaTiO_3$ for BSO) with Professor Armand Tanguay of the University of Southern california. We measured photoluminescence in the BSO samples.

3. Providing a $BaTiO_3$ crystal called "Doyle" to Professor Jack Feinberg of the University of Southern California.

4. Collaborating with and providing a $BaTiO_3$ crystal to and Dr. Charmaine Gilbreath of the Naval Research Laboratoiy for use in wavefront shaping of a diode laser for space communications.

5. Technical exchanges with personnel from Sanders Associates on the crystal growth of barium titanate.

12 Publication Resulting from DARPA/RADC Sponsorship

1. Temple, D. and C. Warde, "Anisotropic Scattering in Photorefractive Crystals," J. Opt. Soc. Am. B 3, 337-341, 1986.

2. Temple, D. and C. Warde, "Anisotropic Scattering in Photorefractive Crystals: Reply to Comments," J. Opt. Soc. Am. B4, 1335, August 1987.

3. Hathcock, R. S., D. A. Temple and C. Warde, "Photorefractive Properties of $BaTiO_3$:Cr," IEEE J. Quantum Electron. QE-23, 2122, 1987.

4. Nandakumar, Ramanujam, "Measurement of the Electro-Optic Properties of Photorefractive Crystals," BS Thesis, MIT, May 1987.

5. Schunemann P. G., D. A. Temple, R. S. Hathcock, H. L. Tuller, H. P. Jenssen, D. R. Gabbe and C. Warde, "Photorefractive Effect in High-Purity $BaTiO_3$" Conference on Lasers and Electro-Optics, Technical Digest Series, Vol. 14, 1987, p. 178.

6. Schunemann, P. G., "Effects of Iron Concentration and Valence on the Photorefractive Properties of $BaTiO_3$," in Digest of the Topical Meeting on Photorefractive Materials, Effects, and Devices, Los Angeles, August 1987, pp. 23-25.

7. Hathcock, R. S., D. A. Temple, C. Warde and R. R. Neurgaonkar, "Photoconductivity in Photorefractive SBN," in Digest of the Topical Meeting on Photorefractive Materials, Effects, and Devices, Los Angeles, August 1987, pp 26-29.

8. Temple, D. A., R. S. Hathcock and C. Warde, "Materials Parameters of Photorefractive crystals from Anisotropic Diffraction Measurements," in Digest of the Topical Meeting on Photorefractive Materials, Effects, and Devices, Los Angeles, August 1987, pp. 122-125.

9. Warde, C., D. A. Temple, P. Schunemann, R. S. Hathcock, H. L. Tuller and H. P. Jenssen, "Photorefractive Effect in $BaTiO_3$:Fe" Proc. SPIE 825, 101, 1987.

10. Temple, D. A., R. S. Hathcock and C. Warde, "Anisotropic Diffraction in Photorefractive $BaTiO_3$," Annual Meeting of the Optical Society of America, October 1987 (Abstract).

11. Hathcock, R. S., "Anomalous Beam Fanning in $BaTiO_3$," Annual Meeting of the Optical Society of America, October 1987 (Abstract).

12. Temple, D. A., Chang, J., and C. Warde, "Amplified Reflection via Anisotropic Scattering in $BaTiO_3$," Optics Letters 13, 764, 1988.

13. Temple, D. A. and C. Warde, "High-Order Anisotropic Scattering in Photorefractive Crystals," JOSA B5, 1800, 1988.

14. Schu emann, P. G., D. A. Temple, R. S. Hathcock, H. L. Tuller, H. P. Jenssen, D. R. Gabbe and C. Warde, "Role of Iron Centers in the Photorefractive Effect in Barium Titanate", J.O.S.A., B5, 1682, 1988.

15. Roberts, James, "Control Methods used to observe the Temperature Dependence of Two-Beam Coupling in $BaTiO_3$," BS Thesis, MIT, May 1988.

16. Temple, Doyle Anthony, "Photo-Induced Absorption and Photorefractive Grating in Barium Titanate," Ph.D Thesis, MIT, September 1988.

17. Hathcock, Ronald Scott, "Optical and Photorefractive Properties of Iron-Doped Barium Titanate, Ph.D Thesis, MIT, September 1989.

18. Temple, D. A., R. S. Hathcock and C. Warde, "Intensity-Dependent Photorefractive Properties of $BaTiO_3$:Fe," J. Appl. Phys. 67, 6667, 1990.

19. Temple, D. A., and C. Warde, "Photo-Induced Optical Absorption in $BaTiO_3$:Fe," submitted to Appl. Phys. Lett. 1991.

13 List of Personnel

Faculty and Staff

    Professor Cardinal Warde

Graduate Students

    Doyle Temple
    R.Scott Hathcock
    Peter G. Schunemann
    Jenq-yang Chang
    Suzanne Lau
    James Kottas
    Xiadan Feng

Undergraduate Students

    Ramanujam Nandakumar
    James Roberts

Support Staff

    Margaret Eminian

DISTRIBUTION LIST

addresses	number of copies
RL/EROP ATTN: JOSEPH HORNER Hanscom AFB MA 01731-5000	10
MASS INSTITUTE OF TECHNOLOGY CAMBRIDGE, MASS 02139	5
RL/SUL Technical Library Griffiss AFB NY 13441-5700	1
Administrator Defense Technical Info Center DTIC-FDAC Cameron Station Building 5 Alexandria VA 22304-6145	2
Defense Advanced Research Projects Agency 1400 Wilson Blvd Arlington VA 22209-2308	2
Naval Warfare Assessment Center GIDEP Operations Center/Code QA-50 ATTN: E Richards Corona CA 91718-5000	1
HQ AFSC/XTH Andrews AFB MD 20334-5000	1
ASD/ENEMS Wright-Patterson AFB OH 45433-6503	1

```
AFIT/LDEE                                    1
Building 642, Area B
Wright-Patterson AFB OH 45433-6583


WRDC/MLPO                                    1
ATTN:  D.L. Denison
WPAFB OH 45433-6533


WRDC/MTEL                                    1
Wright-Patterson AFB OH 45433


AUL/LSE                                      1
Bldg 1405
Maxwell AFB AL 36112-5564


HQ ATC/TTOI                                  1
ATTN:  Lt Col Killian
Randolph AFB TX 78150-5001


Commanding Officer                           1
Naval Avionics Center
Library D/765
Indianapolis IN 46219-2189


Commanding Officer                           1
Naval Ocean Systems Center
Technical Library
Code 96428
San Diego CA 92152-5000


Cmdr                                         1
Naval Weapons Center
Technical Library/C3431
China Lake CA 93555-6001


Superintendent                               1
Code 524
Naval Postgraduate School
Monterey CA 93943-5000
```

CDR, U.S. Army Missile Command   2
Redstone Scientific Info Center
AMSMI-RD-CS-R/ILL Documents
Redstone Arsenal AL 35898-5241

Advisory Group on Electron Devices   2
Attn: Documents
2011 Crystal Drive,Suite 307
Arlington VA 22202

Los Alamos National Laboratory   1
Report Library
MS 5000
Los Alamos NM 87544

Commander/USAISC   1
ATTN: ASOP-DO-TL
Bldg 61801
Ft Huachuca AZ 85613-5000

Software Engineering Inst (SEI)   1
Technical Library
5000 ForbesAve
Pittsburgh PA 15213

NSA   1
T5122/TDL
Fort Meade MD 20755-6000

NSA   1
ATTN: D. Alley
Div X911
9800 Savage Road
Ft Meade MD 20755-6000

Director   1
NSA/CSS R12
ATTN: Mr. Dennis Heinbuch
9800 Savage Road
Fort George G. Meade MD 20755-6000

DoD   1
R31
9800 Savage Road
Ft. Meade MD 20755-6000

DIRNSA   1
R509
9800 Savage Road
Ft Meade MD 20775

Defense Technology Sec Admin (DTSA)   1
ATTN: STTD/Patrick Sullivan
400 Army Navy Drive
Suite 300
Arlington VA 22202